論文 / 著書情報
Article / Book Information

題目(和文)	いくつかのABX3型三角格子反強磁性体の相転移
Title(English)	Phase Transitions in Several ABX_3_-type Triangular Antiferromagnets
著者(和文)	小野俊雄
Author(English)	Toshio Ono
出典(和文)	学位:理学博士, 学位授与機関:東京工業大学, 報告番号:甲第4275号, 授与年月日:2000年3月26日, 学位の種別:課程博士, 審査員:
Citation(English)	Degree:Doctor of Science, Conferring organization: Tokyo Institute of Technology, Report number:甲第4275号, Conferred date:2000/3/26, Degree Type:Course doctor, Examiner:
学位種別(和文)	博士論文
Type(English)	Doctoral Thesis

1999年度　学位論文

Phase Transitions in Several ABX_3-type Triangular Antiferromagnets

理工学研究科 物理学専攻

小野 俊雄

December, 1999

Acknowledgments

The author wish to express his sincere gratitude to his supervisor Professor Hidekazu Tanaka of Tokyo Institute of Technology who gave him the base as an experimental scientist on condensed matter physics. The author is also grateful to him for encouragements and stimulating discussions throughout the present study and for his careful reading of the manuscript for this thesis.

The author is grateful to Professor Katsunori Iio of Tokyo Institute of Technology for his encouragements throughout the course of this study and for his conscientious explanation for the magnetic birefringence measurement and other experimental equipment which is installed in his laboratry.

The author would like to express his thanks to Dr. Tetsuya Kato of Tokyo Institute of Technology, from whom he learned many things how to make plans and progress in neutron scattering and other measurements. The author also appreciates his helpful discussions and continuous encoragements on this study.

The author is grateful Professor Kazuhisa Kakurai and Dr. Kenji Nakajima of Neutron Scattering Laboratory ISSP University of Tokyo for helpful suggestions and their technical supports for the neutron scattering experiments of $CsMn(Br_{0.19}I_{0.81})_3$ and for fruitful discussions related to the phase transitions of $RbFeCl_3$.

The author would like to thank Prof. Hiroyuki Nojiri and Mitsuhiro Motokawa for elaborate measuring the pulsed high field magnetization for the mixed system $CsCu_{1-x}Co_xCl_3$.

The author is deeply indebted to Dr. Andreas Hoser, Professor Ursula Schotte and Dr. Norbert Stüßer of Hahn-Meitner-Institute and Proffesor Klaus D. Schotte of Freie Universität for arrangement of the neutron scattering study for $CsCu_{1-x}Co_xCl_3$ and for helpful discussions and suggestions for this study.

The author would like to express his thanks to Professor Meiro Chiba and Mr. Junichiro Hirano of Istitute of Advanced Energy Kyoto University for showing him their experimental data of ^{133}Cs NMR prior to publication and for useful discussions.

The author is deeply grateful to Professor Hiroyuki Shiba, Dr. Tetsuro Nikuni of Tokyo

Institute of Technology and Professor Allan E. Jacobs of University of Toronto for showing him their latest calculation results which concerened with the field induced phase transitions of $RbFeCl_3$ prior to publication and for stimulating discussions.

The author would like to express his sincere gratitude to Dr. Takashi Kambe of Okayama University who have taught him the basis of the low temperature experiments and gave the technichal instruction of ESR measurements.

The author wants to close his acknowledgements by expressing his great thanks to his peer and junior in Iio-Tanaka Laboratoly, Mr. Budhy Kurniawan, Mr. Hiroshi Horai, Mr. Ken-ichi Takatsu, Ms. Wakako Shiramura, Mr. Katsuhiro Hondou, Mr. Akira Oosawa, Ms. Kiyoko Morishita, Ms. Mariko Ishii, Mr. Hidetoshi Nakamura, Mr. YOSUKE Tanaka, Mr. Syuji Maruyama, for their encouragements, assistance in his experiments, providing him the recent informations of progress of studies for quantum spin systems, most of the type settings for his thesis and for valuable and very interesting disscussions within or out of the field of physics.

Abstract

This thesis reports and discusses the new findings on the phase transition phenomena of three hexagonal ABX_3-type triangular antiferromagnetic (TAF) systems, $CsMn(Br_xI_{1-x})_3$, $CsCu_{1-x}Co_xCl_3$ and $RbFeCl_3$ by means of magnetization measurements and neutron scattering technique.

$CsMnBr_3$ and $CsMnI_3$ are known to be triangular antiferromagnets with the planar and axial magnetic anisotropy, respectively. Magnetic susceptibility and torque measurements have been carried out to investigate the relationship between magnetic anisotropy and phase transition in the mixed triangular antiferromagnetic system, $CsMn(Br_xI_{1-x})_3$. The phase diagram for Néel temperature T_N versus bromine concentration x is obtained. With increasing x, the intermediate ferrimagnetic phase becomes narrower and vanishes at $x_c = 0.19$, where the magnetic anisotropy generally vanishes. The magnetic phase diagrams for external field versus temperature were also determined for the samples with various bromine concentration. For the samples with $x < x_c$ which have axial anisotropies, external fields were applied parallel to the c-axis. The multicritical point appears at $(T_m, H_m) = (9.31\ [K], 5.94\ [T])$ for $CsMnI_3$. The position of the multicritical point shifts toward $(T_{N2}, 0)$ with increasing bromine concentration x. For the samples with $x > x_c$ which have planar anisotropies, fields were applied perpendicular to the c-axis. Spin-flop phases are also realized for the weak planar cases. The spin-flop field H_{sf} is found to be well described as a function of bromine concentration x, $H_{sf}\ [T] = 5.04\sqrt{|x - x_c|/x_c}\ [T]$. For the sample with $x = x_c$, there are no multicritical points and spin-flop phase transitions, and the phase boundary does not depend on the field direction which indicates the isotropic nature. The elastic neutron scattering experiments have been carried out for $x = x_c$ to investigate the magnetic structure and the critical behavior. It is found that in the ordered phase below T_N, the spin planes in which the spins lie with the 120°-structure are tilted from the basal plane, and that the average of the tilting angle ϕ is evaluated as $\langle \cos^2 \phi \rangle = 0.362$, *i.e.* $\phi = 53°$. This result supports that the system $CsMn(Br_xI_{1-x})_3$ with $x = x_c$ is almost at the Heisenberg limit for the interaction. The critical exponent for the sublattice magnetization is obtained as

$\beta = 0.28 \pm 0.02$, which is in agreement with the value predicted for the chiral Heisenberg universality class $\beta = 0.30 \pm 0.02$.

$CsCuCl_3$ is a spin-$\frac{1}{2}$ TAF with planar anisotropy and has 120°-structure below $T_N = 10.5$ K. For this compound, it is known to undergo the field-induced phase transition caused by the competition between the planar anisotropy and quantum fluctuation. In order to control its magnetic anisotropy, the mixed system $CsCu_{1-x}Co_xCl_3$ was synthesized, and the magnetization and magnetic torque have been measured. It is observed that the macroscopic anisotropy changes from the planar type to the axial one with increasing Co^{2+} concentration x. It is found that the small amount of Co^{2+} doping produces a new ordered phase in the low-temperature and low-field region, *i.e.*, this system can undergo two phase transitions at zero field. The transition field at which the new phase becomes unstable is minimum for $H \parallel c$ and maximum for $H \perp c$. With increasing Co^{2+} concentration x, the area of the new phase is enlarged in the phase diagram for temperature versus magnetic field. The new phase has a weak spontaneous magnetization in the c-direction. In order to investigate magnetic structures of the intermediate and low-temperature phases, the neutron elastic scattering experiments have been carried out for the sample with $x \approx 0.03$. It is found that the intermediate phase is identical to the ordered phase of $CsCuCl_3$, and that the low-temperature phase is an oblique triangular antiferromagnetic phase in which spins form triangular structure in a plane tilted from the basal plane. The tilting angle ϕ measured from the c-plane is $\phi = 42°$. The value of ϕ increases with increasing temperature and becomes $\phi = 0$ at $T_{N2} = 7.2$ K. The field variations of the tilting angle depend on the field direction. The tilting angle increases gradually with increasing field and becomes $\phi = 0$ at $H_c^{\perp} = 7.4$ T when $H \parallel c$. On the other hand, when $H \perp c$, ϕ is almost constant up to $H = 3$ T and shows the abrupt change at $H_c^{\parallel} = 3.4$ T. These facts indicate the phase transitions at $H_c^{\perp}$ and $H_c^{\parallel}$ are of second and first order, respectively. The off-diagonal exchange term is proposed as the origin of the oblique phase.

$RbFeCl_3$ is one of the ferromagnetically stacked TAF systems with strong planar anisotropy and has 120°-structure in the ground state. It is known when the external field is applied perpendicular to the c-axis, the incommensurate fan structure is realized via the intermediate commensurate up-up-down structure which can not be explained within the classical theory. In order to investigate the phase diagram in $RbFeCl_3$, the magnetization has been measured as a function of magnetic field and temperature in the applied field parallel to the a-axis. It is found that a new phase exists between the commensurate up-up-down phase and the incommensurate fan phase. It is suggested that the new phase is a commensurate phase with a coplanar structure which is stabilized by the quantum fluctuation in magnetic field.

Contents

1 Overview 1

1.1 Concept of frustration on magnets 1

1.2 Triangular antiferromagnets 3

1.2.1 Ising spin system 3

1.2.2 Continuous (XY and Heisenberg) spin system 5

1.3 Outline of thesis 7

2 Anisotropy and the phase transitions of $CsMn(I_{1-x}Br_x)_3$ 8

2.1 Phase transitions of TAF 8

2.1.1 Phenomelogical Landau theory 8

2.1.2 Ising-like Heisenberg TAF 11

2.1.3 XY-like Heisenberg TAF 11

2.2 Novel critical behavior 14

2.2.1 Chirality 14

2.2.2 Chiral universality class 15

2.3 $CsMnI_3$ and $CsMnBr_3$ 16

2.4 Purpose of this study 21

2.5 Magnetic measurements 22

2.5.1 Sample preparation and equipment 22

2.5.2 Magnetic measurements 23

2.5.3 Variations of phase diagrams 31

2.5.4 Summary of this section 37

2.6 Neutron scattering for $CsMn(Br_{0.19}I_{0.81})_3$ 37

2.6.1 Equipment 37

2.6.2 Results 38

2.7 Summary of this section 42

3 Phase Transitions of $CsCu_{1-x}Co_xCl_3$ 43
3.1 $CsCuCl_3$ . . . 43
3.1.1 Crystal and magnetic structure of $CsCuCl_3$ . . . 43
3.1.2 Magnetic properties in the external field . . . 47
3.2 Purpose of this study . . . 50
3.3 Magnetic measurements of $CsCu_{1-x}Co_xCl_3$ . . . 51
3.3.1 Sample preparation and equipment . . . 51
3.3.2 Results of magnetization measurements . . . 52
3.3.3 Torque measurements . . . 58
3.3.4 High field magnetization process . . . 61
3.3.5 Summary of this section . . . 62
3.4 Neutron scattering from $CsCu_{1-x}Co_xCl_3$ with $x = 0.03$ . . . 63
3.4.1 Equipment . . . 63
3.4.2 Results . . . 63
3.4.3 Discussions . . . 73
3.4.4 Summary of this section . . . 76

4 New ordered phase in $RbFeCl_3$ 78
4.1 $RbFeCl_3$ . . . 78
4.2 Experiments . . . 82
4.3 Discussion . . . 85
4.4 Recent theoretical study . . . 87

5 Summary and further scope 89

List of publications 98

Chapter 1

Overview

Over the last few decades, phase transitions and critical phenomena are one of main problems on statistical physics. Especially, for the magnetic systems which have the spin as an order parameter, various models have been investigated extensively by means of both theoretical and experimental approaches.

Thanks to these works, for the unfrustrated ferromagnets and the antiferromagnets, the behavior of the phase transitions is now rather well understood.

The concept of frustration has a very important role on spin systems, including Ising spin systems, classical vector spin systems such as XY and Heisenberg models and also quantum spin systems. When the inter-spin interactions are fully competing with each other, the qualitative behavior of the phase transition is quite different from that of standard ferromagnets and antiferromagnets. In this chapter, brief introduction for frustrated magnetic models and basic properties on triangular antiferromagnets are described.

1.1 Concept of frustration on magnets

In 1977, Vannimenus and Toulouse introduced the word "frustration" for a square plaquette shown in Fig. 1.1 [1, 2]. In this plaquette the single and double bonds denote the ferromagnetic and antiferromagnetic interactions, respectively. When the Ising spins $s_i = \pm 1$ located at the four sites, the Hamiltonian of this four spin system is described as

$$\mathcal{H} = J_{12}s_1s_2 + J_{23}s_2s_3 + J_{34}s_3s_4 + J_{41}s_4s_1. \tag{1.1}$$

When the absolute values of J_{ij} are $J_{ij} = J$, the ground state of above Hamiltonian degenerates eightfold. The frustration parameter ϕ_p defined by the sign of the product of interactions $\phi_p = \mathrm{sign}(J_{12}J_{23}J_{34}J_{41})$ for the plaquette in Fig. 1.1 is negative. For more general polygon

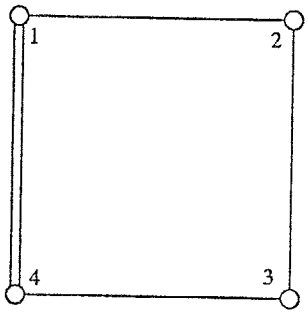

Figure 1.1: A frustrated plaquette with three ferromagnetic and one antiferromagnetic interactions indicated by the three single bonds and one double bond, respectively.

plaquettes, the frustration parameter is defined by

$$\phi_p \equiv \prod_{i=1}^{N} \mathrm{sign}(J_{ii+1}), \tag{1.2}$$

where N denotes the number of sites and $J_{NN+1} = J_{N1}$. If $\phi_p = 1$, the polygon plaquette is non-frustrated, and all spins are arranged so as to satisfy the interactions. If $\phi_p = -1$, the polygon is frustrated. For unfrustrated polygon, the ground state degeneracy is 2. On the other hand, the ground state of frustrated polygon degenerates $2N$-fold. Such a manifold degeneracy is the main character of the frustrated system.

When the lattice is composed of uniform antiferromagnetic bonds between the neighboring sites, the sign of the frustration parameter depends on the topological structure of the lattice. If the lattice can be filled up with the up- and down-spins alternately without confliction among the interactions, the lattice is called *bipartite*, and this is not frustrated. The simplest example of frustrated plaquette is a triangle one with three antiferromagnetic bonds. Non-bipartite lattices are able to be constructed with triangle plaquettes (or polygon with odd vertices). Figure 1.2 shows the examples of the non-bipartite lattices. Many ionic crystals and oxides are known or in attempt to be realized the structure as shown in Fig. 1.2 (b)-(f). Hexagonal BX_2, ABX_3 [13] ionic crystals and layered crystal series $A^{I}M^{III}(X^{VI}O_4)_2$ (A= K, Rb, Cs, NH_4; M=Sc, Fe, Cr, Al, rare earth; X= S, Se, Cr, Mo, W) [3] correspond to (e), and the jarosite compounds $RB_3(OH)_6(SO_4)_2$ (R=NH_4, Na, K, Rb; B=Fe, Cr) and $SrCr_9Ga_3O_{19}$ are known as the kagomé lattice antiferromagnets shown in Fig. 1.2 (f). The zig-zag spin ladder models shown in Fig. 1.2 (c) are often adopted as the Heisenberg linear chain with antiferromagnetic next nearest neighbor (NNN) interaction. Recent numerical studies for $S = \frac{1}{2}$ zig-zag spin ladder reveal that the frustration effects of NNN interactions induce the magnetization jump in M-H curve due to the Fermi-liquid to non-Fermi-liquid

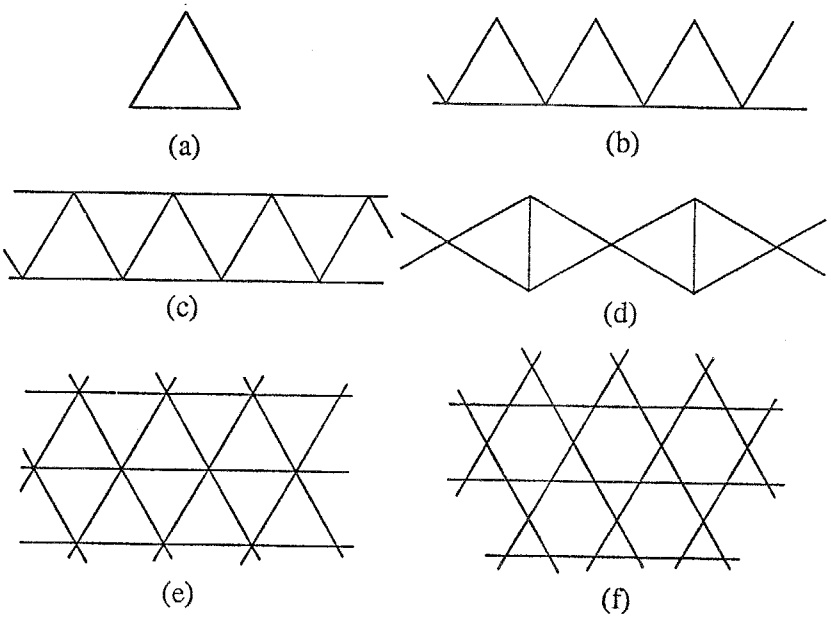

Figure 1.2: Examples of the non-bipertite lattices. (a) single triangular plaquette, (b) Δ-chain, (c) zig-zag ladder, (d) diamond-shaped chain (e) triangular lattice and (f) kagomé lattice.

(singlet-dimer) transition in the field [4, 5], when the magnitude of the bond strength along the leg is larger than one fourth of that of zig-zag rang. Suitable experimental results have not been reported yet. However, this prediction would be confirmed experimentally soon. Also for the models corresponding to (b) [6] and (d) [7], several theoretical and experimental attempts in the view point of the generalized quantum Heisenberg linear chain are now in progress.

Due to the manifold degeneracy at the ground state, various kinds of perturbations can be the candidate for the cause of phase transitions.

1.2 Triangular antiferromagnets

1.2.1 Ising spin system

Stimulated by Onsager's exact solution for the Ising spin on the square lattice [8], several Ising spin systems on the two dimensional lattices which include triangular lattice have been studied. Wannier showed rigorously that the ground state of the Ising triangular antiferromagnet (TAF) degenerates with $\sim 2^{0.487N}$ states and no phase transition occurs until zero

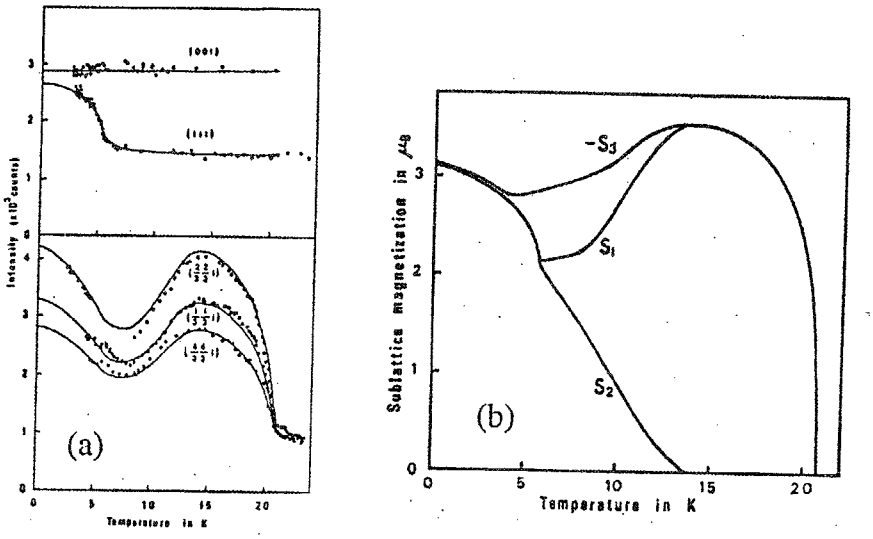

Figure 1.3: (a) Temperature dependence of the magnetic Bragg reflection from $CsCoCl_3$. Solid lines indicate the calculated values for sublattice magnetizations given in (b). (b) Probable temperature dependence of sublattice magnetizations.

temperature [9, 10]. Large number of the degeneracy is partially lifted by introducing NNN ferromagnetic interaction, and up-up-down ferrimagnetic structure is realized in the ground state due to large entropy. Using mean field approximation, Mekata [91] showed that the *partial disordered* phase in which one third of spins on the TAF are disordered and the others are ordered anti parallel is realized between paramagnetic and ferrimagnetic phases, when the ratio of the nearest neighbor interaction J_1 and the NNN interaction J_2 satisfies $|J_2/J_1| \leq 0.8$.

Figure 1.3 shows the magnetic Bragg reflection from $CsCoCl_3$ as a function of temperature. $CsCoCl_3$ is one of the quasi one-dimensional stacked TAF with $CsNiCl_3$ structure shown in Fig. 2.7. Since the intrachain interaction is $|J_0|/k_B = 75$ K, the short range order in the chain develops in the temperature region $T < 75$ K, and each chain can be regarded as a spin on the triangular lattice . Due to the crystal field, Co^{2+} ion has the strong Ising anisotropy, so that $CsCoCl_3$ is regarded as the model substance of Ising TAF with fictitious spin $\frac{1}{2}$ with $g \sim 6$. In Fig. 1.3, the curious temperature dependence of Bragg intensities (a) are explained, as the partial disordered structure is realized in the intermediate phase, and three sublattice magnetizations vary as shown in Fig. 1.3 (b) [92]. The fact that one of the three equivalent sublattices is left disordered in the real magnet has attracted a great attention, and stimulated many theoretical and experimental studies on TAF.

1.2.2 Continuous (XY and Heisenberg) spin system

When the degrees of freedom of spins are larger than or equal to 2, there is no longer a phase transition in the ferromagnetic and antiferromagnetic square lattice. Since the energy loss is small against the disturbance due to large degrees of freedom, the system profits free energy from increase of entropy. Although, Ising TAF does not exhibit any phase transition until 0 K, XY TAF undergoes phase transition with releasing the frustration partially and establish the spin configuration called "120° spin structure", in which three XY spins form 120° angles with the neighboring spins as shown in Fig. 2.6. Though the frustration is partially released, there remains continuous degeneracy around the axis perpendicular to the spin plane in which spins form 120° structure and "*chirality*" which will be mentioned in section 2.2.

In the ground state of Heisenberg TAF, three spins are also arranged as the 120° structure. However, additional continuous degeneracy of three dimensional global rotation of the spin plane remains. When the magnetic field is applied to the Heisenberg TAF which has nearest neighbor interaction $J > 0$, the Hamiltonian of the system is described by

$$\mathcal{H} = 2J \sum_{\langle ij \rangle} \boldsymbol{S}_i \cdot \boldsymbol{S}_j - g\mu_{\mathrm{B}} \boldsymbol{H} \sum_i \boldsymbol{S}_i, \tag{1.3}$$

where the summation $\langle ij \rangle$ runs over the nearest pairs. In the classical limit, the ground state energy per spin E/N is expressed by the three vectors $\boldsymbol{S}_1$, $\boldsymbol{S}_2$ and $\boldsymbol{S}_3$ which correspond the sublattice magnetization on TAF as follows;

$$\frac{E}{N} = 2J(\boldsymbol{S}_1 \cdot \boldsymbol{S}_2 + \boldsymbol{S}_2 \cdot \boldsymbol{S}_3 + \boldsymbol{S}_3 \cdot \boldsymbol{S}_1) - \frac{1}{3} g\mu_{\mathrm{B}} \boldsymbol{H} \cdot (\boldsymbol{S}_1 + \boldsymbol{S}_2 + \boldsymbol{S}_3). \tag{1.4}$$

Using the relation

$$(\boldsymbol{S}_1 + \boldsymbol{S}_2 + \boldsymbol{S}_3)^2 = 3S^2 + 2(\boldsymbol{S}_1 \cdot \boldsymbol{S}_2 + \boldsymbol{S}_2 \cdot \boldsymbol{S}_3 + \boldsymbol{S}_3 \cdot \boldsymbol{S}_1)$$

above equation is factorized as follows;

$$\frac{E}{N} = -3JS^2 - \frac{(g\mu_{\mathrm{B}}H)^2}{36J} + J\left(\boldsymbol{S}_1 + \boldsymbol{S}_2 + \boldsymbol{S}_3 - \frac{g\mu_{\mathrm{B}}\boldsymbol{H}}{6J}\right)^2. \tag{1.5}$$

Thus, the equilibrium condition for the ground state in the field is given by

$$\begin{aligned} \boldsymbol{S}_1 + \boldsymbol{S}_2 + \boldsymbol{S}_3 &= \frac{g\mu_{\mathrm{B}}\boldsymbol{H}}{6J} \qquad \text{and} \\ |\boldsymbol{S}_1| = |\boldsymbol{S}_2| &= |\boldsymbol{S}_3| = S. \end{aligned} \tag{1.6}$$

This expression gives only three parameters which determine the spin orientation, so that arrangement of the three spins are not determined uniquely, and there remains "non-trivial continuous degeneracy" [11]. It is surprising that even though the magnetic field breaks the spherical symmetry of the Hamiltonian, there still exists continuous solutions. Kawamura and Miyashita [12] performed a Monte Carlo simulation of the Heisenberg TAF in a magnetic field. They argued that the thermal fluctuations lift the continuous degeneracy and all spins are restricted in the plane parallel to the field, and that with increasing field, the orientation of the spins change as shown in Fig. 1.4. It should be noted that the collinear spin structure

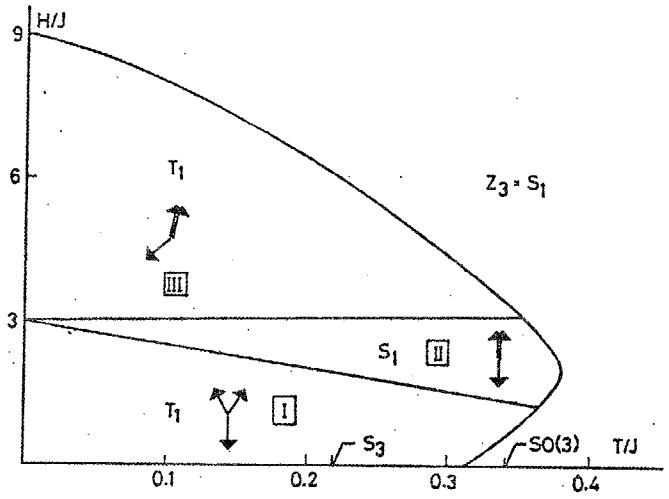

Figure 1.4: Magnetic phase diagram of Heisenberg TAF. (quoted from ref. [12].)

is stabilized in the middle field range. The quantum fluctuations can also lift the continuous degeneracy of the ground state of the Heisenberg TAF, as we see in chapters 3 and 4.

1.3 Outline of thesis

Since the frustration gives the large thermal and quantum fluctuations between the states which are energetically close to each other, a small perturbation which is neglected in the unfrustrated systems often plays an important role at the event of the phase transitions. In this thesis, we treat three TAF systems which show various types of phase transitions due to different origins.

The rest of this thesis is organized as follows. In chapter 2, the experimental studies for the mixed TAF system $CsMn(Br_xI_{1-x})_3$ are described. Since this system has Mn^{2+} ion ($S = 5/2$) as the magnetic ion and has controllable magnetic anisotropy, the information for the relation between the weak anisotropy and phase transitions is available. In addition to that, the critical behavior in the vicinity of the transition points is known to be different from those of the unfrustrated systems due to the fact that the canted spin structure such as 120° structure has the novel Z_2 symmetry. In the present work, the critical behavior is studied for $CsMn(Br_{0.19}I_{0.81})_3$ which can be regarded as the Heisenberg limit classical TAF. In chapter 3, the magnetic measurements and neutron scattering studies for $S = \frac{1}{2}$ mixed TAF system $CsCu_{1-x}Co_xCl_3$ are presented. Experimental and theoretical studies for $CsCuCl_3$ reveal that the quantum fluctuation determines the spin structure in the high field region. In the present study, one attempt to reduce the magnetic anisotropy which determines the low field spin structure is given. The Co^{2+} ion doping effect results in the new type of the phase transition. Although the origin of the new phase transition is not clear at present, a candidate of the driving force of this transition is discussed. In chapter 4, an XY TAF system $RbFeCl_3$ is studied in connection with the theoretical prediction [90] which argues that the successive quantum phase transition occurs in the field along the plane in which spins are confined. The result indicating the appearance of the newly found ordered phase is presented. The last chapter is devoted to the whole summary and further scope.

Chapter 2

Anisotropy and the phase transitions of $CsMn(I_{1-x}Br_x)_3$

Real magnets have more or less magnetic anisotropies. As mentioned in the former chapter, the continuous degeneracy which TAFs has is lifted mainly by the magnetic anisotropy which is caused by various origins, and the magnetic phase diagrams depend strongly on the anisotropy . In the first half of this chapter, theoretical and experimental investigations focused on the relationship between the phase transitions and the magnetic anisotropies on TAFs are reviewed, and the character of the critical behavior caused by the magnetic frustration among the nearest neighbor interactions is described. In the latter half, the results of the magnetic measurements performed on $CsMn(I_{1-x}Br_x)_3$ and the results of the neutron scattering experiments performed on the sample with $CsMn(I_{0.81}Br_{0.19})_3$ are described.

2.1 Phase transitions of TAF

The magnetic phase diagrams for the stacked TAF are full of variety, which reflects the bonding frustration between the neighboring spins and the weak axial or planar magnetic anisotropy. For the Heisenberg like spin system, spin structure is stabilized by the weak magnetic anisotropy and the external field. When the external field is applied along the direction which is favorable for the anisotropy, the competition between the anisotropy and Zeeman energies will occur.

2.1.1 Phenomelogical Landau theory

Plumer and his coworker derived the wide variety of the phase diagram in connection with the experimental study for multi criticalities of the $CsMnBr_3$ and $CsNiCl_3$ or the other ABX_3 TAF compounds [21, 22] using the phenomelogical Landau (mean-field) theory. Landau free

energy is expressed by the order parameter which is characterized by the spin density $s(r)$. In the vicinity of the second order phase boundary, since it can be assumed that the amount of the spin density is sufficiently small, it is able to expand the free energy around phase boundaries, with respect to $s(r)$. Thermal effect is contained as the expansion coefficient of the second-order of the order parameter. Taking into account up to fourth-order of the order parameter, the ordered phases which were reported by the experimental studies are reproduced by adjusting the expansion coefficients and the transition temperature. When the system undergoes the second order phase transition from the paramagnetic to an ordered state, it is assumed the ordering can be characterized by the spin density $s(r)$ which has single modulation wave vector as the next form,

$$s(r) = \frac{V}{N}\sum_{R}\rho(r)\delta(r-R) \tag{2.1}$$

$$\rho(r) = m + S\exp(iQ\cdot r) + S^{*}\exp(-iQ\cdot r), \tag{2.2}$$

where R gives the positions of the magnetic ions, m is the uniform magnetization induced by the external field H, S is the spin polarization and Q is the spin density wave vector, which characterize the spin arrangements in the ordered phases. When the spin structure is non-collinear, the polarization vector S has the two components, which correspond to cosine and sine components , and S can be defined as the complex vector,

$$S = S_1 + iS_2. \tag{2.3}$$

where S_1 and S_2 are real vectors described as

$$S_1 = S\cos\beta(\sin\hat{\rho}_1 + \cos\theta\hat{z}) \tag{2.4}$$

$$S_2 = S\sin\beta\hat{\rho}_2 \tag{2.5}$$

where $\hat{\rho}_1 \perp \hat{\rho}_2 \perp \hat{z}$. The illustration which describes above definition is shown in Fig. 2.1. Plumer *et al.* argued that the free energy can be expressed with power of order parameter $s(r)$ up to fourth-order for the crystals which have hexagonal symmetry, as follows:

$$F = F_I + F_{A2} + F_{A4}, \tag{2.6}$$

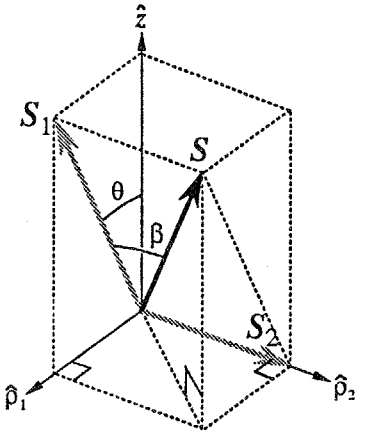

Figure 2.1: The definition of the polarization vector $\boldsymbol{S}$. $\hat{\rho}_2$-axis implies the imaginary part of $\boldsymbol{S}$.

and

$$\begin{aligned} F_I =& A_Q S^2 + \frac{1}{2}A_0' m^2 + B_1 S^4 \frac{1}{2}B_2 |S \cdot S|^2 + \frac{1}{4}B_3 m^4 \\ &+ 2B_4 |m \cdot S|^2 + B_5 m^2 S^2 - m \cdot H, \end{aligned} \tag{2.7}$$

$$F_{A2} = - A_z |S_z|^2 - A_{z0} m_z^2, \tag{2.8}$$

$$\begin{aligned} F_{A4} =& \frac{1}{2}E_1 (m_z^2 |S_\perp|^2 + m_\perp^2 |S_z|^2) + E_2 |S_z|^2 |S_\perp|^2 \\ &+ \frac{1}{4}E_3 [S_z^2 (S_x^{*2} + S_y^{*2}) + \text{c.c.}] + \frac{1}{2}E_4 m_z^2 m_\perp^2 \\ &+ \frac{3}{2}G_1 |S_z|^4 + 3G_2 m_z^2 |S_z|^2 + \frac{1}{4}G_3 m_z^4, \end{aligned} \tag{2.9}$$

where F_I includes all isotropic terms up to fourth order in $\boldsymbol{s}$, F_{A2} is the contribution from second-order anisotropy terms, and F_{A4} includes all fourth-order anisotropy terms. In eqs. 2.7 $S^2 = \boldsymbol{S} \cdot \boldsymbol{S}$, $\boldsymbol{S}_\perp = S_x \hat{\boldsymbol{x}} + S_y \hat{\boldsymbol{y}}$, and $\hat{\boldsymbol{z}}$ defines the direction of the c-axis of the hexagonal lattice. In above expressions, the terms which satisfy $3\boldsymbol{Q} = \boldsymbol{G}$ or $4\boldsymbol{Q} = \boldsymbol{G}$ are not included, where $\boldsymbol{G}$ is a reciprocal lattice vector. For the most of the hexagonal ABX_3-type TAFs, typical 120°-structure in the c-plane is expressed as $\boldsymbol{Q} = (1/3, 1/3, 1/2)$ in the lattice which consists of only magnetic ion, so that $6\boldsymbol{Q} = \boldsymbol{G}$. Temperature dependence is included in the second-order isotropic coefficients which are described as

$$A_Q = a(T - T_Q), A_0 = A_0' - A_{z0} = a(T - T_0), \tag{2.10}$$

where $a > 0$ and $T_Q > T_0$ are assumed. T_Q and T_0 correspond to the ordering temperature and the paramagnetic Curie temperature, respectively. Since the A_z and A_{z0} act as an

axial anisotropy when $A_z \sim A_{z0} > 0$, and a planar anisotropy when $A_z \sim A_{z0} < 0$. That the condition of weak anisotropy is described as $|A_z|, |A_{z0}| \ll A_0 - A_Q = a(T_Q - T_0)$ and $|E_i|, |G_i| \ll |B_i|$. Non-collinear spin structure is mainly produced by the term $B_2|\boldsymbol{S} \cdot \boldsymbol{S}|^2$ in eqs. 2.7. When $B_2 > 0$, this term favors the helical spin structure, while it favors collinear spin structure if $B_2 < 0$. The term $2B_4|\boldsymbol{m} \cdot \boldsymbol{S}|^2$ produces the spin-flop phase. Since the spin configuration favors $\boldsymbol{S} \perp \boldsymbol{H}$ in the sufficiently high field, $2B_4|\boldsymbol{m} \cdot \boldsymbol{S}|^2$ is taken to be positive. Within the molecular field approximation, the relations $B_1 = \cdots = B_5$, $E_1 = \cdots = E_4$ and $G_1 = G_2 = G_3$ are satisfied, however, in the phenomelogical Landau theory, it is assumed these coefficients are independent parameters with each other and determined from the experimental results with breaking the equality relationships.

2.1.2 Ising-like Heisenberg TAF

$CsNiCl_3$, $RbNiCl_3$, $CsNiBr_3$, $RbNiBr_3$ and $CsMnI_3$ belong to the space group $P6_3/mmc$, and are materials which fulfill the conditions of Heisenberg hexagonal ABX_3 TAF with weak axial-type anisotropy. Figure 2.2 shows the magnetic phase diagram of these materials which are correspondent to the case

$$A_z > 0, B_2 > 0, B_4 > 0 \tag{2.11}$$

for the phenomelogical Landau free energy as mentioned above. These coefficients favor axial arrangement, helical structure and $\boldsymbol{H}$ $\perp$spin-plane in the high-field (i.e., spin-flop). Phases 1, 2, 3 and 4 indicate the paramagnetic, two-sublattice ferrimagnetic order along the c-axis, triangular structure in the ac-plane and 120°-structure in the c-plane, respectively. The phase boundary between phases 3 and 4 is of first order spin-flop transition. Tanaka *et al.* [16] show that the critical field H_c of the spin-flop transition is given by

$$H_c^{\parallel} = \sqrt{8J_0(D + \Delta J)}S/g\mu_B \tag{2.12}$$

at $T = 0$, when J_1, D and ΔJ are sufficiently small, where J_0, J_1, D and ΔJ are the intra chain, inter chain exchange interactions, the single ion anisotropy and pseudo dipolar anisotropy, respectively (the definitions are given in eq. (2.19)).

2.1.3 XY-like Heisenberg TAF

$CsMnBr_3$, $CsVBr_3$, $CsVCl_3$, $RbVCl_3$ and $CsVI_3$ are the members which are the Heisenberg hexagonal ABX_3 TAF with planar-type anisotropy. Their phase diagrams are classified into two cases for $3J_1 > D$ and $3J_1 < D$ [13, 17, 20]. The magnitudes of J_1 and D are estimated from neutron scattering experiments [13], and it is found that $CsMnBr_3$ corresponds to the

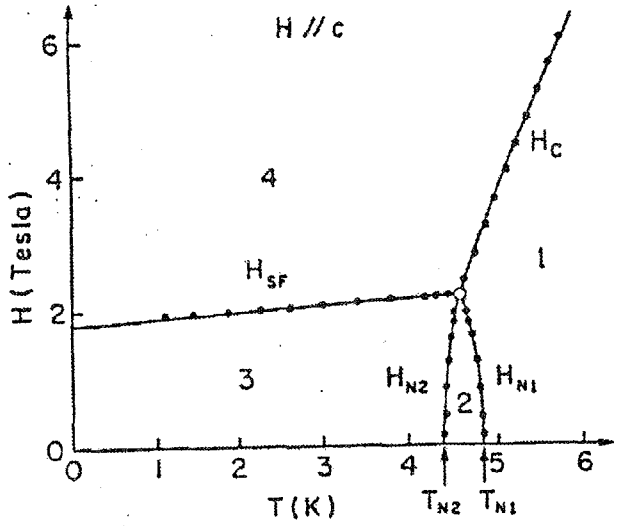

Figure 2.2: The phase diagram of $CsNiCl_3$. Solid circles indicate the experimental data measured by Johnson *et al.* [15]. Solid lines are the fitting result by Plumer *et al.* (quoted from ref. [18])

case $3J_1 < D$, and the others correspond to the case of $3J_1 > D$. Figure 2.3 shows the magnetic phase diagrams for both cases which are correspondent to the case

$$A_z < 0, B_2 > 0, B_4 > 0. \tag{2.13}$$

These coefficients favor planar arrangement, helical structure, and $B_4 > 0$ induces the spin-flop transition for $H \perp c$. In Fig. 2.3 the phases 1, 3, 4, 5 and 7 indicate the paramagnetic, spin-flop phase, 120°-structure in the c-plane, the collinear spin arrangement perpendicular to the field direction and deformed planar triangular structure, respectively. The spin-flop phase transition occurs at $H_c^{\perp}$ which is described by

$$H_c^{\perp} = \sqrt{8J_0(D + \Delta J)}S/g\mu_B. \tag{2.14}$$

In the spin-flop phase, the components of the spin moments projected on to the plane perpendicular to the external field form a triangular structure, and one of spin on the three sublattice remains in the c-plane, as shown in Fig. 2.4. Due to the strong anisotropy, $CsMnBr_3$ does not exhibit the spin-flop phase 3 in Fig. 2.3. For $CsVX_3$ (X=Cl, Br, I) and $RbVCl_3$, the realization of type-3 phase is expectied. However, due to the strong intrachain exchange coupling , *i.e.* $80\text{K} \sim J_0/k_B \sim 120\text{K}$, whole phase diagram has not been obtained.

Systematic investigation for the relationship between anisotropy and the transition points of TAF has been made by Miyashita and Kawamura [55]. They peformed Monte-calro simu-

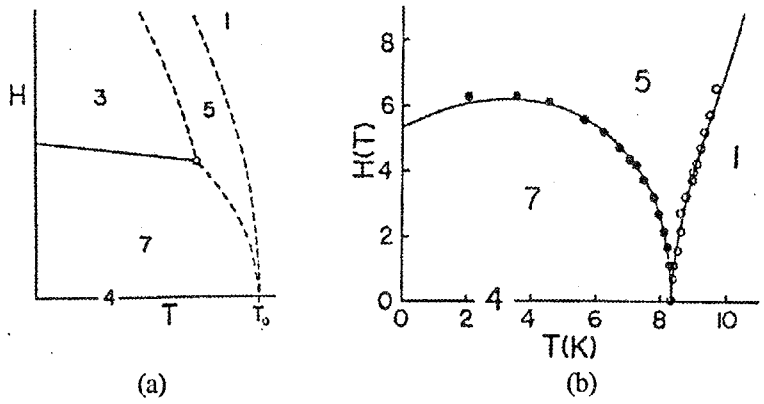

Figure 2.3: (a)Schematic phase diagram for $H \perp c$ and $A_z < 0, B_2 > 0, B_4 > 0$. Solid line and the open circle indicates the first-order spin-flop transition and the multicritical point, respectively. Dashed lines indicate the second order transition. (b) Phase diagram of $CsMnBr_3$. Closed and open circles are the experimental data measured by Gaulin *et al.* [36] Solid lines are the fitting result by Plumer *et al.* The definitions of the numbers are described in the text. (quoted from ref. [21, 19])

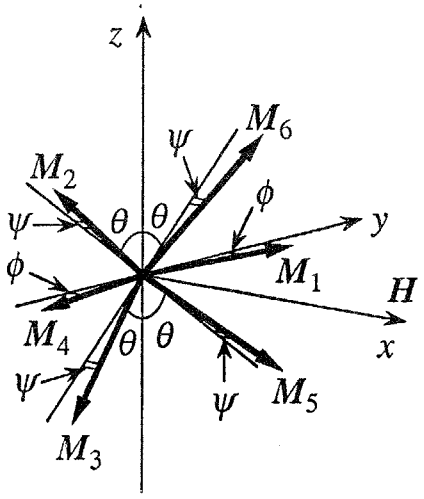

Figure 2.4: The spin configuration in the spin-flop phase of the Heisenberg TAF with weak planar anisotropy. (quoted from ref. [17].)

lations on the specific heat of the stacked TAFs with general anisotropy. They obtained the phase diagram for the anisotropy A defined by $A = J_z/J_{xy}$ versus phase transition temperature, where J_z and J_{xy} are the inter-spin coupling constants for the c-axis and the ac-plane components, respectively. Their results are shown in Fig. 2.5. Two phase transitions occur

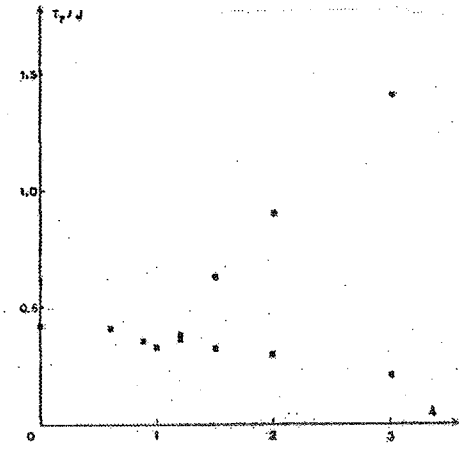

Figure 2.5: Phase diagram of magnetic anisotropy A defined as $A = J_z/J_xy$ versus transition temperature. $A = 1$ denotes the Heisenberg limit.

for $A > 1$. The two transition points approach each other with increasing A, and meet at $A = 1$ which denotes the Heisenberg limit.

2.2 Novel critical behavior

2.2.1 Chirality

For the continuous spin systems such as XY and Heisenberg TAF, the frustration is partially released and spins are ordered in the 120°-structure in the ground state. For such non-collinear spin ordering, extra degrees of freedom appear as shown in Fig. 2.6. In the case of XY spin, the ground state is twofold degenerate, according to whether the 120° spin structure is right- or left-handed. This degenracy is so called *chiral degeneracy*. In a bipartite lattice, long range ordering can be established by global spin rotation. On the other hand, a chiral state cannnot be transformed into the opposite chiral state with any global spin rotation in the XY-plane. The grobal spin reflection is required to achieve the opposite chiral state. To

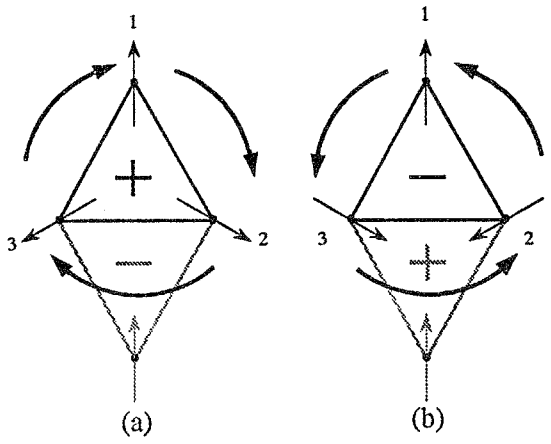

Figure 2.6: Twofold degeneracy arised as the consequence of the partial release of the frustration in the case of XY TAF. (a) and (b) shows the right- and left- handed 120°-structure, each of which is characterized by the opposite chirality.

characterize these two chiral states, it is convenient to introduce the chirality defined by

$$\kappa_p = \frac{2}{3\sqrt{3}} \sum_{\langle ij \rangle}^{p} [S_i \times S_j]_z = \frac{2}{3\sqrt{3}} \sum_{\langle ij \rangle}^{p} (S_i^x S_j^y - S_i^y S_j^x), \tag{2.15}$$

where the summation runs over the triangle plaquette. In the case of Fig. 2.6 (a) and (b), the chirality equals to +1 and -1, respectively. For Heisenberg spin system, there is no longer a chiral degenracy, since the two chiral states shown in Fig 2.6 can be transformed into each other with continuous three dimensional spin rotation. For this case, chirality is defined as the vector described by

$$\kappa_p = \frac{2}{3\sqrt{3}} \sum_{\langle ij \rangle}^{p} \boldsymbol{S}_i \times \boldsymbol{S}_j. \tag{2.16}$$

Application of the chirality concepts to the magnetic systems was originary performed by Villain [56].

2.2.2 Chiral universality class

The critical behavior of physical properties near a second-order phase transition is determined by the universality class, which is classified by only a few parameters reflecting the symmetry of the system such as the spatial dimensionality d of the system and the number of components of the order parameter n. Each universality class is characterized by the set of critical

Exponent	Definition	Condition(s)
α (specific heat)	$C \propto \|T - T_c\|^{\alpha}$	H=0
β (sublattice magnetization)	$M_s \propto (T_c - T)^{\beta}$	$T < T_c, H = 0$
γ (staggered susceptibility)	$\chi_s \propto \|T - T_c\|^{-\gamma}$	$H = 0$
ν (correlation length)	$\xi \propto \|T - T_c\|^{-\nu}$	

Table 2.1: Critical exponents and their definitions.

exponents defined in Table 2.1. For the critical exponents, within a universality class, the scaling laws are derived as follows,

$$\alpha + 2\beta + \gamma = 2, \qquad \text{(Rushbrooke's law)} \tag{2.17}$$

$$\nu d = 2 - \alpha. \qquad \text{(Josephson's law)} \tag{2.18}$$

Since the non-collinear spin ordering produces the new degrees of freedom *chirality*, it is expected that the universaity class of the system is different from that of standard unfrustrated systems.

Kawamura pointed out that the stacked XY and Heisenberg TAFs belong to the new universality classes, chiral universality classes, characterized by new critical exponents [27, 47] which are listed in Table 2.3. Kawamura's prediction for chiral Heisenberg universality class is supported by several numerical calculation studies [57, 58, 59]. However, in XY case, several theoretical and experimental reports conflict to the chiral universality seanario [60, 61, 62, 63, 64]. The critical exponents for the XY universality class are very close to those of mean field tricritical behavior (see Table 2.3.). Thus, it is hard to distinguish the criticality of chiral XY from meanfield tricritical point by the finite size numerical study and the experimental study.

2.3 $CsMnI_3$ and $CsMnBr_3$

$CsMnI_3$ and $CsMnBr_3$ are the members of the ABX_3-type TAF group, which crystallizes in $CsNiCl_3$ structure with space group $P6_3/mmc$. The magnetic interactions of these TAF group are usually represented by

$$\mathcal{H} = 2J_0 \sum_{\langle i,j \rangle}^{\text{chain}} S_i \cdot S_j + 2J_1 \sum_{\langle \ell,m \rangle}^{\text{plane}} S_\ell \cdot S_m + 2\Delta J \sum_{\langle i,j \rangle} S_i^z S_j^z + D \sum_i (S_i^z)^2, \tag{2.19}$$

where the first and second terms are the exchange interactions along the chain and in the basal plane, respectively. The third and last terms denote the pseudodipolar interaction and

the single-ion anisotropy, respectively. Since J_0 is significantly larger than J_1 ($J_0/J_1 > 10^2$), with some exceptions, the ABX_3 antiferromagnets behave as one-dimensional spin systems at high temperatures. With decreasing temperature, the interchain spin correlation grows, so that three-dimensional ordering occurs. Since the J_1 interaction is antiferromagnetic, they are described as stacked TAF in the vicinity of and below the ordering temperature. Thus the spin frustration plays an important role [23, 24, 26, 28, 29, 30, 35]. $CsMnBr_3$ and $CsMnI_3$ are typical examples of the stacked TAF with planar and axial anisotropy respectively. Figure 2.7 illustrates the crystal structure for $CsMnX_3$ compounds. Their lattice and magnetic

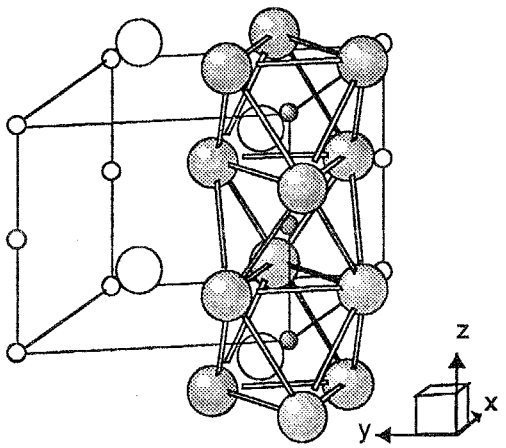

Figure 2.7: The crystal structure $CsMnX_3$ compounds. Small circles are Mn^{2+} ions which have $S = \frac{5}{2}$, and large circles and shaded large circles denote Cs^+ and X^- ios, respectively.

parameters are summarized in table 2.2. The origin of the anisotropy for both compounds is

	$CsMnBr_3$	Reference	$CsMnI_3$	Reference
J_0/k_B	10.3 K	[36]	9.5K	[38]
J_1/k_B	0.020 K	[36]	0.042 K	[38]
$\Delta J/k_B$	-0.070 K	[39]	0.025 K	[40]
T_N	8.37 K	[35]	$T_{N1} = 8.2$K $T_{N2} = 11.2$K	[41, 42]
a (at r.t.)	7.61 Å	[43]	8.20 Å	[44, 45]
c (at r.t.)	6.52 Å	[43]	6.96 Å	[44, 45]

Table 2.2: Lattice and magnetic parameters of $CsMnBr_3$ and $CsMnI_3$. The values of ΔJ are estimated from the anisotropy energies shown in references [39] and [40].

mainly the pseudodipolar interaction, which is shown in the next section.

$CsMnBr_3$ undergoes a phase transition at $T_N = 8.3$ K. In the ordered phase, the spins lie in the basal plane and form a 120° structure. In the magnetic phase diagram, the transition point at zero field is associated with the tetracritical point. The criticalities of this transition point are discussed as the realization of the chiral XY universality class [46]. In the finite magnetic field perpendicular to the c-axis, an intermediate phase which has collinear spin arrangement appears [36]. Figure 2.8 shows the magnetic phase diagram obtained by the magnetization measurements in a field in the c-plane [23]. The critical behavior is described

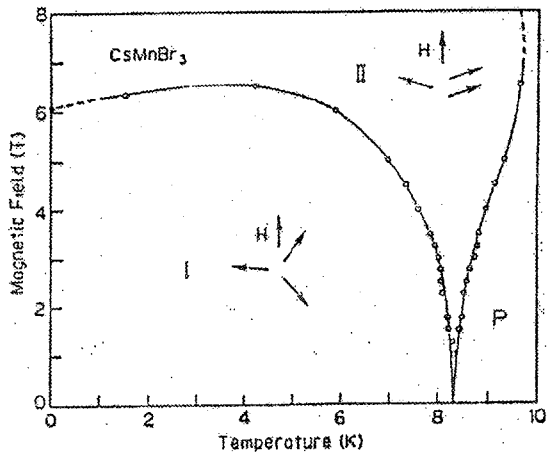

Figure 2.8: The phase diagram of $CsMnBr_3$ in a magnetic field applied in the c-plane. Transition points were determined by the magnetization measurements.

by the conventional XY universality class and Ising universality class for upper and lower phase boundary, respectively [46]. The anisotropy crossover is predicted in the vicinity of the tetracritical point. Kawamura argued that the curvature of the two phase boundaries is described by the crossover exponent ϕ as

$$H^2 = w^{\pm}[T(H) - T(0)]^{\phi}, \tag{2.20}$$

where $T(H)$ is the transition temperature for the two phase lines in the field H, w^+ and w^- are the coefficients for the upper and lower phase boundaries, respectively. The crossover exponent ϕ and the ratio w^+/w^- should be the same within a universality class. For the chiral universality class, ϕ is predicted as $\phi = 1.04$ by means of renormalization group calculation [46]. The values of ϕ derived from the neutron scattering experiments are $\phi^+ = 1.21 \pm 0.07$ and $\phi^- = 0.75 \pm 0.05$ for the higher and lower transition line, respectively [36]. The discrepancy between ϕ^+ and ϕ^- is suspected to come from the ambiguity of $T(0)(= T_N)$. Figure 2.9 shows the analysis of the crossover exponents, which indicates the strong dependence on the

assumption of $T(0)$ [37]. The variation of $T_N = 8.32 \pm 0.05$ K gives the ~25 % variation

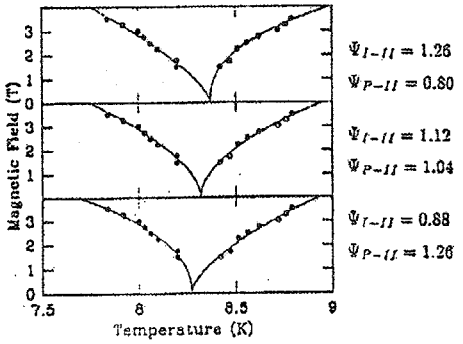

Figure 2.9: The discrepancy of the higher and lower cross-over exponents due to the ambiguity of T_N using the magnetization data [23] of $H > 1.5$ T. $T_N = 8.32$ K gives the $\phi^+ = 1.12$ and $\phi^- = 1.04$ as shown in the middle. Upper and lower diagrams indicate the results of fitting for the varied T_N with + and -0.05 K, respectively. (quoted from ref. [37])

of the crossover exponents. Taking into account of such ambiguity of T_N, the discrepancy between ϕ^+ and ϕ^- is understandable. However, it is suspected that the boundaries of high field region is no longer governed by the crossover exponent. Experimental results for the critical exponents of $CsMnBr_3$ at the tetracritical point are summarized in table 2.3. The

	α	β	γ	ν
3D Ising[48]	0.106	0.326	1.238	0.631
3D XY[48]	-0.01	0.345	1.316	0.669
3D Heisenberg[48]	-0.121	0.367	1.388	0.707
Tricritical	0.5	0.25	1.0	0.5
chiral XY[46]	0.34(6)	0.253(10)	1.13(5)	0.54(2)
chiral Heisenberg[46]	0.24(8)	0.30(2)	1.17(7)	0.59(2)
$CsMnBr_3$	0.40(5)[35]	0.25(1)[28]	1.1(1)[31]	0.53(3)[31]
$CsMnI_3$ (T_{N1})		0.32(1)[32]	1.12(7)[33]	0.59(3)[33]
$CsMnI_3$ (T_{N2})	-0.05(15)[34]	0.35(1)[32]	1.04(3)[33]	0.56(2)[33]

Table 2.3: Critical exponents for the conventional three-dimensional universality classes, the chiral universality classes, and experimental values for $CsMnBr_3$ and $CsMnI_3$.

obtained values show the excellent agreement with Monte Carlo calculation for a chiral XY universality class.

$CsMnI_3$ has two phase transitions at $T_{N1} = 11.2$ K and $T_{N2} = 8.2$ K. In the intermediate phase, the c-axis component of the spin is ordered, with ferrimagnetic structure in the basal

plane. In the low-temperature phase the perpendicular component of the spin is ordered, such that the spins form a triangular structure in the plane including the c-axis, i.e., one-third of the spins are parallel to the c-axis and the rest of the spins are canted away from the c-axis. A scaling analysis by Kawamura *et al.* [26] predicted that both of the transitions belong to the conventional $d = 3$ XY universality class. Figure 2.10 shows the magnetic phase diagram of $CsMnI_3$ determined by the magnetization measurements in the field parallel to the c-axis performed by Katori *et al* [24]. The transition between the paramagnetic phase and the

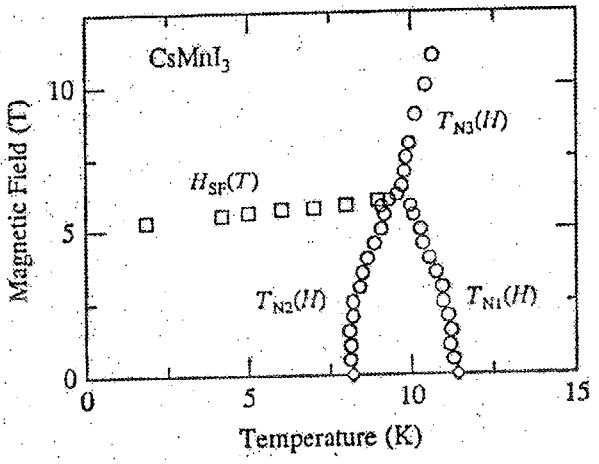

Figure 2.10: Magnetic phase diagram of $CsMnI_3$. Open circles were determined by the results of the temperature dependences of the magnetizations and the open squares were determined by the field dependences of the magnetization. Transition points in zero field is determined by the neutron scattering.

spin-flop phase belongs to $d = 3$ chiral XY universality class. In the phase diagram shown in Fig. 2.11, four phase boundaries meet at (T_m, H_m). According to the scaling analysis, in the vicinity of the multicritical point (T_m, H_m), it is predicted that three second-order phase boundaries which emanate from (T_m, H_m) are described by

$$\frac{H - H_m}{H_m} = w_\alpha \left(\frac{T - T_m}{T_m} \right)^\phi \tag{2.21}$$

with the anisotropy crossover exponent $\phi \simeq 1.06$, where $\alpha = 1, 2, 3$ are correspondent to each phase boundary as labeled in Fig. 2.11 [26]. All phase boundaries are predicted to come into the first-order spin-flop line tangentially, and the coefficients w_α for each boundary are the same value, when the system has the same phase diagram. Katori *et al.* [24] estimated ϕ for $CsMnI_3$ and $CsNiBr_3$ by means of magnetization measurements. They concluded that the phase boundaries $\alpha = 1, 2$ and 3 are described by eqs. 2.21 within the extremely small area

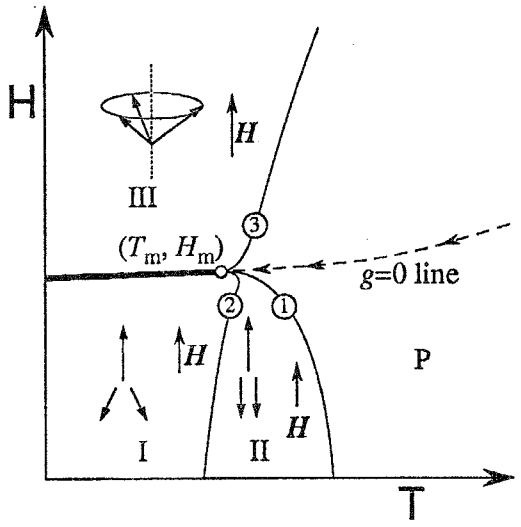

Figure 2.11: A schematic magnetic phase diagram of TAF with weak axial anisotropy. The magnetic field is applied along the c-axis. The thick line (the boundary between phase I and III) denotes the first-order spin-flop transition, and the thin curves indicate the second-order transition.

around the multicritical point. The critical behavior for the multicritical point (T_m, H_m) is predicted to be described by the chiral Heisenberg universality [26]. In Table 2.3, the experimental results of the critical exponents for phase transitions at T_{N1} and T_{N2} are shown. For the higher transition temperature T_{N2}, critical exponents are obtained as $\alpha = -0.05 \pm 0.15$ [35], $\beta_\perp = 0.35 \pm 0.01$ [32], $\gamma_\perp = 1.04 \pm 0.03$ and $\nu_\perp = 0.56 \pm 0.02$ [33]. These results are not consistent with the scaling relation $\alpha + 2\beta + \gamma = 2$. This discrepancy may be caused by the anisotropy crossover effect.

2.4 Purpose of this study

As seen in the previous section, the phase transition and critical behavior of the TAF depend on the anisotropy. Therefore, it is worth studying how the phase transition changes with the anisotropy. In the first half of this study, the magnetic anisotropy and the phase transition in the mixed system $CsMn(Br_xI_{1-x})_3$ are treated. The bromide ion concentration x was varied to control the macroscopic anisotropy of this system. The anisotropy vanishes on average at $x = x_c$.

The phase transition of $CsMnBr_3$ has been well investigated from the point of view of criticality by means of neutron scattering experiments and specific heat measurements

[29, 35, 28, 31, 49]. The critical exponents obtained (see Table 2.3) are in good agreement with values predicted for the chiral XY universality class. On the other hand, experimental studies of the chiral Heisenberg universality have been scarce, because no suitable model substance without anisotropy is available. The possibility of the experimental study of the chiral Heisenberg universality was pointed out for the weak-anisotropy case, such as that of $CsMnI_3$, under the appropriate magnetic fields [26].

When an external field is applied parallel to the c-axis, $CsMnI_3$ has a multicritical point at which three critical lines of the second-order phase transitions and the first-order spin-flop line meet as shown in Fig. 2.11 [24, 25]. Along the $g = 0$ line, where g is a scaling field, the system becomes isotropic in the spin space [26]. Thus, if both temperature and magnetic field (T, H) are varied along the locus $g = 0$, the critical behavior for the phase transition at the multicritical point should belong to the chiral Heisenberg universality class. In general, however, the locus $g = 0$ is not parallel to the temperature axis. Experimentally, it is difficult to obtain the $g = 0$ line and to vary both T and H keeping the condition $g = 0$. In order to investigate the critical behavior belonging to the chiral Heisenberg universality class, we need a TAF without magnetic anisotropy, for which the locus $g = 0$ corresponds to the temperature axis ($H = 0$). If the anisotropy of this system can be removed by controlling the bromine concentration x, the criticalities which belong to chiral Heisenberg universality class would be observed with only the temperature variation. This is the main aim of this study.

2.5 Magnetic measurements

2.5.1 Sample preparation and equipment

The single crystals of $CsMnBr_3$ and $CsMnI_3$ were grown by the vertical Bridgman method from the melt of equimolar mixtures of CsX and MnX_2 (X=Br and I) sealed in evacuated quartz tubes. The temperature at the center of the furnace was set at 650°C, and lowering rate was 3mm/hour. The source materials used were CsI and MnI_2 of 99.9% purity and $MnBr_2{\cdot}4H_2O$ of 99% purity (Soekawa Chemicals), and CsBr of 99.9% purity (Wako Pure Chemical Industries). To get manganese bromide, $MnBr_2{\cdot}4H_2O$ was dehydrated around 120°C in vacuum for three days. CsI, $MnBr_2$ and MnI_2 were very hygroscopic, so we treated them in the glove-box filled with dry nitrogen. After weighing, the materials were packed into the quartz tubes and dehydrated in vacuum near 150°C for three days, again.

Mixing single crystals of $CsMnBr_3$ and $CsMnI_3$ in a ratio of $x : 1 - x$, we prepared $CsMn(Br_xI_{1-x})_3$ by the Bridgman method. Single crystals of size 1~5cm^3 were obtained.

Each sample looks homogeneous, so that the gradients of bromine concentration are expected to be very small. The crystals are easily cleaved along the (1, 0, 0) plane. Samples were cut into pieces weighing 100~150mg and coated with Apiezon-N grease.

The susceptibility was measured by the Faraday method using a Cahn 2000 electrobalance and an electromagnet. An accuracy of 5% in the absolute value and 1% in the relative value is obtained for the temperature variation. To measure the perpendicular susceptibility $\chi_\perp$ accurately, we set the c-axis to be vertical so that the external field is always perpendicular to it. Since the value of $\chi_{//} - \chi_\perp$ is obtained by the torque measurement, we did not measure the susceptibility $\chi_{//}$ parallel to the c-axis.

The magnetic torque was measured using a torque meter (Yasunami YMT-H1) and an electromagnet. The torque meter used is an electric current-to-torque transducer type constructed for measuring torque values as small as $10^{-4} \sim 10^{-3}$dyne·cm. We measure the current which generates counter torque for keeping the orientation of the sample unchanged. The accuracy of the absolute value is approximately 1×10^{-7}emu and that of the relative value is 1%. The sample was placed such that the external field always lies in the (1, 1, 0) plane containing the c-axis. The experimental geometry is shown in Fig. 2.12. The electromagnet was rotated at the rate of 1.5°/sec for the measurements of torque curves. The phase diagrams were measured using a SQUID magnetometer (Quantum Design MPMS XL). The accuracy of the absolute value is approximately 5×10^{-9}emu.

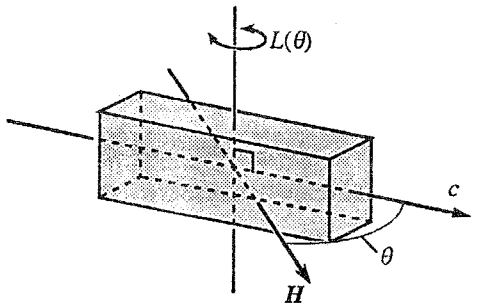

Figure 2.12: The experimental geometry of the torque measurements.

2.5.2 Magnetic measurements

Magnetic susceptibility

Figure 2.13 shows the temperature dependence of the susceptibility $\chi_\perp$ perpendicular to the c-axis for various bromine concentrations x. The applied magnetic field is 6kOe. All

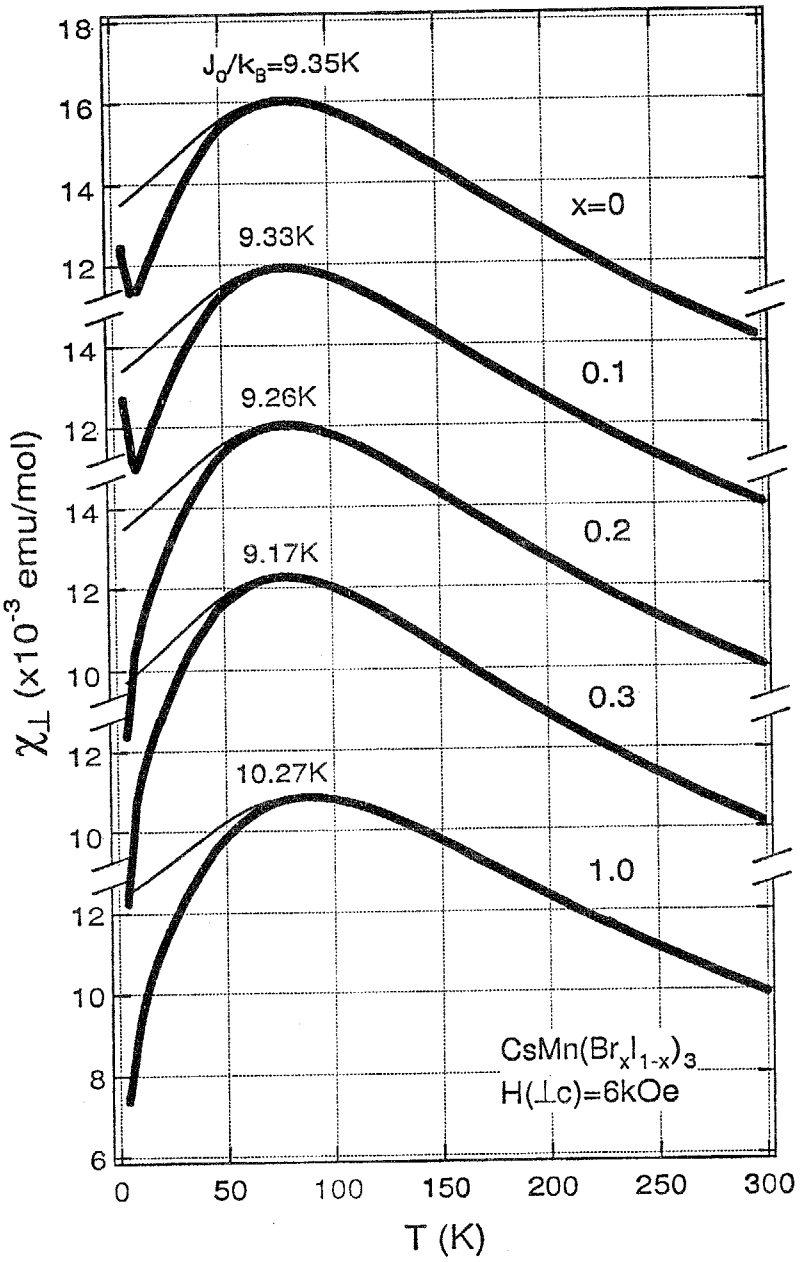

Figure 2.13: The temperature dependences of the perpendicular susceptibilities $\chi_\perp$ for the $CsMn(Br_xI_{1-x})_3$ system measured at H =6 kOe. Thee thick lines show the experimental results and thin solid lines represent fits of Fisher's theory to our data for $T > 90$ K.

susceptibility curves have the broad maxima at around $T = 80$ K which is characteristic of the one-dimensional Heisenberg antiferromagnets. In order to check the intrachain exchange interaction J_0, the susceptibility data above 90K are fitted to Fisher's theory [53] for the classical Heisenberg linear chain. His result is expressed as

$$\chi(T) = \frac{4N_A g^2 \mu_B^2 S(S+1)}{12 k_B T} \frac{1+u(K)}{1-u(K)} \tag{2.22}$$

with

$$u(K) = \coth K - \frac{1}{K}$$

and

$$K = \frac{1}{2}\frac{J_0}{k_B T}.$$

Since the spin value of the present system is $S = 5/2$, eq. 2.22 gives a good approximation to the high temperature susceptibilities. The values of J_0 obtained from the fitting are shown in Fig. 2.13. For $x \leq 0.3$, the value of J_0 slightly decreases with increasing x.

Figure 2.14 shows the susceptibilities $\chi_\perp$ at low temperatures. Phase transitions are clearly seen at the positions indicated by arrows. Sharp anomalies due to the phase transitions are indicative of the good homogeneity in the samples. For the sample with x=0, 0.1, 0.15 and 0.18, two phase transitions are observed. The perpendicular susceptibility decreases monotonically with increasing temperature, has the bend anomalies at T_{N2} and T_{N1} and then increases in the paramagnetic phase. This behavior is typical of the antiferromagnetically stacked TAFs for the weak axial anisotropy case [50, 51]. On the other hand, the single phase transition is observed at $T_N \approx 8.3$K, for the sample with $x = 0.2, 0.3$ and 1.0. The susceptibility increases monotonically and changes its gradient at the Néel temperature. This behavior is typical of the planar anisotropy case [52].

Torque measurements

The magnetic torque $L(\theta)$ is given by $L(\theta) = -\partial F/\partial\theta$, where F is the free energy of the system and θ is the angle between the external field H and the c-axis. In the paramagnetic phase, $L(\theta)$ is expressed as

$$L(\theta) = -\frac{\partial F}{\partial \theta} = -\frac{1}{2}\left(\chi_{//} - \chi_\perp\right) H^2 \sin(2\theta), \tag{2.23}$$

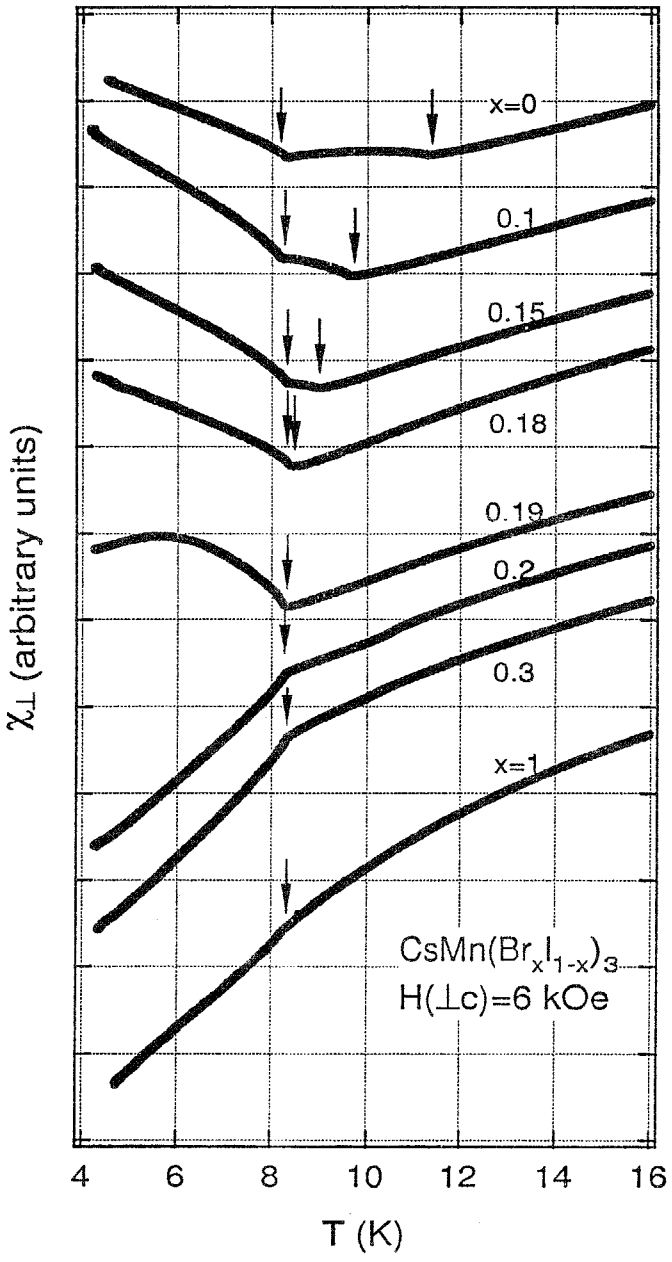

Figure 2.14: The temperature dependences of the perpendicular susceptibilities $\chi_\perp$ for various values of x in the phase transition region. The arrows indicate phase transition points.

where $\chi_{//}$ and $\chi_{\perp}$ are the susceptibilities for $H//c$ and $H \perp c$, respectively. Thus, we can obtain $\Delta\chi = \chi_{//} - \chi_{\perp}$ through the torque measurement.

Nagata *et al.* [54] demonstrated that in the one-dimensional antiferromagnet with the isotropic g-factor, $\Delta\chi$ does not change its sign over the entire temperature range when the anisotropy is due to the pseudodipolar interaction, while for the single ion anisotropy, $\Delta\chi$ changes its sign at

$$T = J_0 S(S+1)/k_B.$$

We confirmed by ESR measurements that the g-factor in $CsMnBr_3$ and $CsMnI_3$ is almost equal to 2.00, irrespective of the magnetic field direction. We measured the torque on both the compounds up to room temperature and observed that $\Delta\chi$ does not change its sign. This shows that the origin of the magnetic anisotropy in the present systems is due to the pseudodipolar interaction, and is not the single ion anisotropy.

Figure 2.15 shows the temperature dependence of $\Delta\chi$ defined by $\Delta\chi = -2L(\theta = 45°)/H^2$. When the torque is proportional to $H^2 \sin 2\theta$ in the ordered state, $\Delta\chi$ is equal to $\chi_{//} - \chi_{\perp}$. Phase transitions are observed at the same temperatures as those detected by the susceptibility measurements. For $x < 0.19$, the lower temperature phase transition (T_{N2}) is less clear than that at the higher temperature (T_{N1}).

Figure 2.16 shows $\Delta\chi$ at 14K. We see that the value of $\Delta\chi$ increases linearly in x, and it becomes zero at $x_c = 0.19$. Since $\Delta\chi$ is proportional to the magnitude of the anisotropy, the result indicates that the pseudodipolar interaction ΔJ generally varies as $\Delta J \propto (x_c - x)$, *i.e.*, the anisotropy changes from the axial type to the planar one at $x = x_c$.

In the antiferromagnetically stacked TAF, the 120° structure in the basal plane gives $\chi_{//} > \chi_{\perp}$, while the triangular structure in the plane including the c-axis gives $\chi_{//} < \chi_{\perp}$. Thus, it is concluded that the anisotropy is of the axial type for $x < x_c = 0.19$, and of the planar type for $x > x_c$, and that the ground state spin structures for $x < x_c$ and $x > x_c$ are the same as those of $CsMnI_3$ and $CsMnBr_3$, respectively.

Figure 2.17 (a), (b) and (c) shows the torque curves at 4.2 K for x=0.18, 0.19 and 0.20, respectively. The torque at low fields for $x = 0.18$ and 0.20 is roughly described by eq. 2.23. With increasing the external field, the peaks shift towards the $\theta = 0$ for $x = 0.18$ and towards the $\theta = \pm 90°$ for $x = 0.20$. This behavior is interpreted as resulting from the fact that the plane of the triangular spin structure (spin plane) moves slightly so as to become perpendicular to the external field. The anomaly near $\theta = 0°$ for $x = 0.18$ is attributed to the "single domain to multidomain" transition for the orientation of the spin plane, which

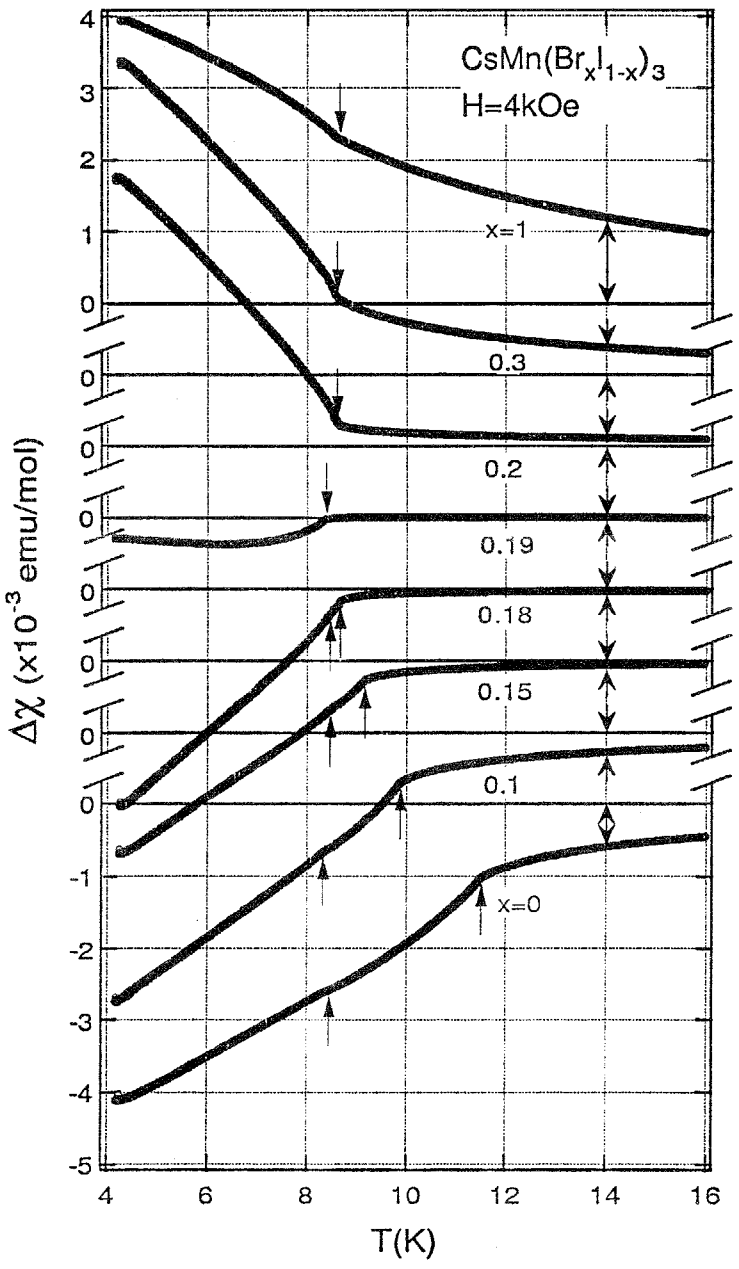

Figure 2.15: The temperature variation of $\Delta\chi$ defined by $\Delta\chi = \chi_{\parallel} - \chi_{\perp}$ for the system $CsMn(Br_xI_{1-x})_3$ in the phase transition region measured at $H = 4$ kOe. Transition points are indicated by arrows.

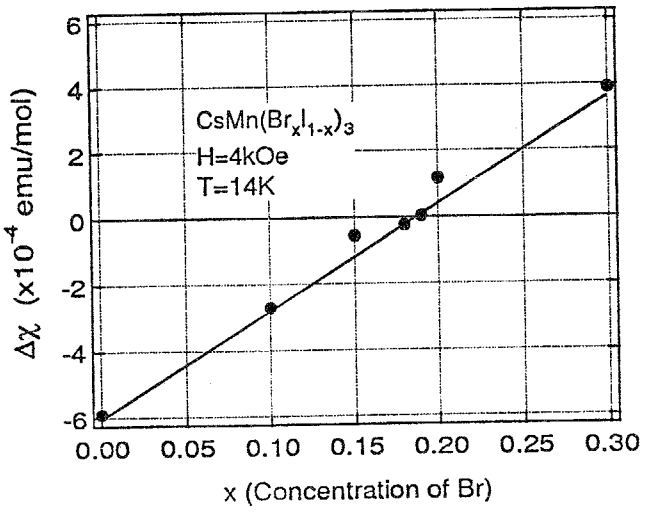

Figure 2.16: The differential susceptibility $\Delta\chi$ as a function of the bromine concentration x at $T = 14$ K. The solid line is a guide to the eye.

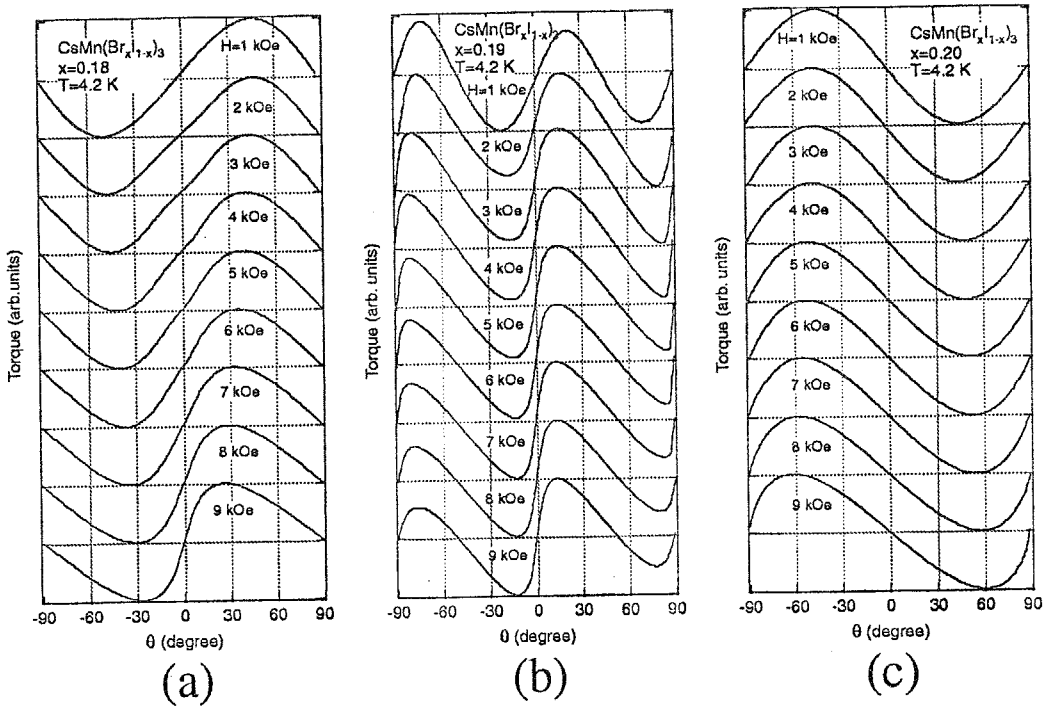

Figure 2.17: Torque curves at $T = 4.2$ K for (a) $x = 0.18$, (b)$x = 0.19$ and (c) $x = 0.20$.

is characteristic of the triangular spin structure including the c-axis [51]. The torque for $x_c = 0.19$ has a large component with a period of 90°. This implies that the anisotropy vanishes at $x = x_c$, and that the spin structure is mainly affected by the external field.

Figure 2.18 shows the phase diagram of the transition temperatures versus bromine concentration x obtained from the susceptibility and torque measurements. Experimental results

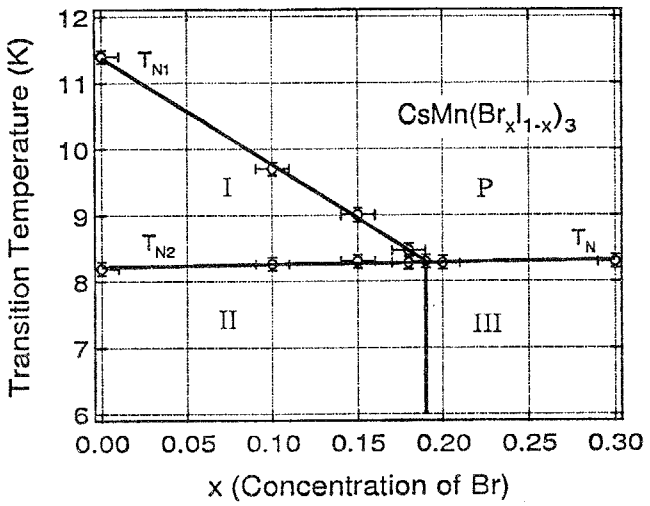

Figure 2.18: The phase diagram for the transition temperature versus the bromine concentration x.

are plotted by open circles with error bars. In this figure, phase P denotes paramagnetic phase. The phase labeled as III is the phase of the 120° structure in the c-plane. For $x < x_c$, the intermediate (IM) phase and the low temperature (LT) phase are labeled as I and II, respectively. The magnetic structures in phases I and II are the two sublattice ferrimagnetic structure and the triangular structure in the plane including the c-axis, respectively. As seen from Fig. 2.18, the intermediate phase I becomes narrower with increasing x, and vanishes at $x_c = 0.19$. The I-II and P-III phase boundaries are almost constant at 8.3 K. The boundary between phases II and III may be parallel to the temperature axis, because no phase transition was observed below T=8.3 K for x=0.18, 0.19, and 0.20.

Miyashita and Kawamura studied the phase transition in the anisotropic Heisenberg model on the triangular lattice by means of the Monte Carlo method [55]. They showed that the temperature range of the IM phase decreases on decreasing the magnitude of the axial anisotropy, and that the P-IM and IM-LT phase boundaries meet tangentially at the isotropic limit. In the present system, we could not observe such a tangential confluence of

both phase boundaries within the experimental resolution.

2.5.3 Variations of phase diagrams

As seen in Figs. 2.2, 2.3, 2.8, 2.10, the magnetic phase diagram of TAF is strongly affected by the magnetic anisotropy. For $CsMn(Br_xI_{1-x})_3$ system, the macroscopic anisotropy can be controlled by varying bromine concentration x with keeping the magnitude of J_0 and J_1. Thus, the continuous change of the phase diagram from that of $CsMnI_3$ (Fig. 2.10) to that of $CsMnBr_3$ (Fig. 2.8) and new ordered phases which do not exist in the pure system are expected. As was seen in Fig. 2.3 (a), for TAF with weak planar anisotropy undergoes the spin-flop transition at $H_c^{\perp}$ described by eqs. 2.14. For this mixed system, the spin-flop transition field $H_c^{\parallel}$ or $H_c^{\perp}$ should be lower than that of $CsMnI_3$, $H_c^{\parallel} \simeq 5.3$ T [24]. We classify the magnetic phase diagrams of this mixed system in three cases, (i) axial anisotropy case ($x = 0, 0.1, 0.15$ and $0.18 < x_c$), (ii) isotropic case ($x = 0.19 = x_c$) and (iii) planar anisotropy case ($x = 0.20$, 0.25 and $1 > x_c$).

(i) Axial anisotropy case ($x < x_c$)

Figure 2.19 shows the magnetic phase diagram of $CsMnI_3$ obtained in the present measurements. In Fig. 2.19, solid circles and triangles indicate the transition points which are determined from temperature and field dependence of magnetization. In ref [24], it was observed that the tangential approach of the second order phase boundaries in the vicinity of the multicritical point. In this experiment, however, such behavior was not observed, because of insufficiency of the signals of magnetization anomaly in the vicinity of the multicritical point. Figure 2.20 shows the magnetic phase diagrams for the samples with x =0.1, 0.15 and 0.18. Magnetic field is applied parallel to the c-axis. The phase boundary which corresponds to the spin-flop phase transition were detected by field variation, and transition points were assigned at the field which gives the local maximum on dM/dH. Three second-order phase boundaries were detected by temperature variations. With increasing bromine concentration x, multicritical point (T_m, H_m) shifts toward $(T_{N2}, 0)$, the spin-flop phase boundary is lowered, and the area of intermediate phase is shrunken. While the phase boundary between paramagnetic and spin-flop phase, and between intermediate and low-temperature phase seem to be fixed. The gradient of the spin-flop phase boundary shows decrease with increasing x, so that in the isotropic limit, this boundary should be parallel to the temperature axis.

(ii) Isotropic case ($x = x_c$)

The phase diagram for the sample with $x = x_c = 0.19$ is shown in Fig. 2.21. For this sample,

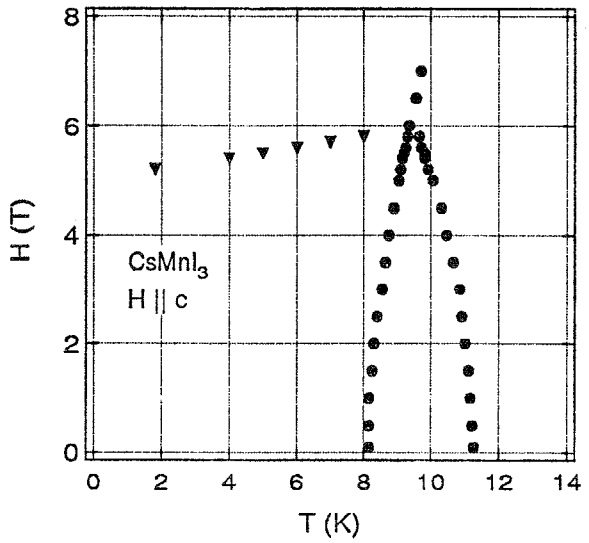

Figure 2.19: Phase diagram of $CsMnI_3$ in the field parallel to the c-axis. Solid circles and squares denote the transition points determined from temperature dependence and magnetization process, respectively.

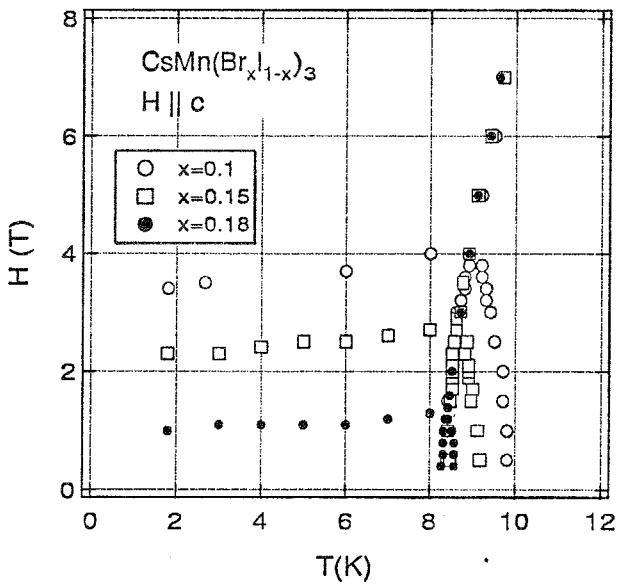

Figure 2.20: The magnetic phase diagrams in the field parallel to the c-axis. Open circles, open squares and solid circles indicate the transition points for the samples with $x = 0.10$, 0.15 and 0.18, respectively.

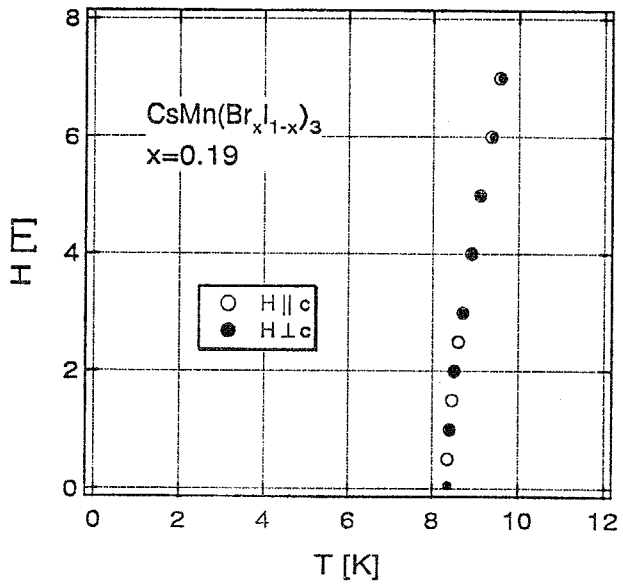

Figure 2.21: The phase diagram for the sample with $x = x_c = 0.19$. Open and closed circles are the transition points for the magnetic field parallel and perpendicular to the c-axis.

no spin-flop transitions were detected in the field dependence of the magnetization for both field direction $H \parallel c$ and $H \perp c$. Thus, in the ordered phase, the normal of the spin plane in which spins form the 120° structure should always point to the field direction. The fact that the phase boundary does not depend on the field direction, shows the isotropic nature of this sample. The critical behavior of the phase transition at zero field should belong to the chiral Heisenberg universality class.

(iii) Planar anisotropy case ($x > x_c$)

The phase diagrams for the systems with $x = 0.20$ and 0.25 in the field perpendicular to the c-axis are shown in Fig. 2.22. In Fig. 2.22, closed and open circles denote the transition points of $x = 0.20$ and 0.25, respectively. It should be noted that these systems have the spin-flop transitions. With increasing bromine concentration, the spin-flop transition field H_{sf} is increased, and the area of the intermediate phase labeled as 5 in Fig. 2.3 is enlarged.

The spin-flop phase transition fields H_{sf} for various x are summarized in Fig. 2.23. The values of H_{sf} were obtained by extrapolating the spin-flop phase boundary to 0 K. The spin-flop fields H_{sf} for TAF with axial and planar anisotropies are expressed by eqs. (2.12) and (2.14), respectively. Since J_0 is almost constant as shown in Fig. 2.13 and anisotropy ΔJ

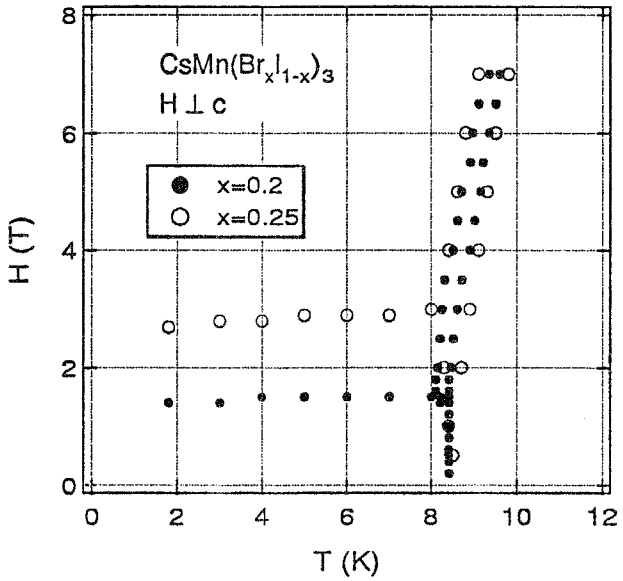

Figure 2.22: The phase diagram for the samples with $x = 0.20$ and 0.25 in the field perpendicular to the c-axis. Closed and open circles denote the transition points of $x = 0.20$ and 0.25, respectively.

can be assumed to be proportional to $|x_c - x|$ as seen in Fig. 2.16, the spin-flop field for the present system should be expressed as,

$$H_{sf} = H_{sf}(0)\sqrt{|x_c - x|/x_c}, \tag{2.24}$$

where $H_{sf}(0) = 5.04$ T denotes spin flop field of $CsMnI_3$ which is determined from the present measurements, and plotted by a cross in Fig. 2.23. The agreement between the solid line and data indicates that H_{sf} assigned on this measurements are fairly well.

Figure 2.24 (a) shows the phase diagram of $CsMnBr_3$ in the field perpendicular to the c-axis. In Fig. 2.24, solid squares and circles are the transition points determined from field and temperature variations of magnetization. For two phase boundaries, crossover exponents ϕ^+ and ϕ^- defined by eqs. (2.20) were estimated as $\phi^+ = 0.94 \pm 0.05$ and $\phi^- = 0.97 \pm 0.05$ for higher and lower phase boundaries, respectively. Dashed lines in Fig. 2.24 (a) are the boundaries given by $\phi^+ = 0.94$ and $\phi^- = 0.97$. Figure 2.24 (b) is the log-log plot of transition field versus reduced temperature defined as $t = |T_N - T|/T_N$ with $T_N = 8.35$ K. The solid line is a fit to the power law $H_t \propto (|T - T|/T_N)^{\phi^\pm}$, with $\phi^+ = 0.94 \pm 0.05$, $\phi^- = 0.97 \pm 0.05$ in the field range $0.5\text{T} \leq H \leq 4\text{T}$. The obtained exponents are slightly smaller than the predicted value $\phi = \phi^+ = \phi^- = 1.04$. In this fitting, the low-field data for $H < 0.5$ T

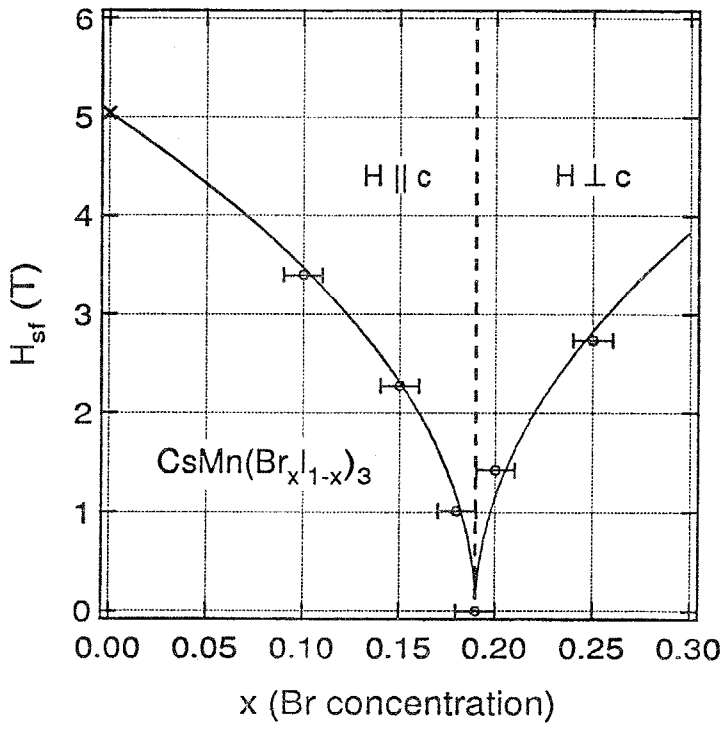

Figure 2.23: Spin-flop transition fields for various bromine concentration x. Field directions are $H \parallel c$ and $H \perp c$ for $x \leq x_c$ and $x_c \leq x$, respectively. Error bars indicate the resolution of the chemical analysis for x. Solid lines indicate the function $H_{sf} = H_{sf}(0)\sqrt{|x_c - x|/x_c}$ which is described in text.

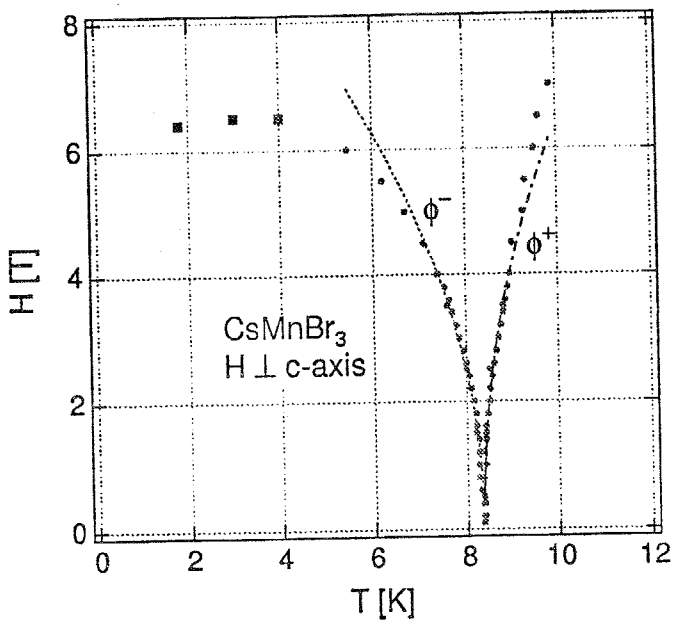

(a)

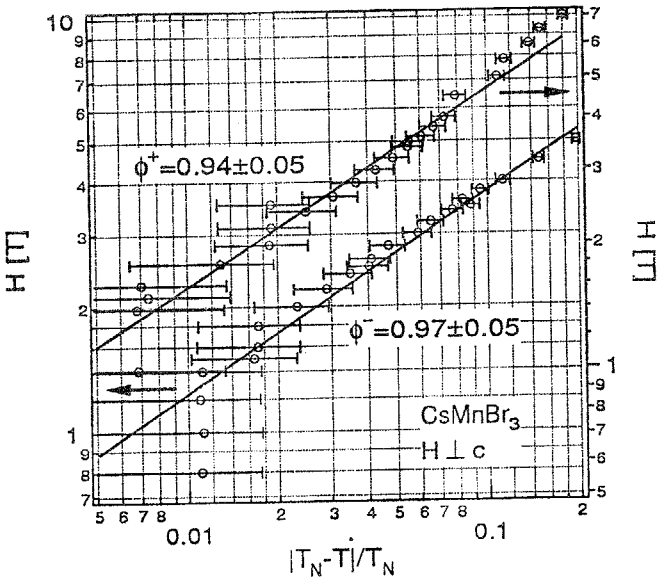

(b)

Figure 2.24: (a) Phase diagram of $CsMnBr_3$ in the field perpendicular to the c-axis. Solid squares and circles are the transition points determined from temperature and field dependence of magnetization. Dashed lines are the boundaries given by the crossover exponents $\phi^+ = 0.94$ and $\phi^- = 0.97$. (b) Log-log plot of the transition field and the reduced temperature defined by $|T_N - T|/T_N$ with $T_N = 8.35$ K. Solid lines indicate the fits of power law given by eqs. (2.20) to the present data in the field region $0.5\text{T} \leq H \leq 4\text{T}$.

is excluded, since it is difficult to distinguish the successive phase transition points in the vicinity of tetracritical point. It shoud be noted that the experimental reports of crossover exponets around the tetracritical point of $CsMnBr_3$ are conflicting each other [23, 52, 49]. The cause of the discrepancy among these results is still unclear.

2.5.4 Summary of this section

Magnetic phase transitions in the triangular antiferromagnetic system $CsMn(Br_xI_{1-x})_3$ have been studied by susceptibility and torque measurements. The phase diagram for the ordering temperature and bromine concentration x was obtained. With increasing x, the higher transition temperature decreases linearly with x, and the intermediate phase vanishes at $x_c = 0.19$. The magnetic anisotropy changes from the axial (easy-axis) type to the planar (easy-plane) type at $x = x_c$, where the system becomes isotropic. Magnetic phase diagrams for temperature v.s. magnetic field also obtained by magnetization measurements up to 7 T. Systematic change of the H-T phase diagram is observed with controlling x. The spin-flop transition is observed both in the axial and weak planar anisotropy cases. In the present system, the spin-flop field H_{sf} is described as $H_{sf} = 5.04\sqrt{|x_c - x|/x_c}$[T].

2.6 Neutron scattering for $CsMn(Br_{0.19}I_{0.81})_3$

As seen in the previous section, for $CsMn(Br_xI_{1-x})_3$, the magnitude and the sign of the anisotropy are systematically controlled by varying the bromine concentration x. With increasing x, the higher transition temperature T_{N1} decreases in proportion to x, so that the intermediate phase becomes narrower and vanishes at $x_c = 0.19$. The anisotropy changes from the axial type to the planar one at $x = x_c$. The result indicates that in $CsMn(Br_{0.19}I_{0.81})_3$ the interaction is almost isotropic on average. Then, we can expect that the phase transition at zero field belongs to the chiral Heisenberg universality class.

In order to investigate the spin structure and the critical behavior in $CsMn(Br_{0.19}I_{0.81})_3$, we carried out neutron scattering experiments.

2.6.1 Equipment

Neutron scattering experiments were performed on the triple-axis spectrometers ISSP-PONTA and HER installed at the research reactor JRR-3M in the Japan Atomic Energy Research Institute (JAERI) Tokai. The spectrometers were used in the double-axis mode to determine the magnetic structure in the ordered state and to observe the critical behavior. The θ-2θ scans to determine the magnetic structure were mainly carried out on PONTA. For the

experiments on the PONTA spectrometer, the experimental conditions were as follows. Pyrolytic graphite (002) reflections were used for the monochromator. To remove higher-order neutrons, a pyrolytic graphite filter was set before the sample. Incident neutron energy was fixed at 14.6meV. The horizontal collimation sequence was chosen as 15'-10'-10'-open. On the HER spectrometer, we determined the critical exponent for the sublattice magnetization β of $CsMn(Br_{0.19}I_{0.81})_3$. The HER spectrometer was installed at the C1-1 port on the C1 guide tube of the liquid-hydrogen-cooled cold neutron beam. For the monochromator, pyrolytic graphite (002) reflection was also used. The angle divergence of the beam incident to the monochromator was fixed at 6'. The second, third and forth collimators were chosen as 10', 20' and open, respectively. Incident neutron energy was fixed at 4.99meV.

The single crystal of $CsMn(Br_{0.19}I_{0.81})_3$ with the shape of a triangular prism of 5mm in width and 5mm in length was used. The sample was mounted in an ILL-type orange cryostat with its [110] and [001] axes in the scattering plane. Sample temperature was measured with a Ge resistance thermometer and was controlled within the accuracy of 0.01~0.001K.

2.6.2 Results

Magnetic structure

$CsMn(Br_{0.19}I_{0.81})_3$ undergoes a phase transition at $T_N = 8.3$K. To determine the spin structure of the ordered state, we first measured the integrated intensities of the Bragg reflections observed at $\boldsymbol{Q}$ =(1/3, 1/3, 1), (2/3, 2/3, 1), (4/3, 4/3, 1), (5/3, 5/3, 1), (1/3, 1/3, 2) and (2/3, 2/3, 2) at 2K. These Bragg reflections indicate that the magnetic unit cell in the c-plane is enlarged $\sqrt{3} \times \sqrt{3}$ times. Since the magnetic anisotropy is negligible in the present system, it is considered that spins form the 120° spin structure in the ordered state. When the spin planes make the angle ϕ with the c-plane as illustrated in Fig. 2.25, and they are in multidomain states with respect to the c-axis, the integrated intensity of the magnetic Bragg scattering for $\boldsymbol{Q} = (h, h, \ell)$ with $h = n/3$, $\ell \neq 3n$ is given by

$$I \propto \frac{|f(\boldsymbol{Q})|^2}{\sin 2\theta} d^2_{(h,k,\ell)} S^2 \left[\left\{ 2\left(\frac{h}{a}\right)^2 + \left(\frac{\ell}{c}\right)^2 \right\} (1 + \sin^2\phi) + \left(\frac{2h}{a}\right)^2 \cos^2\phi \right] \qquad (2.25)$$

and $I = 0$ for integer h, where 2θ is the scattering angle, $f(\boldsymbol{Q})$ is the magnetic form factor, $d_{(h,k,\ell)}$ is the spacing of the (h, k, ℓ) lattice plane, and a and c are lattice constants. For $f(\boldsymbol{Q})$, we used the spherical magnetic form factors calculated by Watson and Freeman [94]. The lattice constants a and c are determined from the (110) and (002) nuclear reflections as

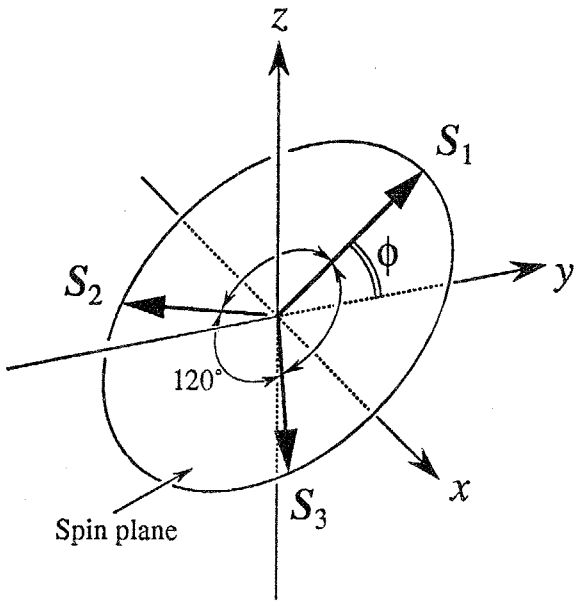

Figure 2.25: The spin structure in the ordered state. The angle ϕ denotes the angle between the spin plane and the c-plane. The x- and y-axis are taken in the c-plane.

$a = 8.032$Å and $c = 6.799$Å. Minimizing the reliability factor R given by

$$R = \sum_{h,k,\ell} |I_{\rm calc}(h,k,\ell) - I_{\rm obs}(h,k,\ell)| \,/\, \sum_{h,k,\ell} I_{\rm obs}(h,k,\ell),$$

we obtain $\langle \cos^2 \phi \rangle = 0.362$, *i.e.*, $\langle \phi \rangle = 53°$, where $\langle \cdots \rangle$ denotes the spatial average. In Table 2.4, we show the experimental and calculated intensities of several Bragg reflections together with the calculated intensities for $\phi = 0°$ and 90°. In Table 2.4, the Bragg intensities are normalized to that of the (1/3, 1/3, 1) reflection. The spin structures for $\phi = 0°$ and 90° correspond to those of $CsMnBr_3$ and $CsMnI_3$. We see from Table 2.4 that the spins form the 120° structure neither in the c-plane nor in the plane including the c-axis, but in the plane making an angle of 53° with the c-plane on average.

When the directions of the spin planes have the isotropic distribution, the average of $\cos^2 \phi$ is given by $\langle \cos^2 \phi \rangle = 1/3$, which leads to $\langle \phi \rangle = 55°$. This angle is very close to $\langle \phi \rangle = 53°$ obtained by minimizing the R-factor. Thus we can interpret the experimental results as indicating that the spin planes are almost isotropically distributed in the present system. This is consistent with the fact that the anisotropy is nearly negligible.

(h,k,ℓ)	I_{obs} (T=2K)	$I_{calc}(\langle\cos^2\phi\rangle = 0.362)$	$I_{calc}(\phi = 0°)$	$I_{calc}(\phi = 90°)$
$(\frac{1}{3},\frac{1}{3},1)$	1	1	1	1
$(\frac{2}{3},\frac{2}{3},1)$	0.678	0.691	0.573	0.797
$(\frac{4}{3},\frac{4}{3},1)$	0.298	0.296	0.200	0.383
$(\frac{5}{3},\frac{5}{3},1)$	0.210	0.190	0.123	0.250
$(\frac{1}{3},\frac{1}{3},3)$	0.178	0.178	0.197	0.161
$(\frac{2}{3},\frac{2}{3},3)$	0.144	0.125	0.132	0.118
		R=2.15%	R=12.8%	R=11.4%

Table 2.4: Experimental and calculated intensities of several magnetic Bragg reflections in $CsMn(I_{0.81}Br_{0.19})_3$. They are normalized to (1/3, 1/3, 1) reflections. The calculated intensities for $\phi = 0°$and 90° are also shown for comparison.

Critical behavior

The magnetic Bragg intensity I_{Bragg} is proportional to the square of the sublattice magnetization. In the critical region below T_N, I_{Bragg} is described as

$$I_{Bragg} \propto \left(\frac{T_N - T}{T_N}\right)^{2\beta}, \tag{2.26}$$

where β is the critical exponent of the sublattice magnetization.

For strict correction of the background and critical scattering, the scan along the $(h,h,1)$ direction was performed. An example of the scan performed at $T = 8.266(1)$K ($T < T_N$) is shown in Fig. 2.26.

The profiles obtained around (1/3, 1/3, 1) at different temperatures were fitted to the following form,

$I_{obs}(h,k,\ell)$ =Magnetic Bragg scattering with Gaussian shape
+ Diffuse signal with Lorentzian shape
+ Background.

Figure 2.27 shows a log-log plot of the magnetic Bragg peak intensity for $Q = (1/3, 1/3, 1)$ versus reduced temperature $(T_N - T)/T_N$ with $T_N = 8.291(1)$K. Fitting eqs. 2.26 to the experimental data between $0.005 < (T_N - T)/T_N < 0.1$, we obtain $\beta = 0.28 \pm 0.02$. This value agrees with the value $\beta = 0.30 \pm 0.02$ predicted for the chiral Heisenberg universality class [46, 47].

For a more decisive experiment, measurement of the critical exponent α for the specific heat is desired, because the exponent $\alpha = 0.24 \pm 0.08$ predicted for the chiral Heisenberg universality class differs significantly from those of the conventional three-dimensional ($\alpha \simeq -0.121$) and chiral XY ($\alpha = 0.34 \pm 0.06$) universality classes.

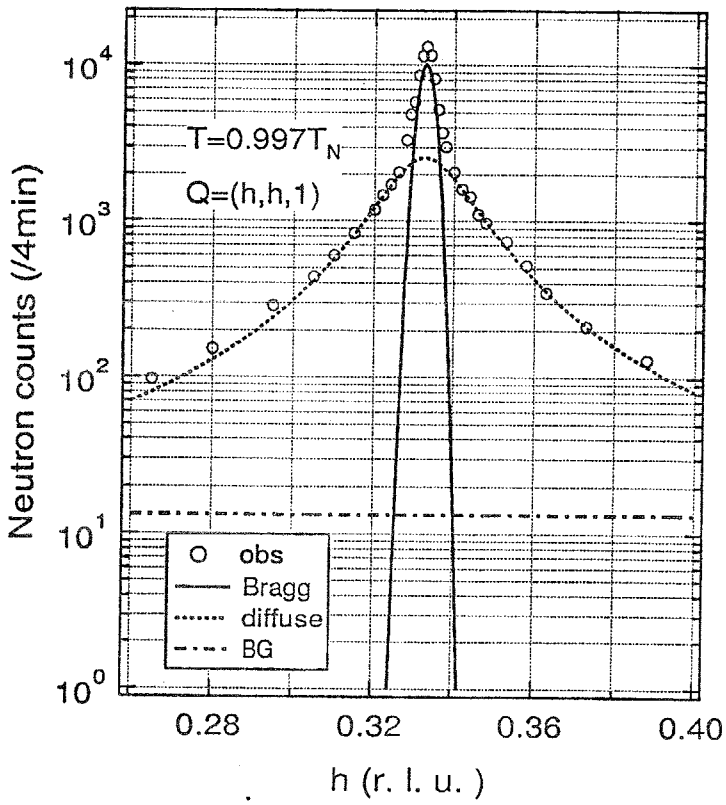

Figure 2.26: An example of a scan along the $(h, h, 1)$ line around the $(1/3, 1/3, \ell)$ reflection on a logarithmic scale. Solid and dashed curves and the dot-dashed line indicate the magnetic Bragg scattering, diffuse scattering, and background, respectively.

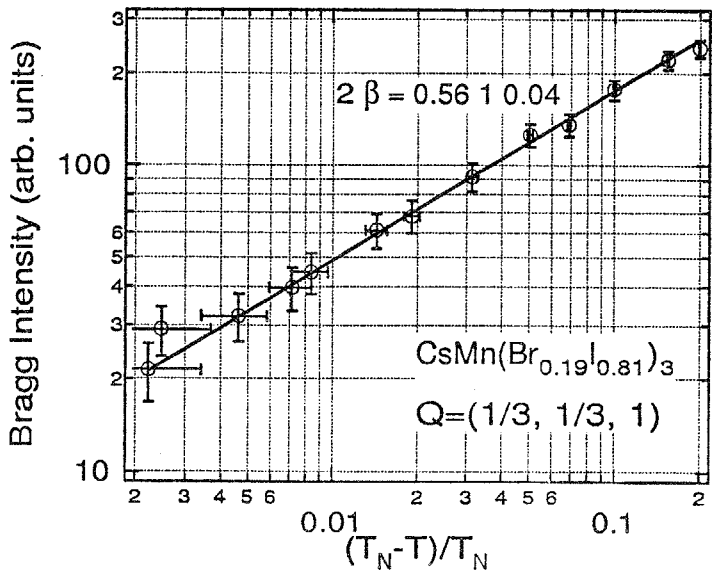

Figure 2.27: A log-log plot of the magnetic Bragg peak intensity $I_{\rm Bragg}$ versus reduced temperature $(T_{\rm N}-T)/T_{\rm N}$ for the $\boldsymbol{Q}=(1/3,1/3,1)$ reflection. The solid line is a fit to the power law $I_{\rm Bragg} \propto (1-T/T_{\rm N})^{2\beta}$, with $2\beta = 0.56 \pm 0.04$ and $T_{\rm N} = 8.291(1)$ K.

2.7 Summary of this section

The elastic neutron scattering experiments were performed on a triangular antiferromagnet $CsMn(Br_{0.19}I_{0.81})_3$, for which magnetic measurements revealed that the magnetic anisotropy is negligible. In the ordered state below $T_{\rm N} = 8.29$K, the spin planes in which the spins lie with the 120° structure are tilted from the basal plane, and the average of the tilting angle ϕ is evaluated as $\langle \cos^2 \phi \rangle = 0.362$, *i.e.*, $\langle \phi \rangle = 53°$. This result suggests that the spin planes have almost isotropic distribution.

The critical exponent β for the sublattice magnetization is obtained as $\beta = 0.28 \pm 0.02$, which agrees with the predicted one for the chiral Heisenberg universality class.

Chapter 3

$S = \frac{1}{2}$ triangular antiferromagnetic system $CsCu_{1-x}Co_xCl_3$

3.1 $CsCuCl_3$

In this chapter, the study of the magnetic phase transitions and the spin structure of the ordered phase of the triangular antiferromagnetic system $CsCu_{1-x}Co_xCl_3$ are described. Before going to the main subject of this study, we review the experimental and the theoretical studies of $CsCuCl_3$ which is the base compound of this impurity doped system.

3.1.1 Crystal and magnetic structure of $CsCuCl_3$

$CsCuCl_3$ is one of the hexagonal ABX_3-type compounds. Among such hexagonal ABX_3-type TAF compounds, $CsCuCl_3$ has remarkable features in the crystal structure, the spin structure of the ground state, the field dependences of the spin configurations and the anomalous critical behavior [60, 64, 62, 47]. The mysterious properties of $CsCuCl_3$ have fascinated many experimentalists and theorists over a few decades.

Since the Cu^{2+} ion is Jahn-Teller-active, $CsCuCl_3$ undergoes a structural phase transition at T_t =423 K. Below T_t, the crystal structure of $CsCuCl_3$ is distorted from the $CsNiCl_3$ structure (space group $P6_3/mmc$) to another hexagonal structure ($P6_122$) and the unit cell is enlarged 3 times along the c-axis as shown in Fig. 3.1. In the low-temperature crystal structure phase, all $CuCl_6$-octahedra are elongated along one of the principal axes, and the longest axes form a helix along the c-axis with a repeat length of six [65, 66, 67, 68, 69, 70]. Figure 3.2 indicates the distortion of an octahedral chain in the low-temperature phase. In Fig. 3.2, a, b and c indicate the routes for the path through the Cu-Cl-Cu-Cl$\cdots$ chain. The elongated axis changes on the Cu-Cl-chain in order $c \to b \to a \to c \to b \to a \to \cdots$ as indicated by the thick line of Fig. 3.2.

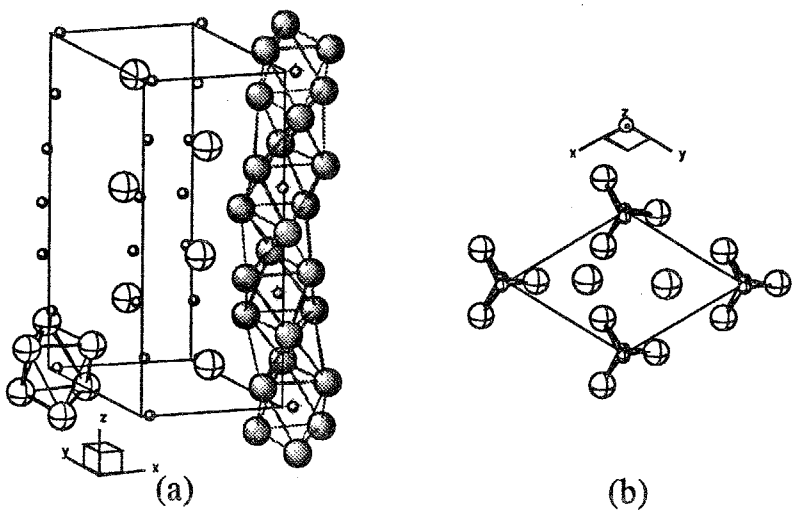

Figure 3.1: The crystal structure of $CsCuCl_3$. In order to make it easy to see, $CuCl_6$-chain and the ab-plane are shown separately as (a) and (b), respectively. Lattice constants at room temperature are determined as $a = 7.216$ Åand $c = 18.117$ Å.

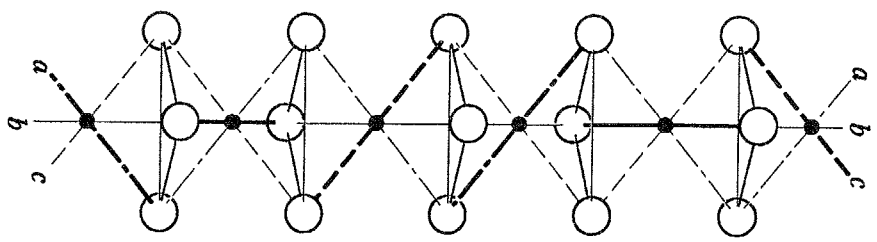

Figure 3.2: Distortion sequence of $CuCl_6$ octahedral chain. The thick line indicates the elongated axes. a, b and c indicates the each of three Cu-Cl-Cu-Cl$\cdots$ chains.

The low-symmetry crystal structure can lead to the antisymmetric interaction of the Dzyaloshinsky-Moriya (D-M) type between the neighboring spins in the $CuCl_6$ chain with the D-vector parallel to the c-axis. The magnetic anisotropy is of the planar type due to the pseudo-dipole interaction [73]. Taking into account the D-M interaction and anisotropy, the Hamiltonian of $CsCuCl_3$ is well described by [73],

$$\mathcal{H} = -\mu_B \sum_{\ell,j}(\boldsymbol{S}_{\ell j}\mathbf{g}_j\boldsymbol{H}) - 2J_0\sum_{\ell,j}(\boldsymbol{S}_{\ell j}\cdot\boldsymbol{S}_{\ell j+1}) + 2J_1\sum_{\ell,m,j}(\boldsymbol{S}_{\ell j}\cdot\boldsymbol{S}_{mj}) - \sum_{\ell,j}(\boldsymbol{d}_{jj+1}\cdot[\boldsymbol{S}_{\ell j}\times\boldsymbol{S}_{\ell j+1}]) + 2\Delta J_0\sum_{\ell j}(S^z_{\ell j}S^z_{\ell j+1}). \quad (3.1)$$

The first term is the Zeeman energy. The second and third term denote the intrachain and the interchain exchange interactions which are ferromagnetic and antiferromagnetic, respectively. The fourth term is the D-M interaction with the $\boldsymbol{d}_{jj+1} = (0, 0, d)$ parallel to the c-axis and the last term is the pseudo dipolar interaction which causes small planar-type anisotropy. The signs and the values of the parameters in Hamiltonian 3.1 have been estimated by several groups. Adachi *et al.* determined the magnetic structure in the ordered state and concluded the sign of the intrachain, and the interchain interaction [71]. Hyodo *et al.* [76] and Tazuke *et al.* [72] estimated the exchange coupling constants J_0 and J_1 using high temperature expansion method from their experimental results of the optical birefringence and the magnetic susceptibility, respectively. Tanaka *et al.* calculated the ESR modes which are observable in the field parallel to the c-axis [73], and pointed out that the existence of the last term of the Hamiltonian (3.1) with fitting the experimental results of Palme *et al* [74]. The magnitude of the exchange interactions was determined as $J_0/k_B = 28$ K and $J_1/k_B = -4.9$ K for intrachain and interchain, respectively. Since the period of the helical structure $2\pi/\theta$ is determined by the ratio of J_0 to d as

$$\tan\theta = \frac{d}{2J_0}, \quad (3.2)$$

the magnitude of D-M interaction is determined as $d = 5.0$ K by using the result of the neutron scattering experiment, $\theta = 5.1°$.

$CsCuCl_3$ undergoes a magnetic phase transition at $T_N = 10.5$ K at zero field [71, 75, 76, 77]. In the ordered phase, spins lie in the c-plane and form the 120° structure, while along the c-axis, a long-period, i.e., about 71 layers of the c-plane, helical incommensurate structure is realized, due not to the competition between effect of the nearest and next nearest neighbor interactions along the c-axis, but to the competition between the ferromagnetic interaction and the D-M interaction in the chain [71]. The magnetic structure in the ground state of $CsCuCl_3$ is shown in Fig. 3.3

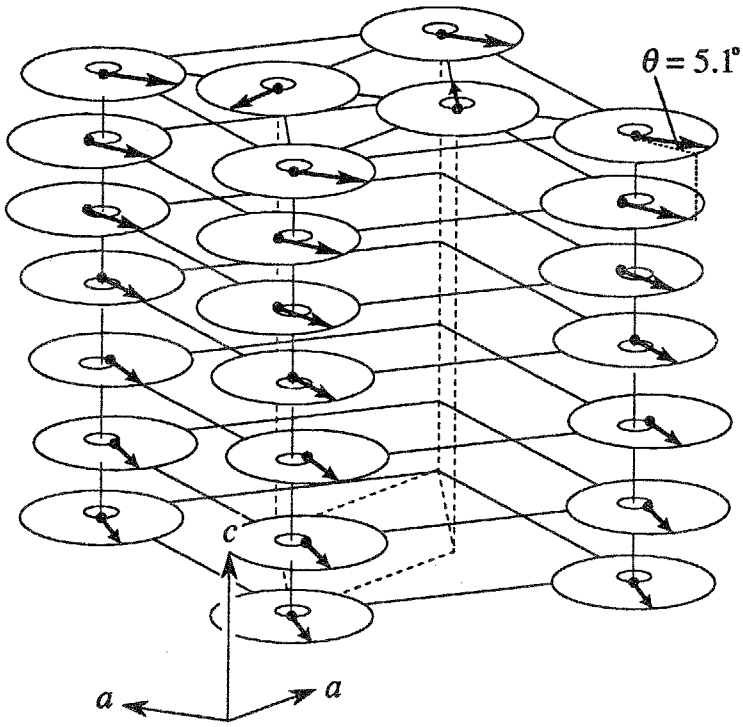

Figure 3.3: The magnetic structure of $CsCuCl_3$ in the ground state. Solid circles at the root of each spins indicate the displacement from the c-axis of Cu^{2+} ion. The angle $\theta \simeq 5.1°$ denotes the pitch of the helical structure along the c-axis per Cu-site.

3.1.2 Magnetic properties in the external field

Within the mean-field theory, the D-M interaction and the planar anisotropy favors the umbrella-like structure as show in Fig. 3.4 in the entire field range up to saturation for the field parallel to the c-axis. However, in 1978, Motokawa and his coworkers [78] reported a small magnetization jump which indicates a phase transition at $H_c = 12.5$ T and $T = 1.1$ K for $H \parallel c$-axis, as shown in Fig. 3.5 (a). The magnetic phase diagram of the field versus temperature was also determined for $H \parallel c$ as shown in Fig. 3.5 (b) (the case of $H \perp c$ is mentioned below in this section). The high-field phase is stable in the entire temperature range of the ordered state. The origin of this field induced phase transition was left unclear for 15 years. In 1992, using spin wave approximation, Nikuni and Shiba [79] argued that the coplanar structure, as shown in Fig. 3.4 (d), is stabilized in high magnetic fields due to the quantum fluctuations, so that the transition from the umbrella-type structure to a coplanar structure shown in Fig. 3.4 (d) , can occur at H_c. The competition between the small planar anisotropy and the quantum fluctuation gives rise to the phase transition at H_c. The coplanar spin structure predicted for the high-field phase was confirmed by means of neutron scattering [80, 81] and ESR measurements [82] in pulsed high magnetic fields, and ^{133}Cs NMR measurements [83].

For the applied field perpendicular to the c-axis, the situation is more complicated, since the helical incommensurate (IC) wave length of the spins is affected by the field. The magnetic behavior in the low field region is well described by the mean-field theory [84], i.e., the pitch θ of the IC helical structure along the c-axis is decreased with increasing field, quadratically to the applied field strength H as follows,

$$\theta = \theta_0 \left[1 + \frac{1}{2} \left(\frac{2H/H_s}{1 + \frac{2J_0}{9J_1}} \theta_0^2 \right)^2 \right]^{-1}, \tag{3.3}$$

where θ_0 indicates the IC wave length in zero field. However, mean-field theory can not explain the existence of the magnetization plateau at around one third of the saturation field H_s which is shown in Fig. 3.5 and the strange field dependence which have the plateau-like behavior around $H \sim H_s/3$. Figure 3.6 shows the experimental results of the field variation of IC wave length $q(= \theta)$ measured by Mino *et al.* [80] and Nojiri *et al* [86]. In order to explain the behavior of the magnetization curve and the field variation of q, Jacobs *et al.* [84] and Nikuni and Jacobs [85] studied the quantum effects on the spin reorientation and succeeded to reproduce the field variation of q (see Fig. 3.6 (b)) and the magnetization plateau around one third of saturation field $H \sim H_s$ (see Fig. 3.7). Recently, Werner *et al.* [87] reported detailed specific heat results which indicates the existence of the new IC phase

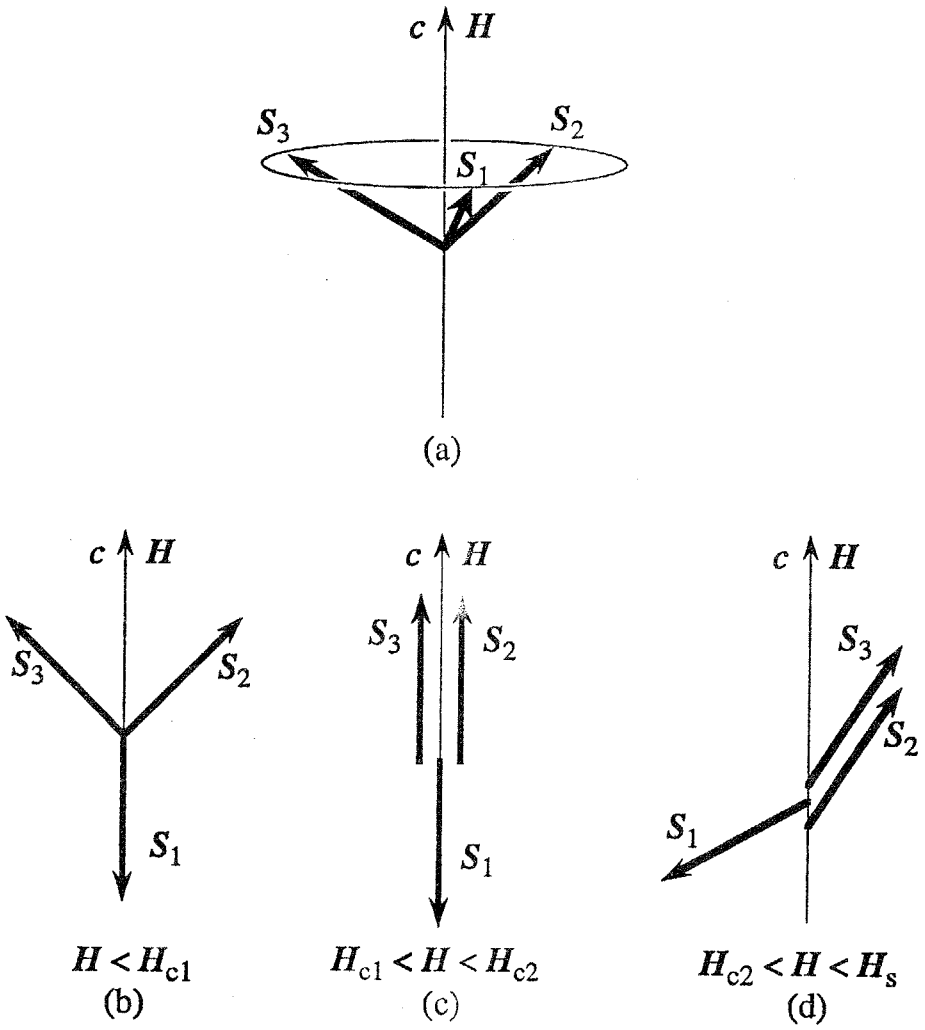

Figure 3.4: Various spin structures in magnetic fields for the ferromagnetically stacked triangular Heisenberg antiferromagnet. (a) Umbrella -type structure, (b) low-field coplanar structure, (c) collinear structure, and (d) high-field coplanar structure.

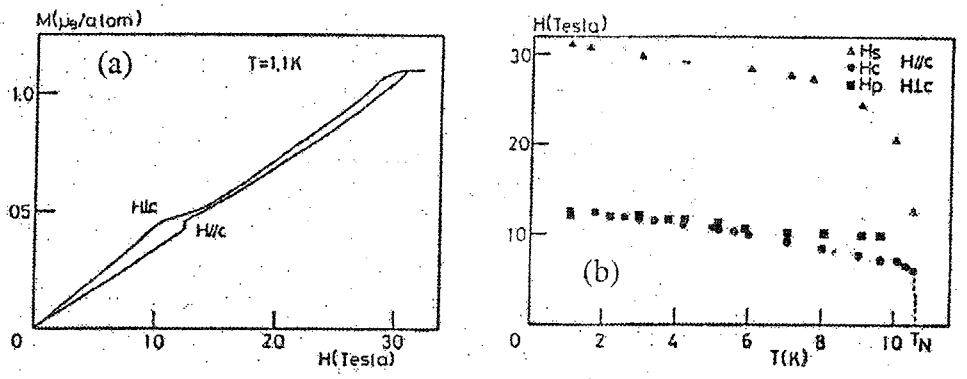

Figure 3.5: (a) Magnetization process of $CsCuCl_3$ for the field parallel and perpendicular to the c-axis. (b) Temperature dependence of saturation field H_s, critical field H_c for $H \parallel c$ and plateau field H_p for $H \perp c$. (quoted from ref. [78].)

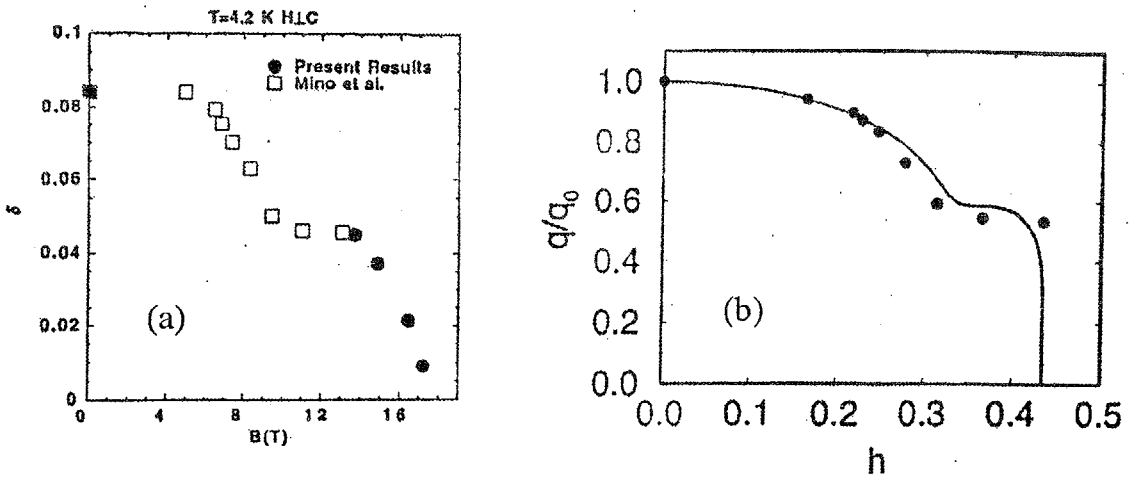

Figure 3.6: The (a) experimental and (b) theoretical results of field dependence of the helical IC spin structure wave length. In (a), δ denotes the IC wavelength per chemical unit along the c-axis. Since the chemical unit length along the c-axis corresponds to six Cu-sites, $\delta = 6\theta$. In (b), h is defined as $h \equiv H/H_s$. (quoted from ref. [86] and ref. [85]).

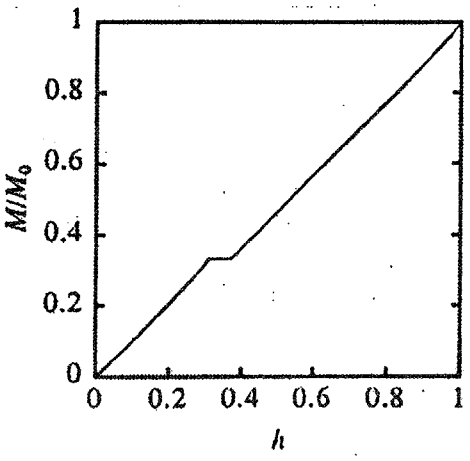

Figure 3.7: The magnetization curve for $H \perp c$ with taking account of quantum correction to the spin direction with the appropriate parameter $J_0/k_B = 28$ K and $J_1/k_B = 4.9$ K. (quoted from ref. [84].)

with different IC wave length along the c-axis in the vicinity of the Neél temperature under the appropriate field region. Stimulated by this result, Jacobs and Nikuni [88] investigated the phase diagram for $H \perp c$ using Landau expansion of the order parameter, and Schotte *et al.* [89] performed the neutron scattering experiments and clarified the magnetic structure of the new IC phase.

As mensioned above, $CsCuCl_3$ provides a lot of surprising magnetic properties which reflects the small magnitude of spin S and the small magnetic anisotropy.

3.2 Purpose of this study

For the isotropic two-dimensional (2D) triangular antiferromagnets, the equilibrium condition for the three sublattice spins, $\boldsymbol{S}_1$, $\boldsymbol{S}_2$ and $\boldsymbol{S}_3$, coupled with the antiferromagnetic nearest neighbor interaction J is described by $\boldsymbol{S}_1+\boldsymbol{S}_2+\boldsymbol{S}_3 = \frac{\boldsymbol{H}}{6J}$ within the mean-field theory. Thus, the spin structure is not determined uniquely, and infinite spin structures are degenerate in the ground state, which is called "non-trivial continuous degeneracy [79]".

Using spin-wave approximation, Chubukov and Golosov [90] investigated the quantum effects on the spin ordering of the two-dimensional isotropic TAF in magnetic fields. They argued that with increasing magnetic field, the Heisenberg TAF undergoes a successive phase transition as shown in Fig. 3.4 (b), (c) and (d) in that order. The intermediate collinear spin structure is stabilized in a finite field range $H_{c1} < H < H_{c2}$, where the critical fields

H_{c1} and H_{c2} are a little smaller and greater than one-third of the saturation field H_s, respectively. Thus the magnetization plateau is expected to be in the field range. However, such a successive phase transition is not observed in $CsCuCl_3$. We infer that the planar anisotropy described as ΔJ_0 in eqs. 3.1 prevents the presence of the low-field coplanar (see Fig. 3.4 (b)) and the intermediate collinear spin structures (Fig. 3.4 (c)). If the planar anisotropy were reduced, the successive phase transition predicted by Chubukov and Golosov or an unexpected new phase might be observed, This is the main motivation of the present study.

$CsCoCl_3$ is well known as a pseudospin-$\frac{1}{2}$ Ising TAF [91, 92]. Thus, we assume that, on average, Co^{2+} ions substituting for Cu^{2+} ions in $CsCu_{1-x}Co_xCl_3$ reduce the planar anisotropy. In the following section, procedures and results of the magnetization and magnetic torque measurements for $CsCu_{1-x}Co_xCl_3$ are described.

3.3 Magnetic measurements of $CsCu_{1-x}Co_xCl_3$

3.3.1 Sample preparation and equipment

The crystals of $CsCu_{1-x}Co_xCl_3$ were prepared as follows: the source materials used were CsCl of 99% purity, $CuCl_2{\cdot}2H_2O$ of 99% purity (Wako Pure Chemical Industries, Ltd.). In preparing $CsCuCl_3$, $CuCl_2{\cdot}6H_2O$ and CsCl were dehydrated separately by heating in vacuum for three days at $T \simeq 80°C$ and $T \simeq 150°C$, respectively. After being weighed, they were put into a quartz tube and dehydrated by heating in vacuum at $T \simeq 80°C$ for three days. In preparing $CsCoCl_3$, we first dissolved equimolar CsCl and $CoCl_2{\cdot}6H_2O$ in water and then vaporized the water by heating. The obtained $CsCoCl_3$ powder was put into a quartz tube and dehydrated by heating in vacuum at $T \simeq 200°C$ for three days. Single crystals of $CsCuCl_3$ and $CsCoCl_3$ were grown by the Bridgman technique from the melt. The temperature at the center of the furnace was set at 550°C for $CsCuCl_3$ and 650° for $CsCoCl_3$. Mixing single crystals of $CsCuCl_3$ and $CsCoCl_3$ in the ratio $1-x : x$, we prepared $CsCu_{1-x}Co_xCl_3$ by Bridgman technique. Single crystals of size $\sim 1cm^3$ were obtained. The crystals are easily cleaved along the (1, 0, 0) plane. The crystals were cut into pieces weighing 50~100mg for magnetic measurements. The concentration of the cobalt ion x was analyzed by emission spectrochemical analysis after the measurements were carried out. Since the resolution of the chemical analysis is higher than 1×10^{-3} ppm, the reliability of cobalt ion concentration x is ± 0.0001.

The magnetization was measured down to 1.8K in magnetic fields up to 7T using a SQUID magnetometer (Quantum Design MPMS XL). A horizontal sample rotator was used to obtain the magnetization for various field directions. The magnetic torque was measured

by the same method as described in the previous chapter. High field magnetization was measured by the induction method using the pulsed high magnetic field. Measurements were performed at Institute for Materials Research, Tohoku University (Sendai).

3.3.2 Results of magnetization measurements

Figure 3.3.2 shows the magnetization process for the sample with x=0.032 at various temperatures. The external field is applied parallel to the c-axis. For $T = 1.8\,\mathrm{K}$, the magnetization jumps at H_c=3.6 T. The field at which there is an inflection point in the magnetization is assigned to the transition field. The transition field H_c decreases with increasing temperature. We observe the presence of a small spontaneous magnetization for $H < H_c$, which is also confirmed by the torque measurements, as discussed below. The magnitude of the spontaneous magnetization M_s at $T = 1.8\,\mathrm{K}$ is estimated by extrapolating the magnetization curve in the field region of $1.5\,\mathrm{T} \leq H \leq 3.3\,\mathrm{T}$ to zero (dotted line in Fig. 3.3.2) as $M_s \simeq 2.5\times10^{-3}\mu_B$/atom.

The temperature dependence of the magnetization for $H \parallel c$ on the sample with x=0.032 is shown in Fig. 3.9. The small anomaly at $T = 12\,\mathrm{K}$ is due to an instrumental problem. When the applied field is higher than 4 T, a single phase transition occurs at $T_{N1} \simeq 9.5\,\mathrm{K}$, and the transition temperature is almost independent of the external field. On the other hand, for $H \leq 3\mathrm{T}$, we can see another anomaly in the low-temperature side, which is indicative of the second phase transition. In Fig. 3.9, the temperature at which dM/dT gives the local maximum is assigned to the transition temperature T_{N2}. The transition temperature T_{N2} shifts rapidly to the high-temperature side with decreasing external field. Sharp anomalies due to the phase transitions indicate good homogeneity of the sample.

The phase transition data for the samples with x=0.015, 0.023 and 0.032 are summarized in Fig. 3.10, where open circles, triangles and closed circles indicate the transition points for the samples with x=0.015, 0.023 and 0.032, respectively. We label each phase as shown in Fig. 3.10. With increasing x, the phase boundary between the paramagnetic phase and phase I shifts toward the low-temperature side. On the other hand, the area of phase II becomes enlarged with increasing x. For the sample with $x = 0.005$, we could not observe phase II. Thus, we infer that there exists a critical concentration x_c to produce phase II. In the area of phase I, we could not detect any anomalies indicative of the phase transition in the magnetization data.

We measured magnetization curves at various field directions for the sample with $x = 0.03$. The dM/dH versus H curves obtained at $T = 1.8\,\mathrm{K}$ are shown in Fig. 3.11, where θ denotes the angle between the external field and the c-axis. The value of dM/dH at around zero field is maximum at $\theta = 0°$, and decreases with increasing $|\theta|$. This indicates that the steep

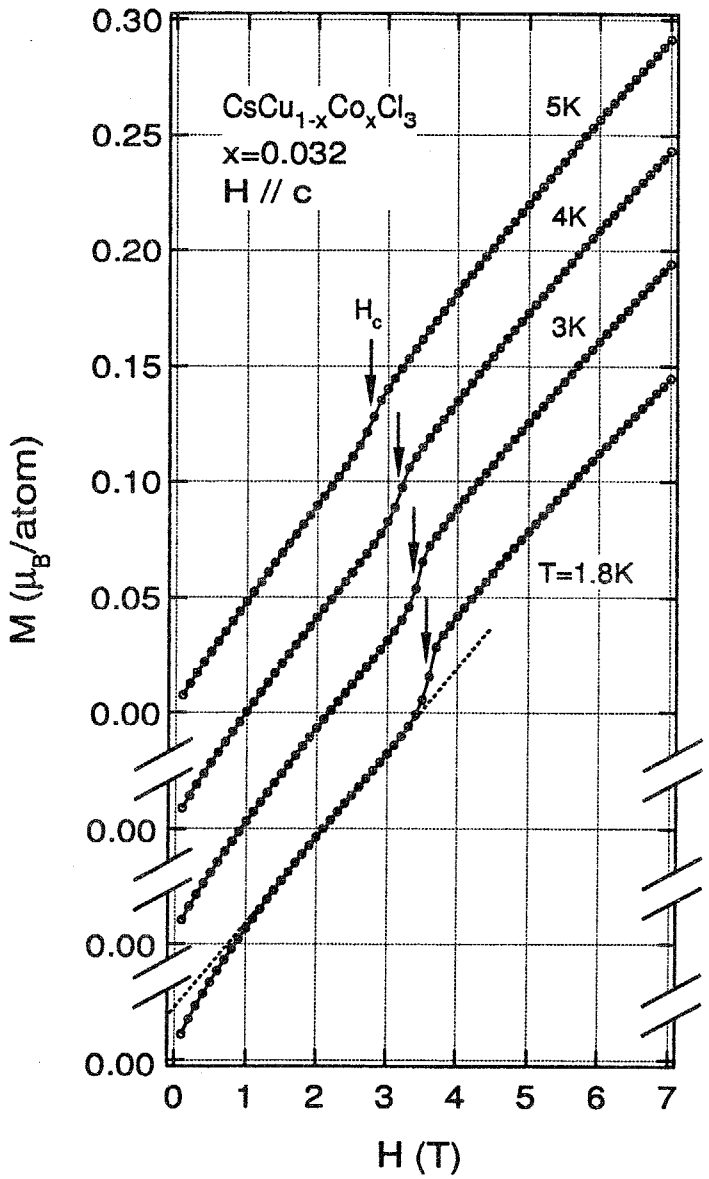

Figure 3.8: Field dependences of magnetization for the sample with $x = 0.032$ measured at various temperatures. The external field is applied parallel to the c-axis. Transition fields are indicated by arrows. The dotted line on the data of $T = 1.8\,\mathrm{K}$ denotes the extrapolation of the magnetization curve in the $1.5\,\mathrm{T} \leq H \leq 3.3\,\mathrm{T}$ to zero.

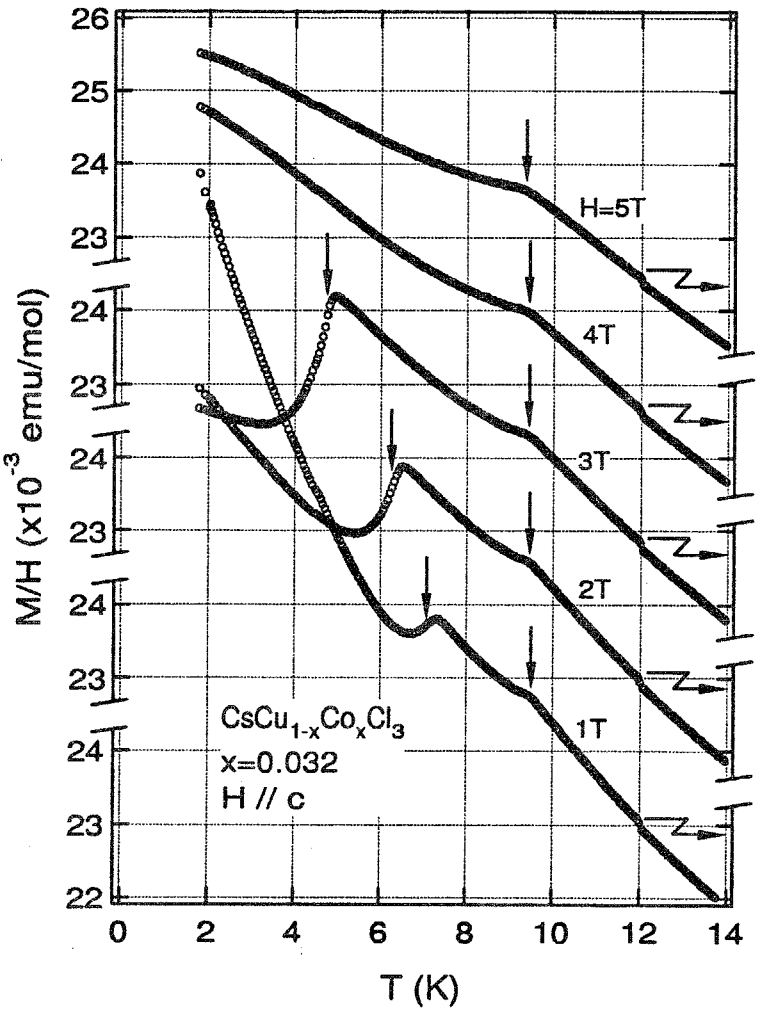

Figure 3.9: Temperature variations of the magnetization for the sample with $x = 0.032$ at the various external fields parallel to the c-axis. Transition temperatures are indicated by arrows.

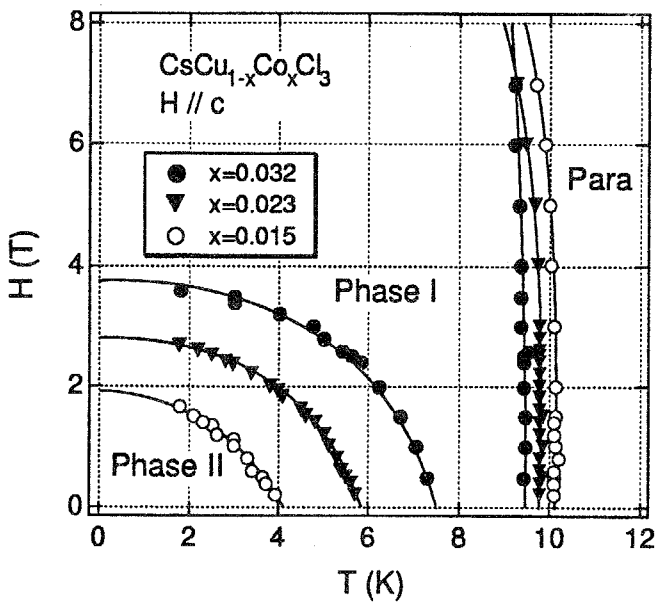

Figure 3.10: The magnetic phase diagram of $CsCu_{1-x}Co_xCl_3$ for the magnetic field parallel to the c-axis. Open circles, triangles and closed circles correspond to the transition points for x =0.015, 0.023 and 0.032, respectively

increase of the magnetization near zero field for $H||c$ is attributable not to the paramagnetic impurity, but to the small spontaneous magnetization along the c-axis. The transition from phase II to phase I can be observed at the peak position of dM/dH.

Figure 3.12 shows the transition field H_c as a function of the angle θ. The solid line is a visual guide. We can observe that the transition field H_c changes continuously with θ, and has a minimum at $\theta = 0°$ ($H||c$) and a maximum at $\theta = \pm 90°$ ($H \perp c$). If the transition field H_c is determined by the c-axis component of the external field, H_c is proportional to $1/\cos\theta$. However, the transition field obtained for $H \perp c$ is finite. This finding indicates that both the field components parallel and perpendicular to the c-axis are responsible for the phase transition. Figure 3.13 is a schematic phase diagram obtained by the present study. We can observe that phase II is surrounded by the phase I, and the principal character of the phase diagram is not affected tremendously by the direction of the external field.

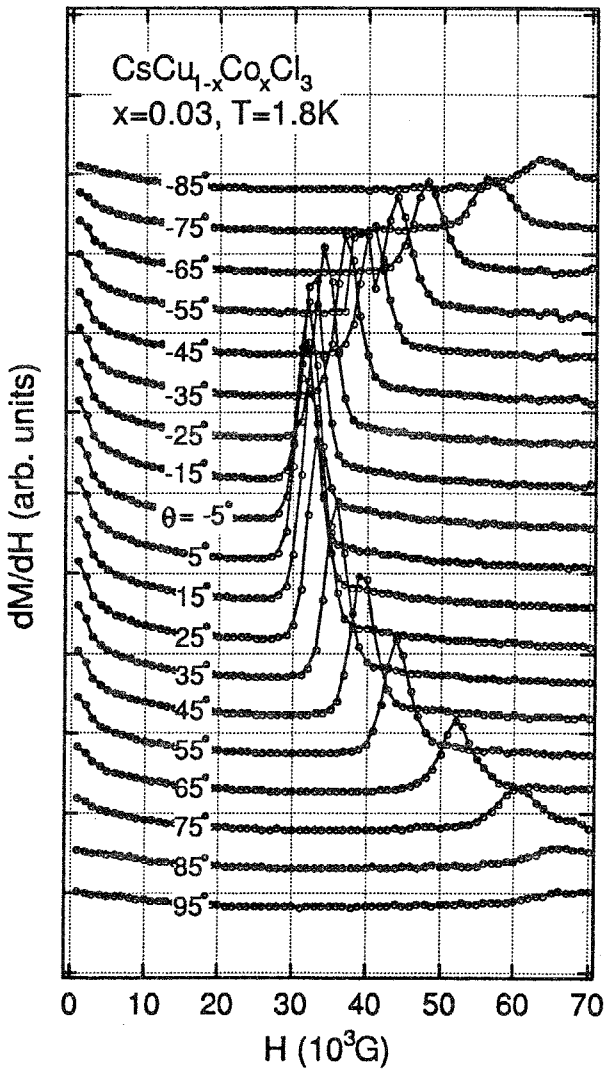

Figure 3.11: The dM/dH versus H measured in various field directions and at $T = 1.8$ K for $x = 0.03$. θ denotes the angle between the external field and the c-axis.

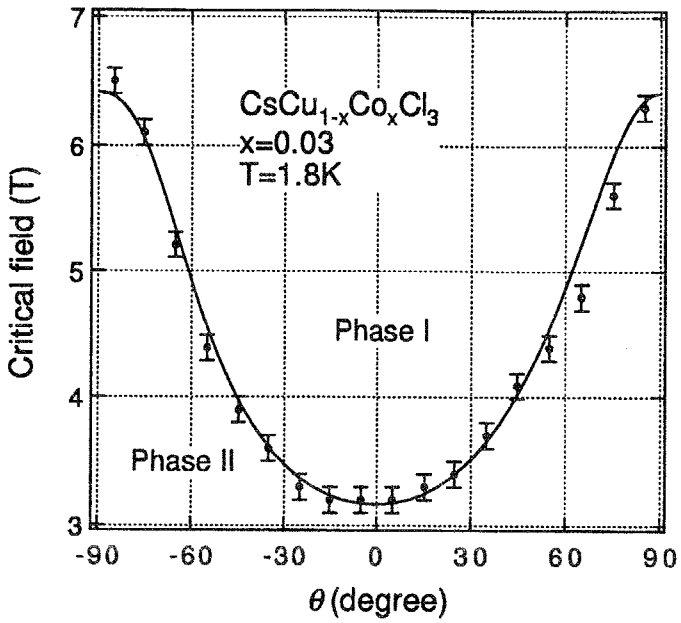

Figure 3.12: The angular dependence of the transition field H_c measured at $T = 1.8\,\mathrm{K}$ for the sample with $x = 0.03$. The solid line is a visual guide.

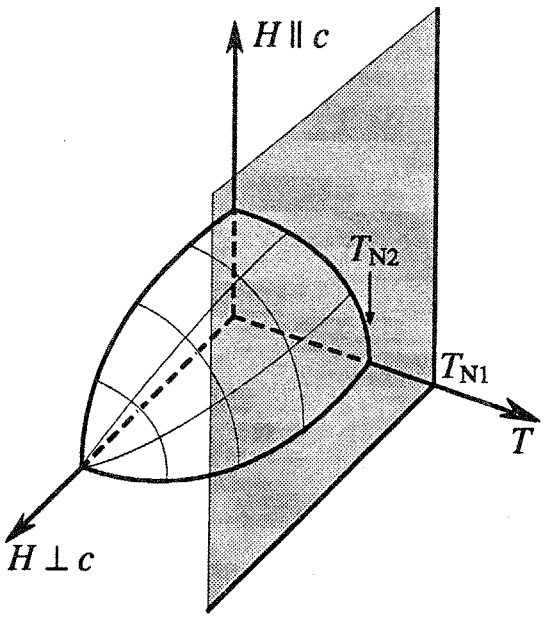

Figure 3.13: The schematic phase diagram of the present system for $0.015 \leq x \leq 0.032$.

3.3.3 Torque measurements

The magnetic torque $L(\theta)$ is given by $L(\theta) = -\partial F/\partial\theta$, where F is the free energy of the system and θ is the angle between the external field H and the c-axis. When the torque $L(\theta)$ is proportional to $H^2\sin2\theta$, which is satisfied in the paramagnetic phase, $L(\theta)$ is expressed as

$$L(\theta) = -\frac{\partial F}{\partial\theta} = -\frac{1}{2}\left(\chi_{\parallel} - \chi_{\perp}\right) H^2\sin2\theta, \tag{3.4}$$

where $\chi_{\parallel}$ and $\chi_{\perp}$ are the susceptibilities for $H \parallel c$ and $H \perp c$, respectively. Thus, we can obtain the difference of the susceptibilities $\chi_{\parallel} - \chi_{\perp}$ through the torque measurement.

Figure 3.14 shows the torque curves for $CsCuCl_3$ and $CsCu_{1-x}Co_xCl_3$ with x=0.015, 0.023 and 0.032, respectively. The external field of $H = 0.9\,\mathrm{T}$ is applied. The dashed and solid curves for $CsCu_{1-x}Co_xCl_3$ are the torque curves in phase I and II, respectively. The magnetic torque for $CsCuCl_3$ and those in the phase I for x=0.015 and 0.023 (dashed curves in Fig. (b) and (c), respectively) are proportional to $H^2\sin2\theta$. From the torque curve, we see $\chi_{\parallel} < \chi_{\perp}$ in the ordered phase of $CsCuCl_3$. On the other hand, for x=0.015 and 0.023, $\chi_{\parallel} > \chi_{\perp}$ in phase I. In phase II, the peak of the torque curve shifts toward $\theta = \pm90°$, and the curve resembles the letter "N". The torque curve can be understood in terms of the small spontaneous magnetization parallel to the c-axis, which produces the torque proportional to $-H\sin\theta$ for $-90° \leq \theta \leq 90°$. The spontaneous magnetization does not exist in phase I, because the torque is described by eq. (3.4).

Figure 3.15 shows the temperature dependence of $\Delta\chi$ defined by

$$\Delta\chi = -2L(\theta = 45°)/H^2. \tag{3.5}$$

The data were collected at $H = 0.5\,\mathrm{T}$ and $0.3\,\mathrm{T}$ for $CsCu_{1-x}Co_xCl_3$ and $CsCuCl_3$, respectively. In the paramagnetic phase in which the torque is proportional to $H^2\sin2\theta$, $\Delta\chi$ is equal to $\chi_{\parallel} - \chi_{\perp}$. Phase transitions are detected at almost the same temperatures as those observed in the magnetization measurements. In the paramagnetic phase, $\Delta\chi$ changes its sign from minus to plus with increasing x, and its magnitude increases. It is considered that $\Delta\chi$ in the paramagnetic phase is almost proportional to the anisotropy, because the difference between the g-factors parallel and perpendicular to the c-axis is small in $CsCuCl_3$, i.e., $g_{\perp} - g_{\parallel} \simeq 0.02$ [82, 93]. Therefore, the present result indicates that, on average, with increasing x, the anisotropy changes from a planar type to an axial one and that phase II appears when the anisotropy is of the axial type.

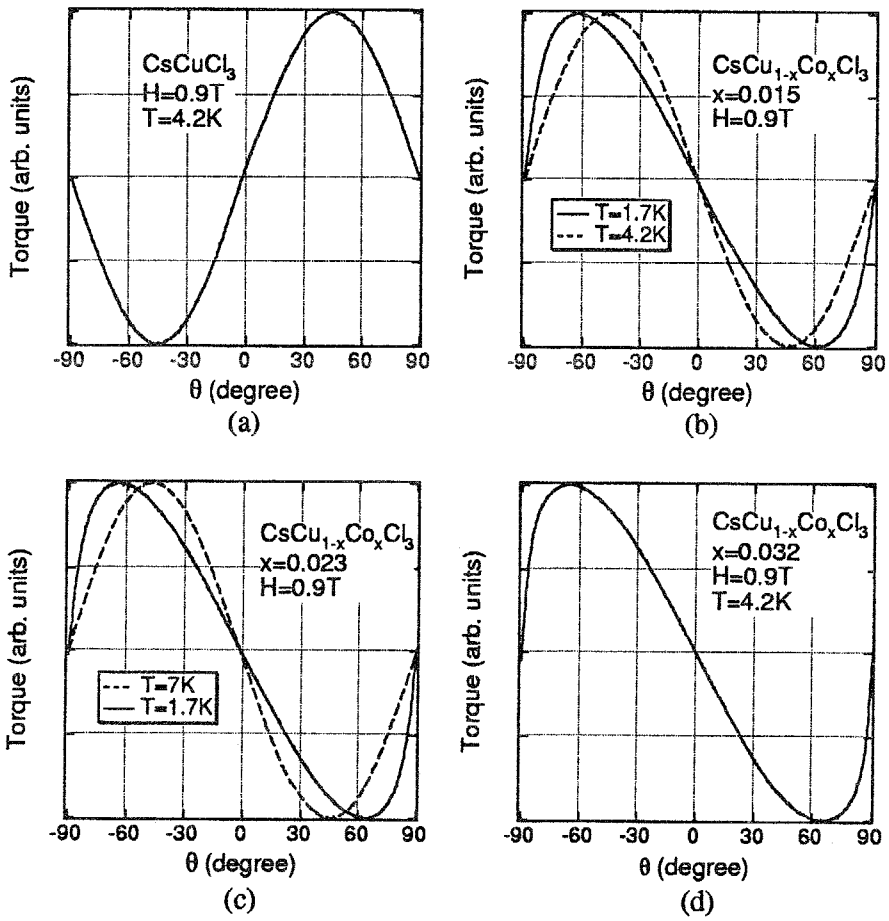

Figure 3.14: Torque curves for (a) $CsCuCl_3$ and $CsCu_{1-x}Co_xCl_3$ with (b) $x = 0015$, (c) 0.023 and (d) 0.032. The external field of 0.9 T is rotated in the ac-plane. In (b) and (c), solid and dashed lines denote the torque curves in phase II and I, respectively.

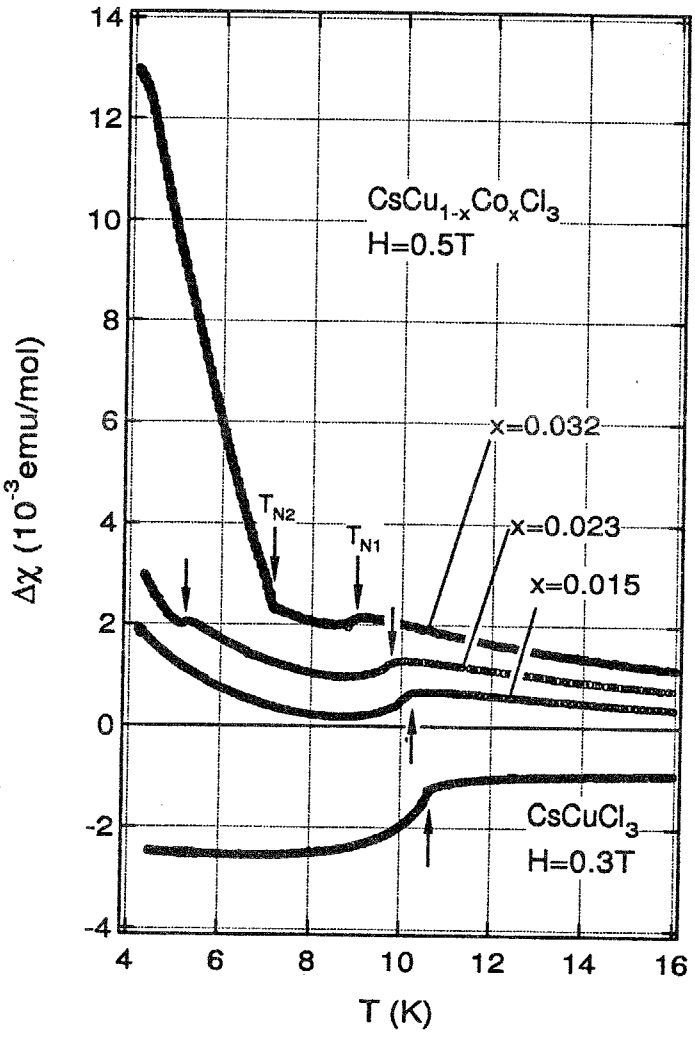

Figure 3.15: Temperature dependences of $\Delta\chi$ defined by eq. (3.5), for $CsCuCl_3$ and $CsCu_{1-x}Co_xCl_3$ with $x = 0.015$, 0.023 and 0.032 in the phase transition region. Transition points are indicated by arrows.

3.3.4 High field magnetization process

Figure 3.16 shows the magnetization processes using the pulsed high magnetic field parallel and perpendicular to the c-axis. Measurements were performed at $T = 1.5\,\mathrm{K}$. The anomaly

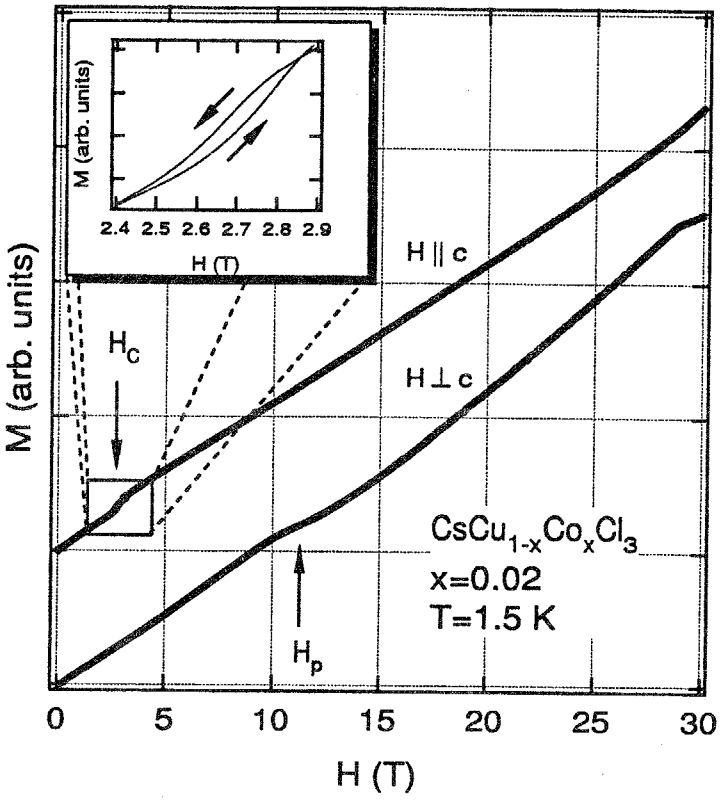

Figure 3.16: High field magnetization for $H \perp c$ and $H \parallel c$ for the sample with $x = 0.02$. Transition field is indicated by an arrow. An enlarged figure around the transition field is shown in a inset. The arrows in the inset indicates the increasing and decreasing processes.

which appears at $H(\perp c) \sim 28\,\mathrm{T}$ is supposed to come from the slipping of the sample due to the insufficiency of fixing the sample. Magnetization curve for $H \perp c$ shows quite a similar behavior to that of pure $CsCuCl_3$, i.e., the magnetization plateau which is not so sharp appears at $H \sim 12\,\mathrm{T}$. For the magnetization curve for $H \parallel c$, there is no anomaly except that is indicated as H_c by an arrow. The quantum phase transition around the critical field $H_c = 12.5\,\mathrm{T}$, which was observed for pure $CsCuCl_3$, disappears with doping of a small amount of Co^{2+} ions. The inset shows the precise magnetization behavior for $H \parallel c$ around the phase transition region. One can observe the hysteresis around H_c. This fact suggests

that the field induced phase transition is of the first-order transition.

3.3.5 Summary of this section

In the triangular antiferromagnetic system $CsCu_{1-x}Co_xCl_3$ with $x \leq 0.032$, the magnetic anisotropy changes from planar type to axial and its magnitude increases, with increasing Co^{2+} concentration x. For the sample with $x = 0.005$, which seems to be closely isotropic, any field induced phase transition was observed below $H = 7$ T. It was found that for $0.015 \leq x \leq 0.032$, a new ordered phase (II) appears in the low-temperature and low-field region of an ordered phase (I) (see the schematic phase diagram in Fig. 3.13). With increasing Co^{2+} concentration x, the area of the new phase becomes enlarged in the phase diagram. The transition field at which the new phase becomes unstable is minimum for $H \parallel c$ and maximum for $H \perp c$. The new phase has weak spontaneous magnetization along the c-direction. The spin structure of the new phase is unknown.

Before the present measurements, our first speculation is that the umbrella-like spin structure as shown in Fig. 3.4 (a) is realized in the ground state, when Co^{2+} ions are doped to reduce the planar anisotropy. The experimental results of the magnetization and the torque measurements, however, indicate that the spin structure of phase II is stabilized with the help of the axial anisotropy. With decreasing Co^{2+} concentration x, the area of phase II is reduced and then disappears. Thus it is logical to deduce that phase I which surrounds phase II is essentially identical to the ordered phase of $CsCuCl_3$. Since the amount of Co^{2+} ion is small, we assume that the exchange interaction in the chain and between the chains are not largely modified. Since the intrachain interaction is ferromagnetic, the spin-flop transition cannot be expected. If the coplanar structure shown in Fig. 3.4 (b) is realized in phase II, the transition at H_c for $H \parallel c$ is not understandable, because both the anisotropy and the quantum fluctuation in high fields favor the coplanar structure over the umbrella type one [79, 90]. Within these measurements the spin structure in the phase II could not be determined.

3.4 Neutron scattering from $CsCu_{1-x}Co_xCl_3$ with $x = 0.03$

In order to clarify the spin structures of the phase I (intermediate phase) and phase II (low-temperature phase), elastic neutron scattering experiments have been carried out for the sample with $x = 0.03$. Experimental procedures and the results are described in following sections.

3.4.1 Equipment

Measurements were performed at E1 triple axis spectrometer installed at experimental hall of Berlin Neutron Scattering Center Hahn-Meitner-institute (Berlin) with the two axis mode. The incident neutron energy was fixed at $E_i = 13.9$ meV by Bragg reflection of the pyrolytic graphite monochromator, and the horizontal collimation sequence was chosen as 40'-40'-40'-open. Single crystal of $CsCu_{1-x}Co_xCl_3$ with $x \sim 0.03$ was used. The sample has the shape of triangular prism 5 mm in width and 15 mm in length. The sample was mounted in the cryostat with its [110] and [001] axis in the scattering plane.

In order to obtain the external magnetic field, we used high field superconducting magnet which with the maximum field of 14.5 T for $H \perp c$ and of 4 T for $H \parallel c$.

3.4.2 Results

In order to determine the magnetic structure, the scans parallel along c^*-axis were performed. Figure 3.17 indicates $(hh\zeta)$ reciprocal-lattice plane, where the dashed lines with double arrow indicates the scans around magnetic Bragg points performed in the present study. Here we have adopted the chemical unit of $CsCuCl_3$ structure as the unit along the c-axis. The scattering intensity is proportional to the square of the component of the spin which is perpendicular to the scattering vector. $\boldsymbol{q}_1$ vector makes an right angle with the c-axis, while the angle between the $\boldsymbol{q}_2$ vector and the c-axis is small (approximately 16°, see Fig. 3.17). Therefore, the c-axis component of the spin structure is emphasized around $\boldsymbol{q}_1$. On the other hand, the c-plane component of the spin structure is emphasized and the c-axis component is weakened around $\boldsymbol{q}_2$ scan.

Typical scans along $\boldsymbol{Q} = (1/3, 1/3, \zeta)$ around $\zeta = 0$ and 6 at $T = 1.6$ K are shown in Fig. 3.18 (a) and (b), respectively. As shown in Fig. 3.18 (a), in the low temperature phase, the scan profile around $\boldsymbol{Q} = (1/3, 1/3, 0)$ consists of the central peak at $\zeta = 0$ and the satellite peaks at $\zeta = \pm\delta \simeq 0.084$. The value of δ indicates the period of the helical structure along the c-axis. The period of the helical structure was found to be 71.4 Cu-sites, which is almost the same as that of $CsCuCl_3$. Since the pitch of the helical structure θ is determined by eqs.

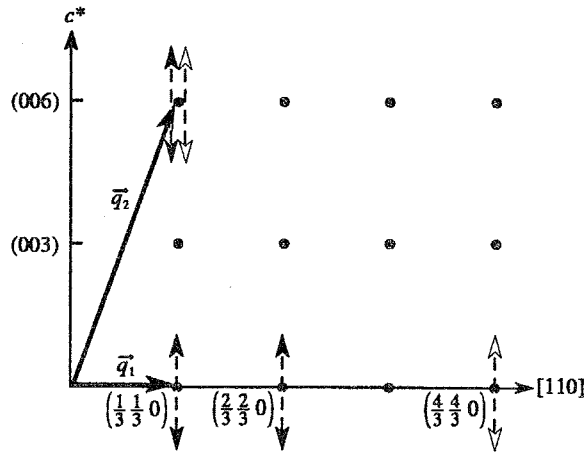

Figure 3.17: The reciprocal lattice space in the scattering plane. Parallel scans were performed around the magnetic Bragg points indicated by dashed lines. Black and white arrows indicate the scans which were adopted for $H \perp c$ and $H \parallel c$, respectively.

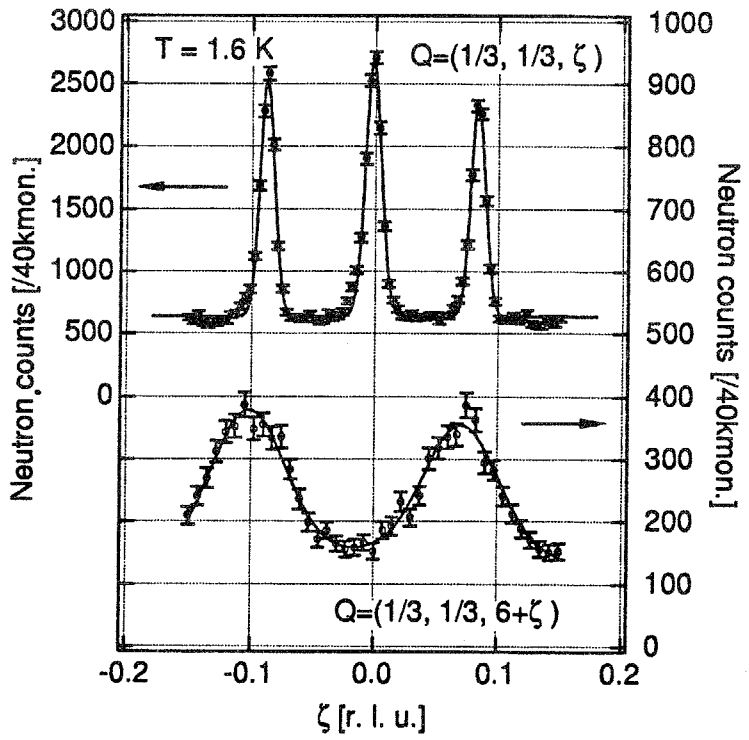

Figure 3.18: The scan profiles along $\boldsymbol{Q} = (1/3, 1/3, \zeta)$ around (a) $\zeta = 0$ and (b) $\zeta = 6$. Solid lines denotes the results of the Gaussian fitting.

(3.2), the magnitude of the intrachain interaction seems to be not so affected by doping such amount of Co^{2+} ion. On the contrary, the scan profile around $\boldsymbol{Q} = (1/3, 1/3, 6)$ does not show the obvious central peak around $\zeta = 6$ (see Fig. 3.18 (b)). Therefore, by comparing the peak intensities around $\zeta = 0$ and $\zeta = 6$, we see that the central peak originates from the c-axis components of the spins which make $\sqrt{3}\times\sqrt{3}$ enlarged magnetic unit cell in the c-plane as shown in Fig. 3.19 (a). On the other hand, the satellite peaks indicate the projecton to the c-plane of the ordering structure which stack helically along the c-axis, as shown in Fig. 3.19 (b). From the present results, it is found that the magnetic structure which satisfies all

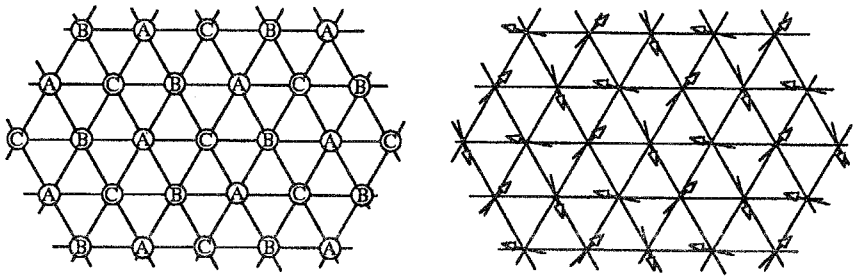

Figure 3.19: The spin components which cause (a) the central peak and (b) the satellite peaks. In (a), A, B and C denote the three distinct sublattices which have the different c-axis component of spin.

reflections observed in the low temperature phase, is an oblique triangular antiferromagnetic structure, in which the spin plane is tilted from the c-plane. Figure 3.20 illustrates the spin structure in the low-temperature phase. In order to take into account of the divergency from the 120°-structure, we introduce the angle γ which indicates the angle between the yc-plane and the sublattice moments $\boldsymbol{S}_2$ and $\boldsymbol{S}_3$, as shown in Fig. 3.20 (b). We infer that the all sublattice moments have the same magnitude, and are confined within the spin planes as illustrated in Fig. 3.20, since it is not expected that the large internal field which lifts a third of spin from the spin plane. When the spin strucutre realizes the arrangements illustrated as Fig. 3.20, and the spin planes stack helically along the c-axis, the integrated intensity of the magnetic Bragg scattering for $\boldsymbol{Q} = (h, h, \zeta)$ with $h = n/3$ and $\zeta = 0$ and even integer and satellite positions around these points (i.e. $\zeta \pm \delta$) is given by

$$I \propto |f(\boldsymbol{Q})|^2 \cos\left(\frac{\pi}{2} - \theta - \arccos\sqrt{\frac{a^2\zeta^2}{4c^2h^2 + a^2\zeta^2}}\right) |F(h, h, \zeta)|^2 \qquad (3.6)$$

and $I = 0$ for integer h, where θ is half of the scattering angle, $f(\boldsymbol{Q})$ is the magnetic form

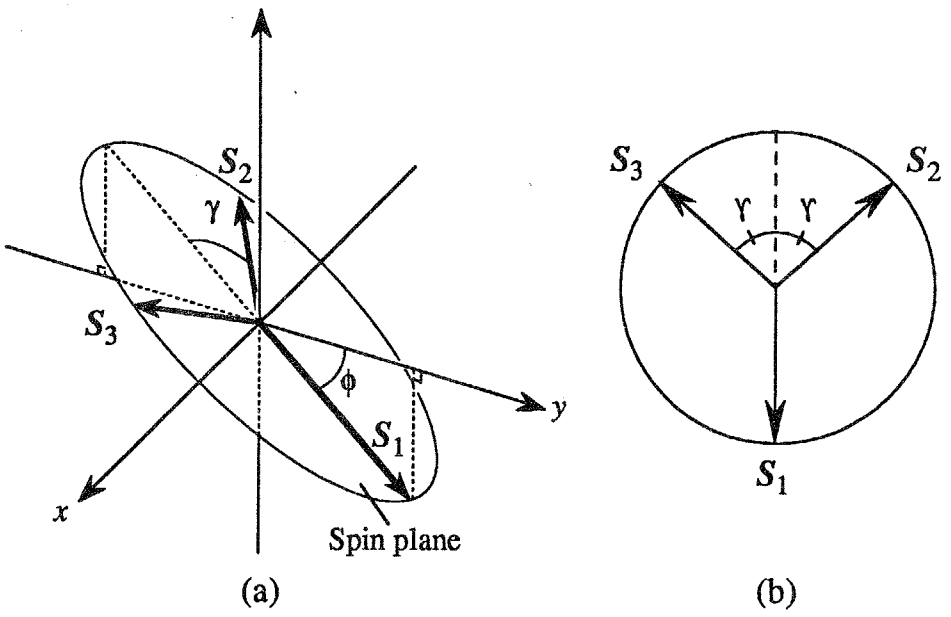

Figure 3.20: Oblique triangular antiferromagnetic structure in the low-temperature phase. (a) The angle ϕ indicates the angle between the spin plane and the c-plane. (b) The angle γ indicates the angle between the cy-plane and the sublattice moments $\boldsymbol{S}_2$ and $\boldsymbol{S}_3$.

factor and a and c are lattice constants. For $f(\boldsymbol{Q})$, we used the spherical magnetic form factors calculated by Watson and Freeman [94]. The lattice constants $a = 7.137\,\text{Å}$ and $c = 6.012\,\text{Å}$ are determined from the (110) and (006) nuclear reflections. $F(h,h,\zeta)$ is the magnetic structure factor. Due to the long-period helical spin structure along the c-axis, the c-plane component and the c-axis component of the spins give Bragg peaks at $\zeta = 0$ and $\zeta = \pm\delta$, respectively. The structure factors for the planar component F_{ab} and for the axial component F_c are described as

$$|F_{ab}(hh\zeta)|^2 = d^2_{(hh\zeta)} \left\{ 2\left(\frac{h}{a}\right)^2 + \left(\frac{\zeta}{c}\right)^2 \right\} \{(1+\cos\gamma)^2\cos^2\phi + 3\sin^2\gamma\} \tag{3.7}$$

$$|F_c(hh\zeta)|^2 = d^2_{(hh\zeta)} \left(\frac{2h}{a}\right)^2 (1+\cos^2\gamma)\sin^2\phi, \tag{3.8}$$

where $d_{(hh\zeta)}$ is the spacing of the (h,h,ζ) lattice plane. The integrated Bragg intensities are calculated for various angles of ϕ and γ. In Fig. 3.21 the variation of the reliability factor R given by

$$R = \sum_{h,h,\zeta} \left| I_{\text{calc}}(h,h,\zeta) - I_{\text{obs}}(h,h,\zeta) \right| \Big/ \sum_{h,h,\zeta} I_{\text{obs}}(h,h,\zeta).$$

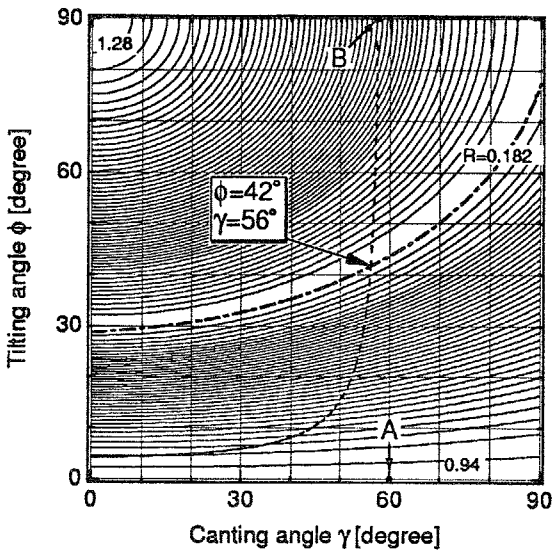

Figure 3.21: Contour plot of the reliability factor R as a function of the angle γ and ϕ. Dott dashed line indicates the minimized R-factor $R = 0.182$. Dashed line indicates the line which stisfies eq. 3.10.

is represented in contour. The R-factor is minimized when the angle (γ, ϕ) around the dott-dashed line plotted in Fig. 3.21.With decreasing tilting angle ϕ, canting angle ϕ which gives minimum R-factor rapidly decreases, and become zero when $\phi = 29.2°$. Since the magnetic structure could not be determined uniquely only from the ratio of the magnetic Bragg intensities, the magnitude of the spontaneous magnetization along the c-axis detected on magnetization measurements (see Fig. 3.3.2) would be expected to give the conclusive structure. For the oblique triangular structure, each sublattice magnetization is described by the next form,

$$\begin{aligned} \boldsymbol{S}_1 &= S(0, \cos\phi, \sin\phi) \\ \boldsymbol{S}_2 &= S(-\sin\gamma, -\cos\gamma\cos\phi, \cos\gamma\sin\phi) \\ \boldsymbol{S}_3 &= S(-\sin\gamma, \cos\gamma\cos\phi, \cos\gamma\sin\phi). \end{aligned} \tag{3.9}$$

So that the spontaneous magnetization M_{sp} parallel to the c-axis is described by

$$M_{\rm sp} = \frac{2S\cos\gamma - S}{3S}\sin\phi\,[\mu_{\rm B}/\text{magnetic ion}]. \tag{3.10}$$

In Fig. 3.21, dashed line gives $M_{\rm sp} = 0.025$ $[\mu_{\rm B}/\text{magnetic ion}]$. From the intersection of dashed and dot-dashed lines, the angle γ and ϕ are obtained as $(\gamma, \phi) = (56°, 42°)$.

(h, h, ζ)	I_{obs}	$I_{cal}\begin{pmatrix}\phi = 42^\circ \\ \gamma = 57^\circ\end{pmatrix}$	$I_{cal}(A)\begin{pmatrix}\phi = 0^\circ \\ \gamma = 60^\circ\end{pmatrix}$	$I_{cal}(B)\begin{pmatrix}\phi = 90^\circ \\ \gamma = 57.49^\circ\end{pmatrix}$
$(\frac{1}{3}, \frac{1}{3}, -\delta)$	0.324	0.306	0.497	0.155
$(\frac{1}{3}, \frac{1}{3}, 0)$	0.384	0.384	0	0.689
$(\frac{1}{3}, \frac{1}{3}, \delta)$	0.292	0.310	0.503	0.156
$(\frac{1}{3}, \frac{1}{3}, 6-\delta)$	0.210	0.230	0.373	0.116
$(\frac{1}{3}, \frac{1}{3}, 6)$	0.012	0.011	0	0.016
$(\frac{1}{3}, \frac{1}{3}, 6+\delta)$	0.186	0.226	0.366	0.114
$(\frac{2}{3}, \frac{2}{3}, -\delta)$	0.171	0.266	0.432	0135
$(\frac{2}{3}, \frac{2}{3}, 0)$	0.252	0.330	0	0.573
$(\frac{2}{3}, \frac{2}{3}, +\delta)$	0.172	0.266	0.432	0.134
		$R = 0.182$	$R = 0.947$	$R = 0.598$
M_{sp} [μ_B/ion]	0.025	0.025	0	0.025

Table 3.1: Experimental and calculated intensities of several magnetic Bragg reflections in $CsCu_{1-x}Co_xCl_3$ with $x = 0.03$ at $T = 1.6$ K. They are normalized to the total peak intensities around $\boldsymbol{Q} = (1/3, 1/3, 0)$ reflection. The calculated intensities at A- and B-point in Fig. 3.21 are also shown for comparison.

In Table 3.1, we show the experimental and calculated intensities of the Bragg peaks around $\boldsymbol{Q} = (1/3, 1/3, 0)$, (1/3, 1/3, 6) and (2/3, 2/3, 0) together with the calculated intensities for $\phi = 0°$ and 90° with $\gamma = 60°$. Experimental and calculated intensities are normalized to total intensities of central and satellite peaks around (1/3, 1/3, 0). The spin structure of $CsCuCl_3$ correspond to $I_{calc}(\phi = 90°)$. We see from Table 3.1 that the spins form the triangular structure neither in the c-plane, nor in the plane including the c-axis, but in the plane tilted from the c-axis with the angle $\phi = 42°$, $\gamma = 56°$. The difference between the observed and calculated value of the scattering intensities may come from the fact that the adopted variable parameter is only ϕ and γ, tilting angle of the spin plane and canting angle from the yc-plane, and we did not taking into account of the variation of the magnitude of S for each sublattice and infer all spins on the three sublattices are confined within the spin plane.

The scan profiles around (1/3, 1/3, 0) for the various temperature at zero field are shown in Fig. 3.22. With increasing temperature, the Bragg intensity of the central peak decreases and vanishes at T_{N2}. On the other hand, the satellite peaks persist up to T_{N1}.

Figure 3.23 shows the temperature variation of the peak intensities at $\boldsymbol{Q} = (1/3, 1/3, 0)$ and (1/3, 1/3, 0.084). With increasing temperature, the intensity of the central peak is

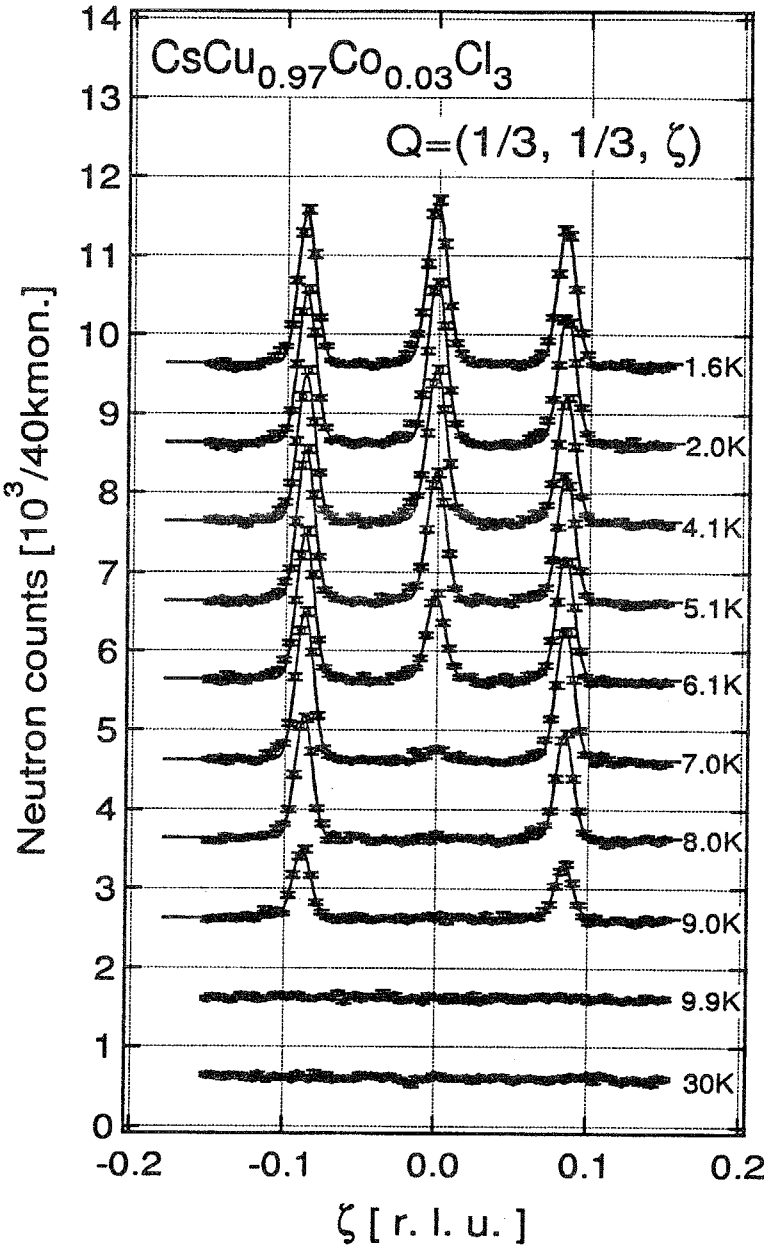

Figure 3.22: The scans around $\boldsymbol{Q} = (1/3, 1/3, \zeta)$ at zero field in the vicinity of $\zeta = 0$ for the various temperature.

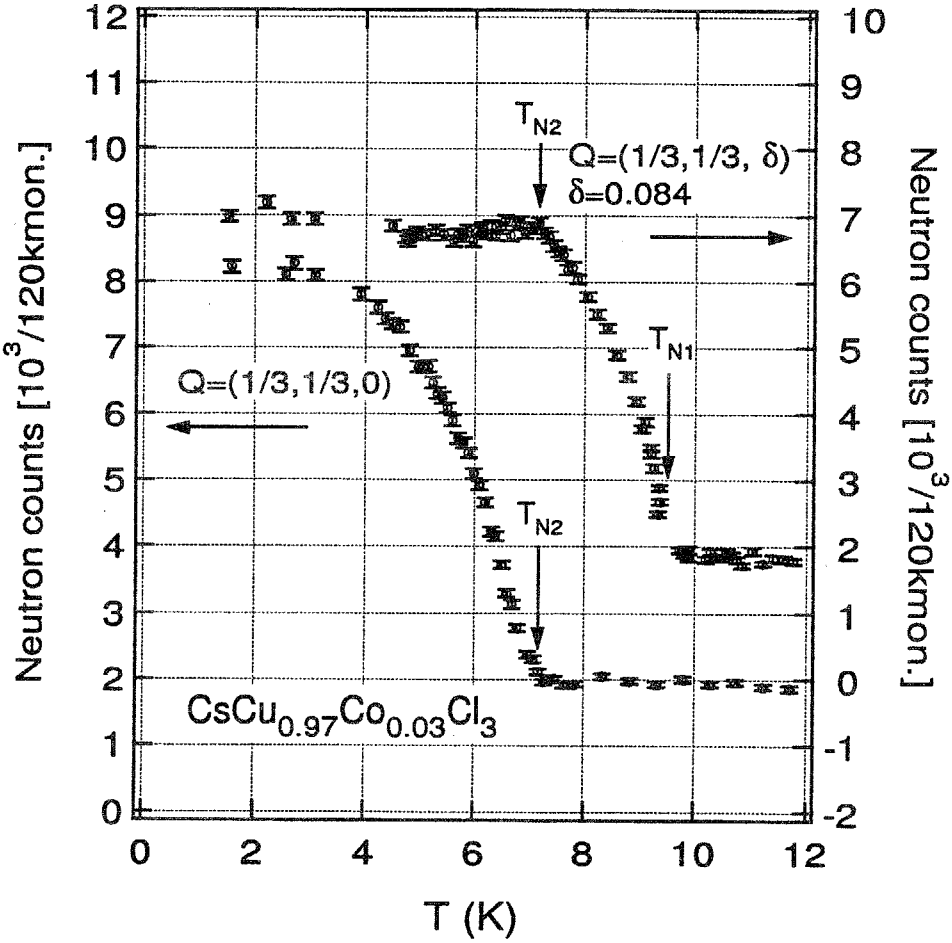

Figure 3.23: Temperature variations of Bragg scattering intensities for $\boldsymbol{Q} = (1/3, 1/3, 0)$ (left axis) and $(1/3, 1/3, \delta)$ with $\delta = 0.084$ (right axis) at zero field. Néel temperatures are indicate by arrows.

decreased and disappears at T_{N2} =7.2 K. On the other hand, the intensity of the satellite peak is almost constant up to T_{N2}, and decreases rapidly and vanishes at $T_{N1} = 9.6$ K. This fact show that the intensities of the central peak and satellite peaks are correlated with each other, and thus they come from the same source. The tilting angle ϕ of the spin plane increases from $\phi_0 \sim 46°$ at $T = 1.6$ K with increasing temperature, and $\phi = \pi/2$ at T_{N2}.

Figure 3.24 shows the scans along $\boldsymbol{Q} = (1/3, 1/3, \zeta)$ around $\zeta = 0$ of $T = 2$ K at various magnetic field applied perpendicular to the c-axis. With increasing applied field, the position of the satellite peaks shift slightly toward the center. This behavior is similar to that in pure $CsCuCl_3$ [86], which is shown in Fig. 3.6. On the other hand, the central peak exhibits more significant field dependence, i. e., the intensity of the central peak decreases and disappears at $H_c = 7.4$ T as shown in Fig. 3.25. The phase transition looks second order. The present results show that the field induced phase transition occurs at $H_c = 7.4$ T for $H \perp c$ and that the spin structure for $H > H_c$ is the same as that of $CsCuCl_3$.

For $H \parallel c$, we have measured the intensity around Bragg point $\boldsymbol{Q} = (4/3, 4/3, 0)$, since the major Bragg point $\boldsymbol{Q} = (1/3, 1/3, 0)$ is hidden by the dark angle of the horizontal cryomagnet. Figure 3.26 shows the scans around $(4/3, 4/3, \zeta)$ in the vicinity of $\zeta = 0$ at $T = 1.8$ K for the various magnetic field parallel to the c-axis. Due to the large scattering angle, Bragg peak intensity is weak and broad in comparison with the Bragg peaks around $\boldsymbol{Q} = (1/3, 1/3, 0)$. Although the signals are weak, the central peak and satellite peaks are obviously detected around $\boldsymbol{Q} = (4/3, 4/3, 0)$. For 1 T$< H <$ 4 T, the deviations of the central peak from $\zeta = 0$ are seen, which may be caused by the miss alignment of the crystal. It can be understood from the field variation that the spin structure changes between 3 T and 4 T.

Figure 3.27 shows field dependence of the central peak intensity at $T = 1.8$ K for $H \parallel c$. In Fig. 3.27, the open and the closed circles indicate the data collected for increasing and decreasing fields, respectively. With increasing field, the scattering intensity of $\boldsymbol{Q} = (4/3, 4/3, 0)$ is almost constant up to $H \sim 3$ T, and begins to decrease with a sharp bend. We see that the phase transition occurs at $H_c = 3.4$ T. Additional character of this behavior is that the scattering intensity of the low field phase has the hysteresis. These facts indicates that the field induced phase transition for $H \parallel c$ is of the first order.

As mentioned in the last of the previous section, the magnetization curve has small hysteresis around the phase transition field for $H \parallel c$. In the recent ^{133}Cs NMR study performed by Hirano *et al.* [95], it is observed the coexistence of the low field spin structure and the high field 120°-spin structure in the vicinity of the critical field. Their results seems to be consistent with ours.

The field induced phase transition from phase II to phase I is of second order for $H \perp c$

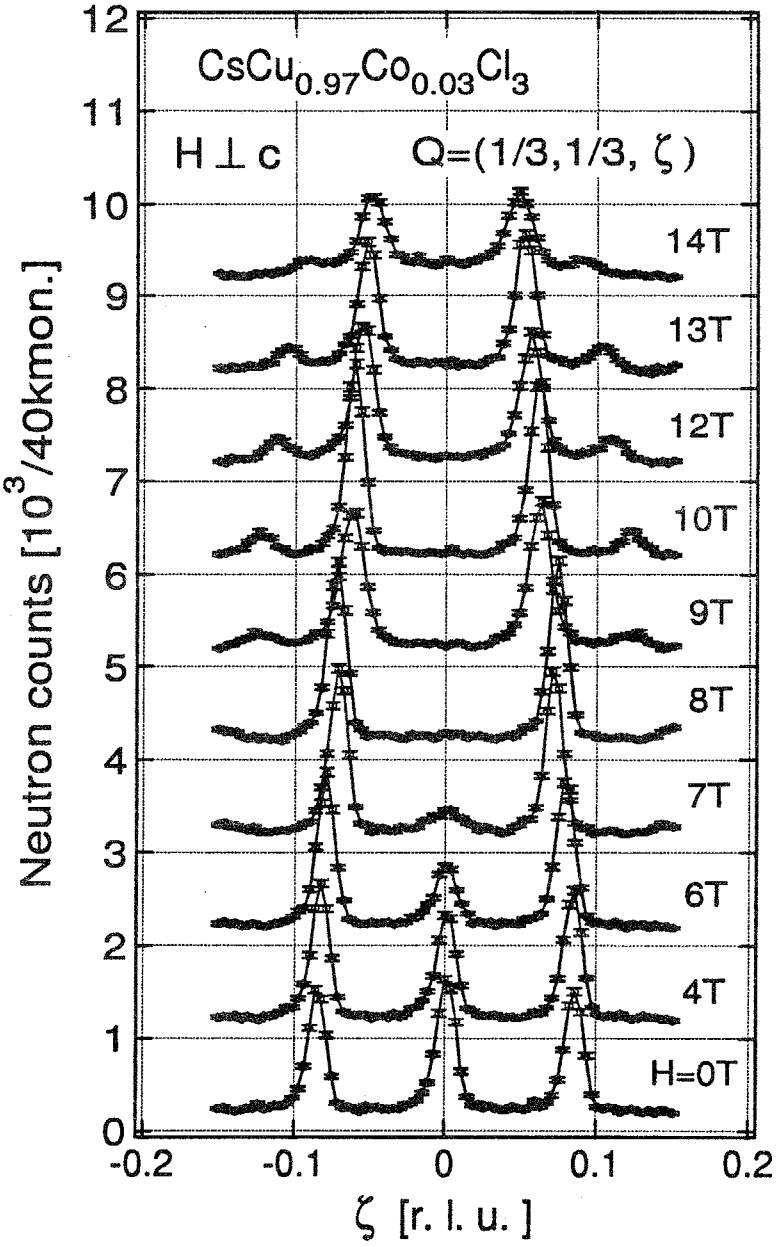

Figure 3.24: The scans along $\boldsymbol{Q} = (1/3, 1/3, \zeta)$ in the vicinity of $\zeta = 0$ at various magnetic field applied perpendicular to the c-axis. The measurements were performed at $T = 2\,\mathrm{K}$.

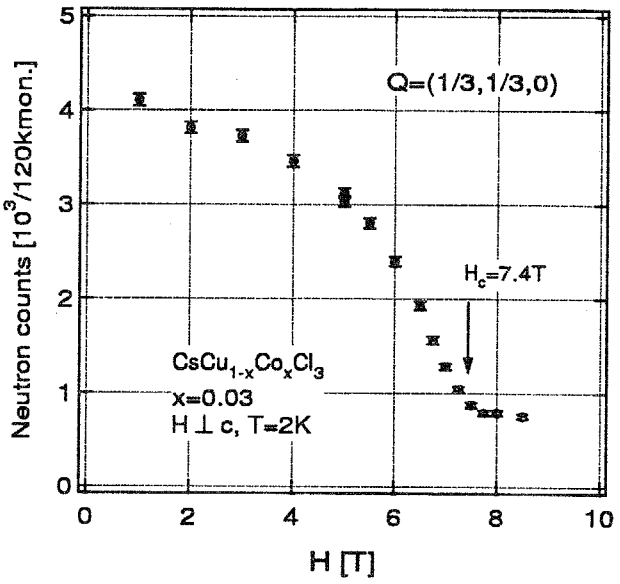

Figure 3.25: The field variation of the Bragg peak intensity at $Q = (1/3, 1/3, 0)$. The measurements were performed at $T = 2\,\mathrm{K}$ and the external field was applied perpendicular to the c-axis. Transition field is indicated by an arrow.

and of first order for $H \parallel c$.

3.4.3 Discussions

At present, the mechanism of the phase transition from phase I to phase II which occurs irrespective of the field direction is still unclear. Phase transitions in the random spin systems with competing anisotropies have been investigated in $Fe_{1-x}Co_xCl_2$ [96, 97] and $Fe_{1-x}Co_xCl_2{\cdot}2H_2O$ [98] by measuring of neutron scattering. Both systems undergo two phase transitions, which are characterized by the orderings of two spin components. In $Fe_{1-x}Co_xCl_2$, the ordering of one spin component is drastically altered by the ordering of the other component, and the lower-temperature transition is rather smeared, which Wong *et al.* [96, 97] attributed to random off-diagonal interactions. On the other hand, in $Fe_{1-x}Co_xCl_2{\cdot}2H_2O$, two phase transitions are equally sharp, and two components of the order parameters are decoupled. On the present system $CsCu_{1-x}Co_xCl_3$ with $x = 0.03$ the ordering nature is different from above both cases. In the present system, the basal plane components of spins orders first to form the 120°-structure at T_{N1}, and then the c-axis component orders at T_{N2}, so that the oblique triangular spin structure is realized. However, below

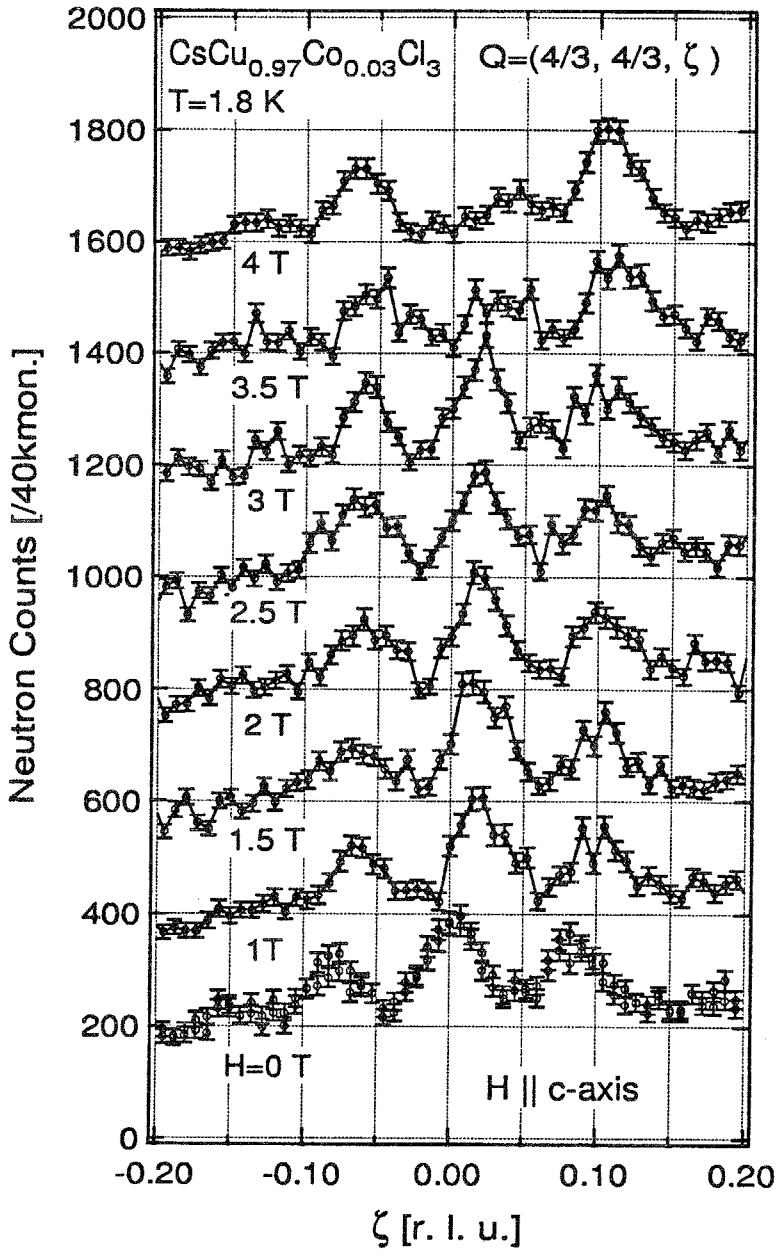

Figure 3.26: The scans around $\boldsymbol{Q} = (4/3, 4/3, \zeta)$ in the vicinity of $\zeta = 0$ at various magnetic field applied parallel to the c-axis. The measurements were performed at $T = 1.8\,\mathrm{K}$.

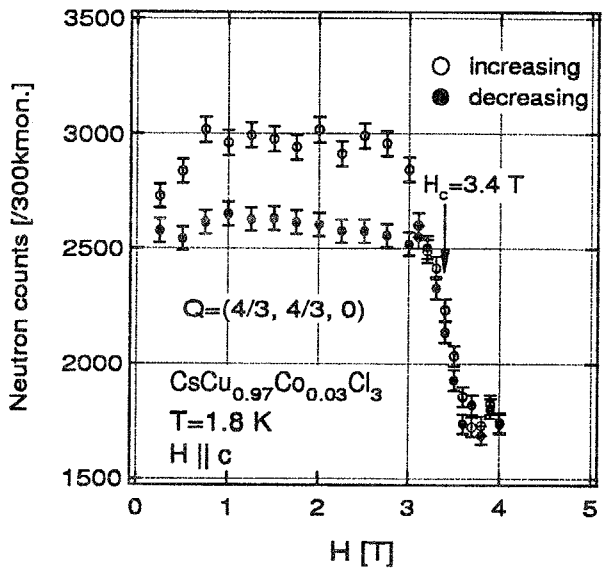

Figure 3.27: The field variation of the Bragg peak intensity at $\boldsymbol{Q} = (4/3, 4/3, 0)$. The measurements were performed at $T = 1.8\,\mathrm{K}$ and the external field was applied parallel to the c-axis. The open circles and closed circles denote the field increasing and decreasing process, respectively. Transition field is indicated by an arrow.

T_{N2}, both the components are not decoupled, *i.e.*, the growth of the basal plane component below T_{N2} is suppressed due to the growth of the c-axis component. Both phase transitions are fairly sharp.

$CsCuCl_3$ has the weak planar anisotropy, while $CsCoCl_3$ is an Ising spin system [13]. The phase transitions in mixed systems of TAF's with axial and planar anisotropies have been investigated in $Rb_{1-x}K_xNiCl_3$ [99] and $CsMn(Br_xI_{1-x})_3$ [100, 101]. However, neither new mixed ordered phase nor oblique phase was observed in these systems. Therefore, one can find that the oblique phase in the present system does not arise from competing anisotropies. The details of the exchange interaction between Cu^{2+} with spin-$\frac{1}{2}$ and Co^{2+} with fictitious spin-$\frac{1}{2}$ are still unclear. However, it can be suggested that the isotropic part of the interaction does not differ much from that between Cu^{2+} ions, because the helical pitch δ determined from the ratio of D-M and intrachain coupling constants is almost the same as that in $CsCuCl_3$ (see eqs. (3.2)).

The exchange interaction between Co^{2+} and other transition metal ions can have large off-diagonal term. For example, in $(CH_3)_3NHCo_{1-x}Mn_xCl_3{\cdot}2H_2O$ [102, 103], the off-diagonal term is dominant, and the diagonal term is canceled out. The off-diagonal exchange term has been proposed to interpret the nature of the mixed ordered state in $Fe_{1-x}Co_xCl_3$ [96, 97, 104]. Recently, Pleimling [105] argued the necessity of the off-diagonal term to describe the ordering of the perpendicular spin component in Ising-like system $FeBr_2$. In the present system, the off-diagonal term of the form

$$\mathcal{H}_{od} = J_{ij}^{zx}(S_i^z S_j^x + S_i^x S_j^z) + J_{ij}^{zy}(S_i^z S_j^y + S_i^y S_j^z) \tag{3.11}$$

is allowed between Cu^{2+} and Co^{2+}, where we take the z-axis parallel to the c-axis and x- and y-axes in the basal plane. It should be noted that the off-diagonal term can exist even in pure $CsCuCl_3$, because the local symmetry is lower than trigonal one, as mentioned in the beginning of this chapter. If $\mathcal{H}_{od}$ is of the same order in magnitude as J_0 or J_1, a few percent of the Co^{2+} doping produce the effective off-diagonal anisotropy which can overcome on average the planar anisotropy of the order $10^{-2}J_0$ [73], so that the spin-plane can tilt from the basal plane. We suggest that the off-diagonal exchange interaction between Cu^{2+} and Co^{2+} gives rise to the oblique phase in the present system. However, the microscopic mechanism leading the successive phase transitions is an open question.

3.4.4 Summary of this section

We have performed the elastic neutron scattering experiments for $CsCu_{1-x}Co_xCl_3$ with $x = 0.03$ in the magnetic field perpendicular and parallel to the c-axis. In the low-temperature

phase (phase I), the oblique triangular antiferromagnetic structure as shown in Fig. 3.20 is realized. At zero field, the phase transition to the intermediate temperature phase (phase II) which is the same as ordered phase of pure $CsCuCl_3$. When the magnetic field is applied parallel and perpendicular to the c-axis, the phase transition from the low-temperature structure to the phase I occurs at $H_c^{\parallel} = 3.7\,\mathrm{T}$ and $H_c^{\perp} = 7.4\,\mathrm{T}$, respectively. From the field variation of the intensities for $\boldsymbol{Q} = (1/3, 1/3, 0)$ and (4/3, 4/3, 0) reflections, the phase transition is revealed to be of second-order for $H \perp c$, and of first order for $H \parallel c$.

Chapter 4

New ordered phase in $RbFeCl_3$

Most of hexagonal ABX_3 TAF have triangular lattice planes stacked antiferromagnetically along the c-axis. On the other hand, there are several menbers which have ferromagnetic interaction between the neighboring triagular lattice planes. In addition to $CsCuCl_3$, $RbFeCl_3$, $CsFeCl_3$ and $CsNiF_3$ belong to the group. As reviewed in the previous section, $CsCuCl_3$ undergoes magnetic phase transition triggered by the quantum fluctuation in the magnetic field. $RbFeCl_3$ is also known to have the commensurate ordered phase which cannot be interpreted within the framework of the mean-field theory in the field perpendicular to the c-axis [112]. Thus, it is expected that the ordering process of $RbFeCl_3$ involves the same physics as observed in $CsCuCl_3$. In this chapter, the results of the magnetic measurements on $RbFeCl_3$ are provided. We found a new ordered phase in the finite field region for magnetic field parallel to the a-axis.

4.1 $RbFeCl_3$

$RbFeCl_3$ have ferromagnetic interaction along the c-axis. When the intrachain interaction is ferromagnetic, the dipole-dipole (D-D) interaction is enhanced, thus it plays an important role in magnetic phase transitions [106, 107].

$RbFeCl_3$ has strong easy plane anisotropy of the form $D(S_i^z)^2$ due to the crystal field, so that the spins lie in the c-plane and form a 120°-structure in the ground state [108]. However, the specific heat measurements by Haseda *et al.* [109] revealed three phase transitions at zero field and in the field parallel to the c-axis, which is shown in Fig. 4.1. Their transition temperatures at zero field have been determined as $T_{N1} = 2.6$ K, $T_{N2} = 2.3$ K and $T_{N3} = 1.95$ K. Shiba [107] described the successive phase transition at zero field in terms of the conical point instability due to the D-D interaction. The D-D interaction stabilizes a collinear spin structure corresponding to the M point in the hexagonal reciprocal lattice space, while the

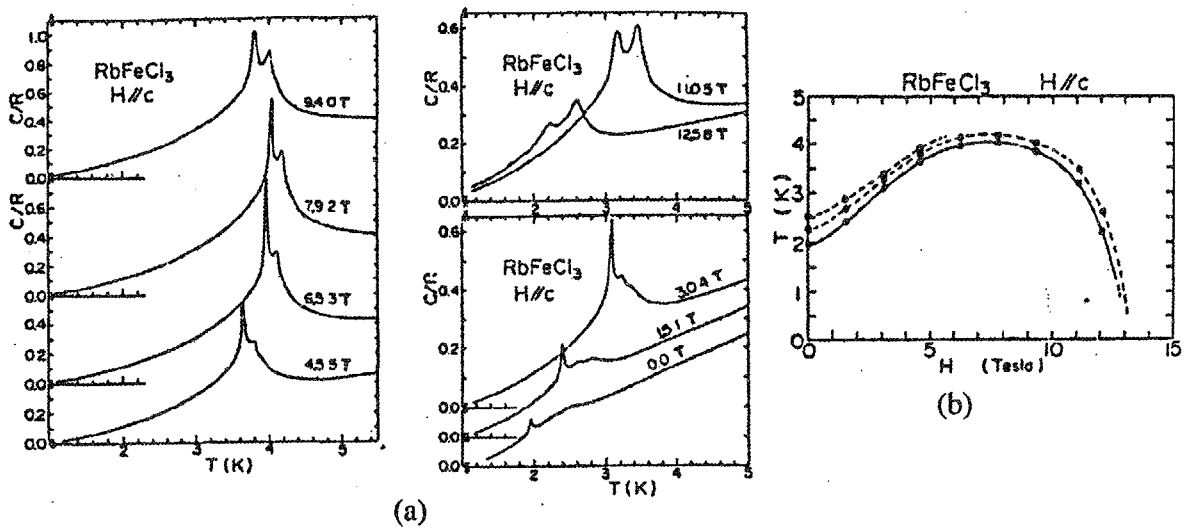

Figure 4.1: (a) specific heat and (b) resultant phase diagram of $RbFeCl_3$ in the field parallel the c-axis. (quoted from ref. [109].)

antiferromagnetic interchain interaction stabilizes the 120°-structure corresponding to the K point. Due to competition between both interactions, the incommensurate (IC) spin structure can be realized. Shiba [107] demonstrated that the successive phase transition occurs from the paramagnetic state to the ground state with the 120°-structure through two different IC states. The high-temperature IC phase (IC_1) is a simple sinusoidal IC phase in which the x-component of the spin is modulated with the incommensurate wave vector. The second IC phase (IC_2) is a double sinusoidal IC phase in which both the x- and y-components are modulated with different incommensurate wave vectors. The spin structures in these three phases were confirmed by Wada *et al.*[110] by the elastic neutron scattering experiments. Figure 4.2 shows the temperature dependence of the sattelite peak intensities. In Fig. 4.2, A_i and B_i are the reciprocal lattice points corresponding to the incommensurate structure for y- and x-components, respectively. With decreasing temperature, at first, the B_i-peak begins to increase at T_{N1}, and then the A_i-peak begins to increase at T_{N2}. Finally, both peaks are disappeared at T_{N3}, and the commensurate peak appears at K-point.

Shiba and Suzuki [111] proposed the phase diagram in magnetic fields parallel and perpendicular to the a-axis, as shown in Fig. 4.3. The IC_1 phase is stable in high magnetic fields, where a fan spin structure is stabilized due to the D-D interaction.

Wada *et al.*[110] also performed neutron elastic scattering experiments for $H \perp c$. Figure 4.4 summarises the field dependence of the A_i and B_i peak positions. Their experimental

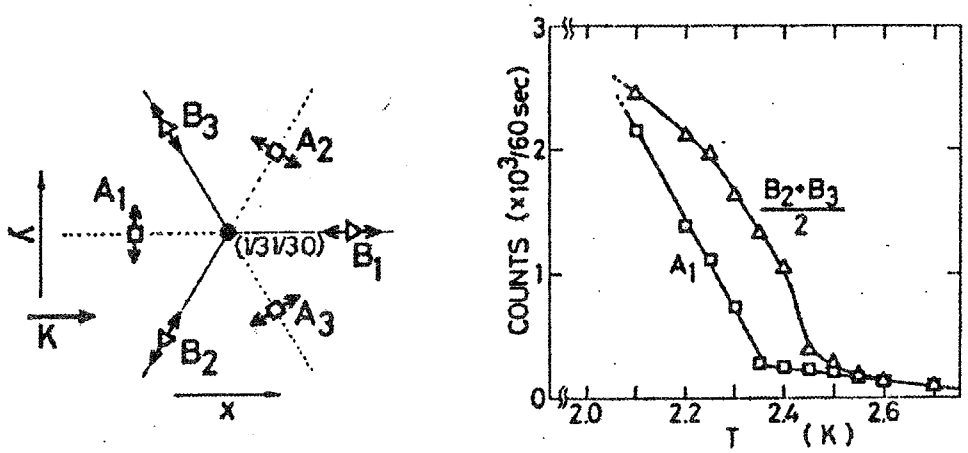

Figure 4.2: The temperature dependences of the scattering intensity of the A_1 peak and the mean value of the intensities at the B_2 and B_3 peaks, where A_1, B_2 and B_3 are the reciprocal lattice points which are shown in left figure. (quoted from ref. [110])

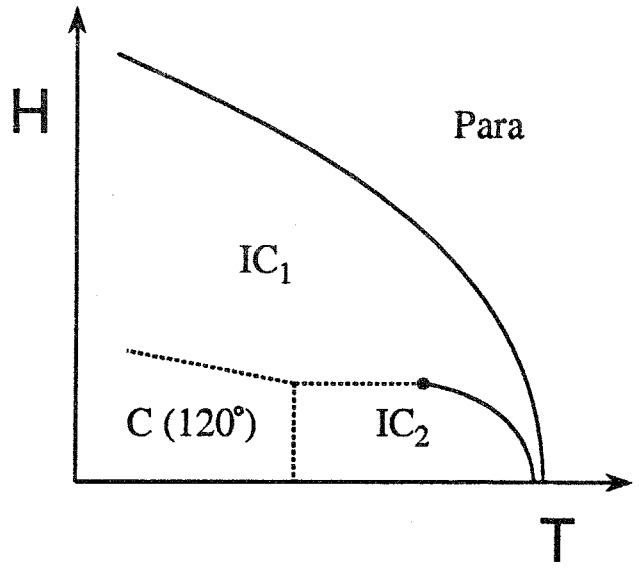

Figure 4.3: Schematic phase diagram of $RbFeCl_3$ for $H \perp c$ proposed by Shiba and Suzuki [111].

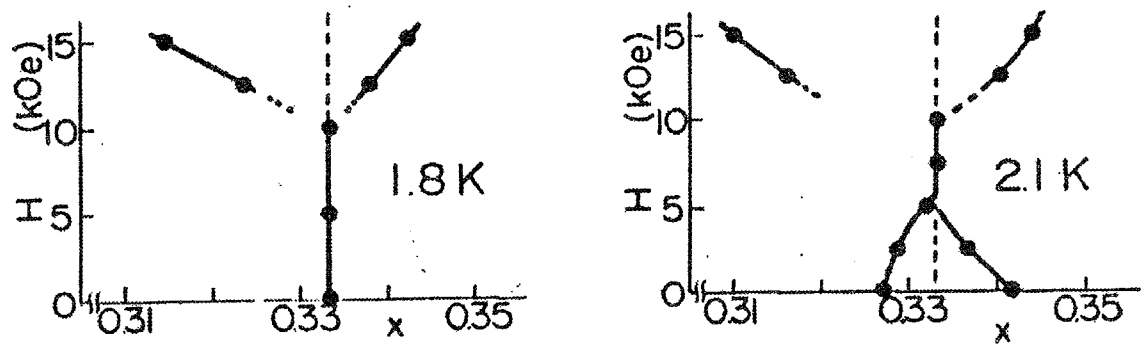

Figure 4.4: The field dependence of the incommensurate wave number in the field perpendicular to the c-axis. Measurements were performed at $T = 1.8$ K and 2.1 K which are in 120°-structure phase and IC_2 phase, respectively.

results are in qualitative agreement with the theory in the field region $H \leq 0.5$ T and 1 T$\leq H$. However, in the intermediate field region 0.5 T$< H < 1$ T, an unexpected commensurate phase was observed. On the basis of the results of specific heat and AC susceptibility measurements, Wada *et al.* [112] have determined the magnetic phase diagram for $H \perp c$. The resultant phase diagram is shown in Fig. 4.5. The new commensurate phase occupies wide temperature and field ranges in the phase diagram. A recent neutron scattering experiment by Kakurai [113] revealed that an up-up-down spin arrangement parallel to the external field perpendicular to the ac-plane is realized in the commensurate phase, i.e., two-thirds of the spins are parallel to the field direction and the rest of the spins are antiparallel. We label the commensurate phase as C_{uud} in this chapter.

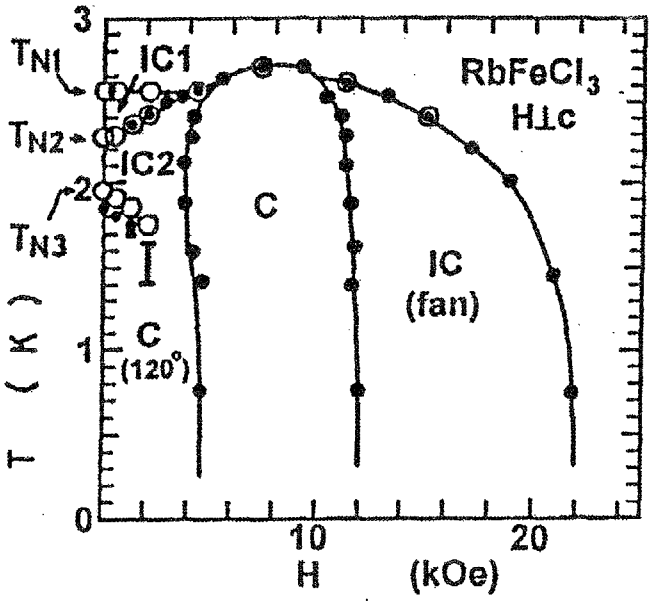

Figure 4.5: Magnetic phase diagram of $RbFeCl_3$ for $H \perp c$ obtained by Wada *et al.* Openand closed circles correspond to the anomalies oberved in the specific heat and AC susceptibility measurements, respectively. (quoted from ref. [112].)

4.2 Experiments

In order to investigate the phase diagram in $RbFeCl_3$, we carried out magnetic measurements for the applied field parallel to the a-axis.

Single crystals of $RbFeCl_3$ were grown by the vertical Bridgman method from the melt of equimolar mixtures of RbCl and $FeCl_2$ sealed in evacuated quartz tubes. The temperature at the center of the furnace was set at 650°C , and the lowering rate was 3 mm·h^{-1}. The source materials used were RbCl of 99.9% purity and $FeCl_2$ of 99.9% purity (Wako Pure Chemical Industries). After weighing, they were placed in a quartz tube and dehydrated by heating in vacuum at $\simeq$120°C for three days. Single crystals of 1$\sim$5 cm^3 were obtained. The crystals were easily cleaved along the (100) plane, and were cut into 10$\sim$20 mg samples for the present measurements. The magnetizations were measured between 1.8 and 3.0 K in magnetic fields up to 7 T using a superconducting quantum interference device (SQUID) magnetometer (Quantum Design MPMS XL). The magnetic fields were applied parallel to the a-axis.

Figure 4.6 shows the field dependence of the magnetization M and its field derivative dM/dH of $RbFeCl_3$ at $T = 1.8$ K. The magnetization curve does not exhibit any pronounced

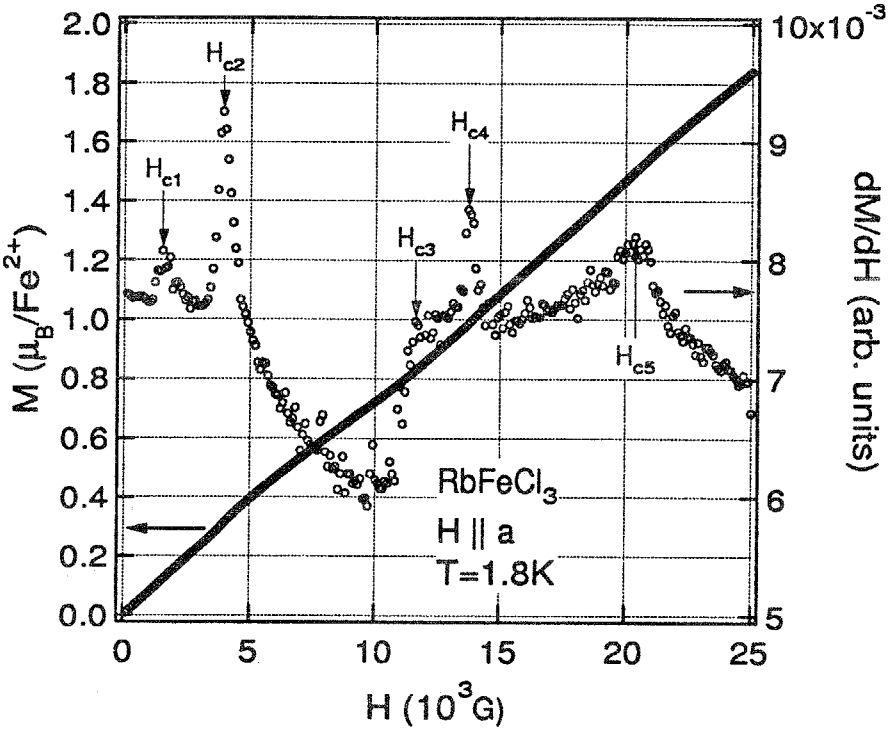

Figure 4.6: Magnetization curve and dM/dH of $RbFeCl_3$ at T=1.8 K for the external field parallel to the a-axis. Transition points are indicated by arrows.

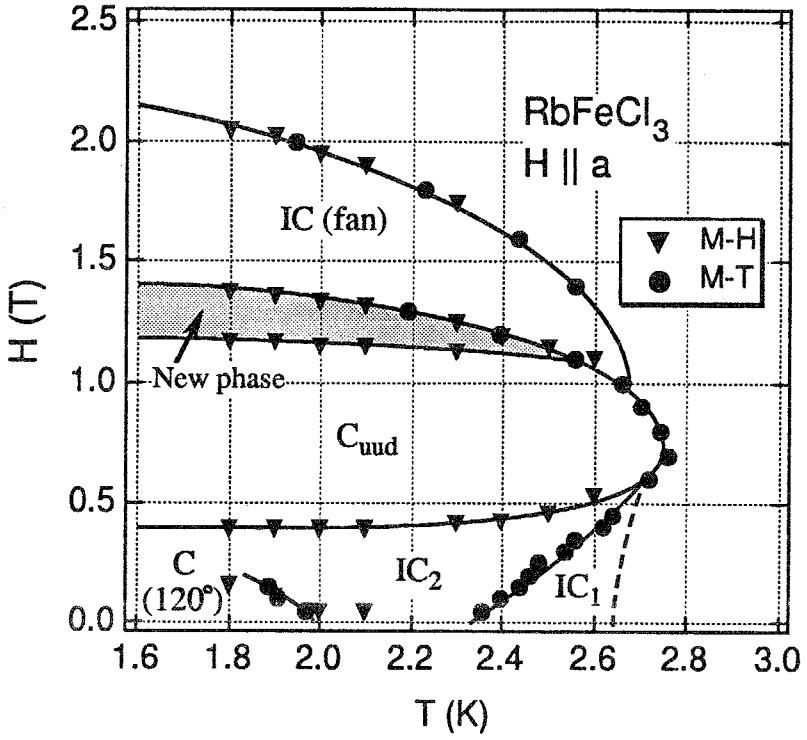

Figure 4.7: Magnetic phase diagram of $RbFeCl_3$ for $H||a$. Triangles and circles are the transition points determined from the magnetization curve and the temperature dependence of the magnetization, respectively. The hatched area between C_{uud} and IC (fan) is a new ordered phase found in the present work. The dashed phase boundary is determined by the specific heat measurements [112].

anomaly up to H =2.5 T. On the other hand, in dM/dH, we can see complicated structures, i.e., four sharp peaks and one shoulder. These anomalies are understood as indicating the phase transitions. We assigned the fields indicated by arrows to the transition fields. Except for the fourth transition field H_{c4}, all transition fields are in good agreement with those observed by Wada *et al.* [112]. The phase transition at H_{c4} is a new phase transition which was identified in the present work.

We measured the magnetization curve and dM/dH at various temperatures. The phase transition data are shown in Fig. 4.7 by closed triangles.

The transition field H_{c4} exhibits slight temperature dependence. We also measured the magnetization curve for $H\perp a$ at 1.8 K, and found that the magnetization curve and dM/dH are the same as those for $H||a$. From this finding, we may deduce that the phase transition is independent of the field direction, when the magnetic field is in the c-plane.

Figure 4.8 shows the temperature dependence of the susceptibility M/H of $RbFeCl_3$ measured at various external fields parallel to the a-axis. In the case of $H = 2.2$ T, there is no phase transition. The small anomaly at T =2.2 K is due to an instrument problem. With decreasing applied field, a broad peak appears from the low-temperature side. The temperature at which dM/dT gives the local maximum is assigned to the transition temperature. When H=0.8 T, the broad peak of magnetization disappears. In the field region (0.15 T< $H \leq$0.8 T), we assign the temperature with an inflection point in the susceptibility to the transition temperature. With decreasing magnetic field from 0.15 T, a new peak appears and shifts toward the high-temperature side. In this low field region ($H \leq 0.15$ T), two phase transitions are detected at temperatures indicated by arrows.

The phase transition temperatures obtained are plotted by closed circles in Fig. 4.7. In the phase diagram, the dotted line denotes the phase boundary between the paramagnetic phase and IC_1 phase observed by specific heat measurements [112]. However, we could not detect the boundary in the present measurement. In the commensurate C_{uud} phase of the intermediate field region, a collinear up-up-down spin structure is realized along the magnetic field [113]. The new phase observed in the present work is located between the C_{uud} phase and the IC (fan) phase.

4.3 Discussion

As previously mentioned, it is difficult to explain the existence of the C_{uud} phase and the new ordered phase within the framework of the classical spin model, even though competition between the dipole-dipole interaction and the exchange interaction is considered. In ferromagnetically stacked TAF, the quantum fluctuation plays an important role in magnetic fields, and sometimes stabilizes spin structures which are unstable in the classical calculation [79]. Such a field-induced quantum phase transition has first been observed in $CsCuCl_3$ [78]. Chubukov and Golosov [90] performed an analytical investigation of the quantum effects on the spin ordering in 2D TAFs in the magnetic field using the spin-wave approximation. They argued that the Heisenberg TAF can undergo the successive phase transition shown in Fig. 4.9 in magnetic fields due to the quantum fluctuation. The intermediate collinear spin structure is stabilized in a finite field range. Chubukov and Golosov predicted that the XY TAF also exhibits a similar successive phase transition. Since the collinear (b) structure in Fig. 4.9 is identical to the structure of the C_{uud} phase, we suggest that the new ordered phase is a commensurate phase with a coplanar structure, as shown in Fig. 4.9 (c).

The magnetization curve shown in Fig. 4.6 has finite slope in the C_{uud} phase. When the

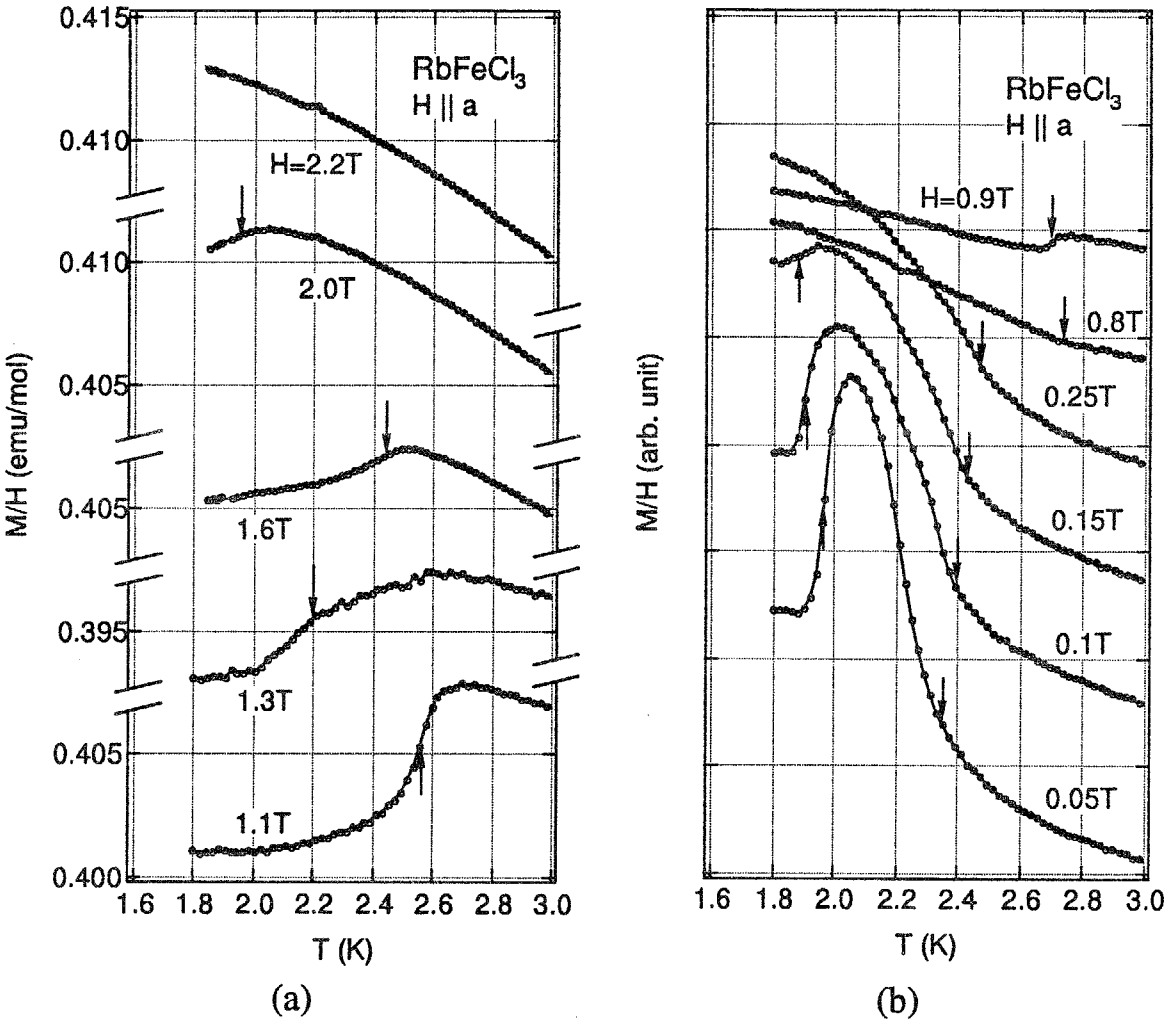

Figure 4.8: Temperature variations of the magnetic susceptibility of $RbFeCl_3$ at higher (a) and lower (b) field region. Transition points are indicated by arrows. For determining the transition points, see text.

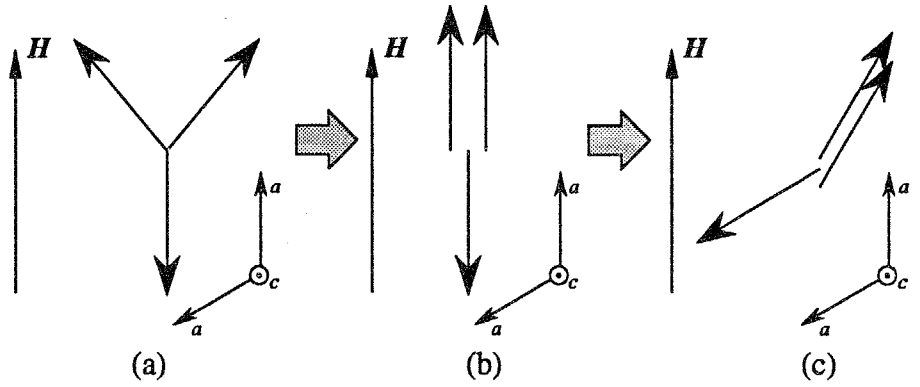

Figure 4.9: Spin structures predicted for the TAF in magnetic fields. With increasing magnetic field, the successive transition from the coplanar (a) structure to other coplanar (c) structure occurs through the collinear (b) structure.

spins are collinear along the external field, as shown in Fig. 4.9 (b), the magnetization curve has a plateau in the conventional spin system. In $RbFeCl_3$, however, the magnitudes of the sublattice magnetizations are determined by the balance between the large planar anisotropy of the single ion type, the exchange interactions and the external field, thus the magnetization can increase with increasing external field. $RbFeCl_3$ has large Van Vleck paramagnetic susceptibility of the order of 10^{-3} emu/mol. For these reasons, the magnetization curve of the present system does not have a plateau in the C_{uud} phase.

In high magnetic fields, there exists the incommensurate IC (fan) phase with a fan structure, which is predicted by the classical model. The D-D interaction may be responsible for the revival of the classical ordered state.

In conclusion, we have measured the magnetization of $RbFeCl_3$ for the applied field parallel to the a-axis and have determined the phase diagram, as shown in Fig. 3. A new ordered phase was observed in the intermediate field region. It was suggested that the spin structure of the new ordered phase is coplanar, as shown in Fig. 5(c), and is stabilized by the quantum fluctuation as well as the collinear structure in the C_{uud} phase.

4.4 Recent theoretical study

In order to clarify the field induced successive phase transition of $RbFeCl_3$, theoretical study have been performed by Shiba *et al.* [114]. They derived microscopically an expression for the free energy which describes the quantum and thermal fluctuations. They found that the following new terms

1. $-J_3[\boldsymbol{m}_1 \cdot \boldsymbol{m}_2(m_1^2 + m_2^2) + \boldsymbol{m}_2 \cdot \boldsymbol{m}_3(m_2^2 + m_3^2) + \boldsymbol{m}_3 \cdot \boldsymbol{m}_1(m_3^2 + m_1^2)]$
2. $-J_2[(\boldsymbol{m}_1 \cdot \boldsymbol{m}_2)^2 + (\boldsymbol{m}_2 \cdot \boldsymbol{m}_3)^2 + (\boldsymbol{m}_3 \cdot \boldsymbol{m}_1)^2]$

can lift the nontrivial degeneracy, where $\boldsymbol{m}_i$ denote the sublattice magnetizations. Figure 4.10 shows the calculating results of the magnetization process and dM/dH with $J_2 = 0.1$ K and $J_3 = 0.1$ K. The calculating results are in qualitative agreement with the experimental

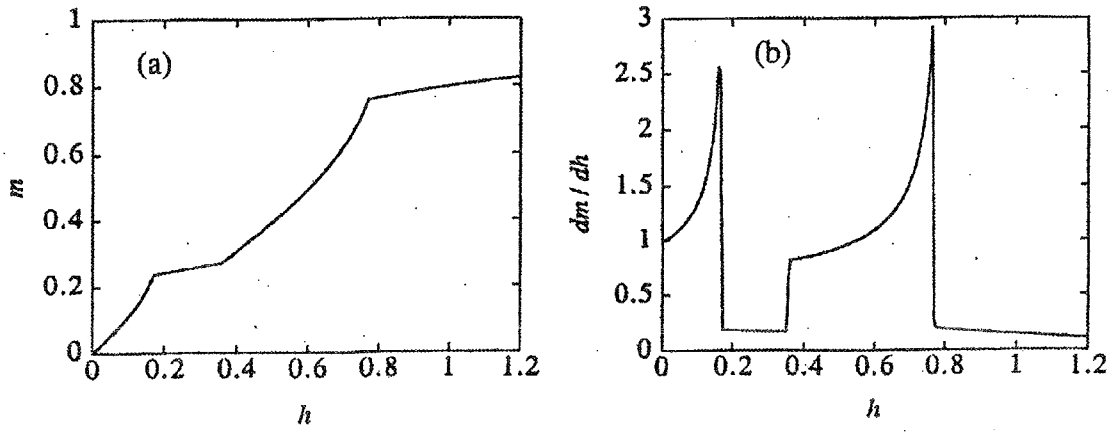

Figure 4.10: The theoretical magnetization curve and dM/dH taking account of the fourth-order terms of sublattice magnetization described in the text.

result shown in Fig. 4.6, except the anomalies at H_{c1} and at H_{c4} due to the D-D interaction. This result supports our speculation of the spin structure which is realised in the field region $H_{c3} \leq H \leq H_{c4}$ presented in the previous section.

Chapter 5

Summary and further scope

In the present studies, various types of phase transitions and their properties were presented for three triangular antiferromagnetic (TAF) systems. Though the manifold degeneracy due to the nearest neighbor bonding frustration is partially lifted by the small perturbation which originates from pseudo-dipolar or single-ion anisotropies, and quantum and thermal fluctuations, many spin states are still close energetically. The variety of the phase transitions presented reflects the multiplicity of the states.

In chapter 2, the various phase diagrams of the mixed TAF system $CsMn(Br_xI_{1-x})_3$ are presented. The variety of the phase diagrams come from the frustration and the competition between the weak anisotropy and applied field. The present study reveals the magnetic anisotropy can be systematically controlled by varying bromine concentration x. Although there are detailed speculations for the ESR frequency-field relation [16, 17, 115] and the dispersion relation of the magnetic excitations [40, 116, 117, 118, 119] for the TAF with various strength of anisotropies, the experimental confirmations for the predictions are not so many, because the anisotropy parameters of the real magnets are not appropriate for the experimental conditions or there is no suitable compounds. On the present system, the spin-flop field can be controlled by the bromine concentration x as H_{sf} [T]$= 5.04\sqrt{|x - x_c|/x_c}$ [T] for $x \leq 0.3$, so that systematical studies of ESR and magnetic excitations for various anisotropy TAF are possible. At $x_c = 0.19$, the system becomes isotropic limit. Thus, it is expected that the phase transition belongs to the chiral universarityclass. The critical exponent $\beta = 0.28 \pm 0.02$ for the sublattice magnetization obtained by neutron scattering experiment agrees well with the theoretical value $\beta = 0.30 \pm 0.02$

In chapter 3, the appearance of the new ordered phase and the spin structure in $CsCu_{1-x}Co_xCl_3$ are presented. It was found that the, oblique triangular structure phase occurs with small amount of Co^{2+} ion concentration $x \geq 0.015$, and its area on the temperature versus

field phase diagram is enlarged with increasing x for both field direction $H \parallel c$ and $\perp c$. To the best of author's knowledge, the present systemshows the first example of the oblique triangular antiferromagnetic phase. The origin of the oblique phase cannot be explained by the competition of the planar and axial anisotropy. We infer that the enhancement of the off-diagonal term of the nearest neighbor exchange interaction due to Co^{2+} doping is responsible for the oblique phase. The off-diagonal exchange field is also allowed for $CsCuCl_3$ because of its low crystal symmetry, though, its magnitude should be too small to overcome the planar anisotropy. The reason for the vanishing of the high field phase transition (see Fig. 3.16) which is observed in magnetization curve of $CsCuCl_3$ for $H \parallel c$ is not clear now. The high field spin structure have not been determined. There is a possibility that the doped Co^{2+} ions disturb the spin ordering of the high-field coplanar structure, so that the transition is smeared out. The research for the spin state in high-fields is desirable.

In chapter 4, a field induced new ordered phase of XY TAF system $RbFeCl_3$ is presented for the field parallel to the easy plane. According to the theoretical prediction [90], the successive field induced phase transition as shown in Fig. 4.9 is expected for the field parallel to the basal plane when the spins are confined within the XY-plane. The magnetization anomaly which was newly found in this study is the strong evidence of the appearance of the high-field coplanar structure shown in Fig. 4.9 (c). Recent theoretical study performed by Shiba *et al.* [114], which takes the quantum and thermal fluctuations into account, shows the qualitative agreements with the experimental result for the magnetization curve, except for the rounding of dM/dH at the beginning of the plateau (C_{uud} phase) region. It is not clear whether the rounding comes from finite temperature effect or other origin. The confirmation of the magnetic structure in the field range between $H_{c3} < H < H_{c4}$ is needed.

References

[1] J. Vannimenus and G. Toulouse: J. Phys. C: Solid State Phys. **10** (1977) L537.

[2] J. Villain: J. Phys. C: Solid State Phys. **10** (1977) 1717.

[3] T. Inami, Y. Ajiro and T. Goto: J. Phys. Soc. Jpn. **65** (1996) 2374.

[4] T. Tonegawa and I. Harada: J. Phys. Soc. Jpn. **56** (1987) 2153.

[5] K. Okunishi, Y. Hieida and Y. Akutsu: Phys. Rev. B **60** (1999) R6953.

[6] K. Kubo: Phys. Rev. B **48** (1993) 10552.

[7] K. Takano, K. Kubo and H. Sakamoto: J. Phys.: Condens. Matter **8** (1996) 6405.

[8] L. Onsager: Phys. Rev. **65** (1944) 117.

[9] G. H. Wannier: Phys. Rev. **79** (1950) 357.

[10] K. Wada and T. Ishikawa: J. Phys. Soc. Jpn. **52** (1983) 1774.

[11] T. Nikuni: Ph D thesis, Tokyo Institute of Technology (1996).

[12] H. Kawamura and S. Miyashita: J. Phys. Soc. Jpn. **54** (1985) 4530.

[13] M. F. Collins and O. A. Petrenco, Can. J. Phys. **75** (1997) 605 and references therein.

[14] D. Beckmann, J. Wosnitza, H. v. Löhneysen and D. Visser: Phys. Rev. Lett. **71** (1993) 2829.

[15] P. B. Johnson, J. A. Rayne and S. A. Friedberg: J. Appl. Phys. **50** (1979) 1853.

[16] H. Tanaka, S. Teraoka, E. Kakehashi, K. Iio and K. Nagata: J. Phys. Soc. Jpn. **57** (1988) 3979.

[17] H. Tanaka, Y. Kaahwa, T. Hasegawa, M. Igarashi, S. Teraoka, K. Iio and K. Nagata: J. Phys. Soc. Jpn. **58** (1989) 2930.

[18] M. L. Plumer, K. Hood and A. Caillé: Phys. Rev. Lett. **60** (1988) 45.

[19] M. L. Plumer and A. Caillé: Phys. Rev. B **41** (1990) 2543

[20] S. Kimura, H. Outa, M. Motokawa, T. Kambe, K. Nagata and H. Tanaka: J. Phys. Soc. Jpn. **66** (1997) 4017.

[21] M. L. Plumer, A Caillé and K. Hood: Phys. Rev. B **39** (1989) 4489.

[22] M. L. Plumer, A. Caillé, A. Mailhot and H. T. Diep: *Magneticsystems with Competing Interactions* Ed. H. T. Diep (Singapore; World Scientific) (1994)

[23] T.Goto, T. Inami and Y. Ajiro: J. Phys. Soc. Jpn. **59** (1990) 2328.

[24] H. A. Katori, T. Goto and Y. Ajiro: J. Phys. Soc. Jpn. **62** (1992) 743.

[25] M. Enderle, G. Furtuna and M. Steiner: J. Phys.: Condens. Matter **6** (1994) L385.

[26] H. Kawamura, A. Caillé and M. L. Plumer: Phys. Rev. B **41** (1989) 4416.

[27] H. Kawamura: J. Phys. Soc. Jpn. **61** (1992) 1299.

[28] Y. Ajiro,T. Nakashima, Y. Unno, H. Kadowaki, M. Mekata and N. Achiwa: J. Phys. Soc. Jpn. **57** 2648.

[29] T. E. Mason, B. D. Gaulin and M. F. Collins: Phys. Rev. B **39** (1989) 586.

[30] H. Kadowaki, S. M. Shapiro, T. Inami and Y. Ajiro: J. Phys. Soc. Jpn. **63** (1994) 1530.

[31] H. Kadowaki, S. M. Shapiro, T. Inami and Y. Ajiro: J. Phys. Soc. Jpn. **57** (1988) 2640.

[32] Y. Ajiro, T. Inami and H. Kadowaki: J. Phys. Soc. Jpn. **59** (1990) 4142.

[33] H. Kadowaki, T Inami, Y. Ajiro, K. Nakajima and Y. Endoh: J. Phys. Soc. Jpn. **60** (1991) 1708.

[34] D. Beckmann, J. Wosnitza, H. von Löhneysen and D. Visser: J. Phys.: Condens. Matter **5** (1993) 6289.

[35] R. Deutschmann, H. von Löhneysen, J. Wosnitza, R. K. Kremer and D. Visser: Europhys. Lett. **17** (1992) 637.

[36] B. D. Gaulin, T. E. Mason and M. F. Collins: Phys. Rev. Lett. **62** (1989) 1380.

[37] B. D. Gaulin: *Magnetic systems with competing interactions*, ed. by H. T. Diep (World Scientific, Singapore, 1994) p 305.

[38] Zandbergen: J. Solid State Chem. **35** (1980) 367.

[39] U. Falk, A.Furrer, H. U. Güdel and J K. Kjems: Phys. Rev.B **35** (1987) 4888.

[40] T. Inami, K. Kakurai, H. Tanaka, M. Enderle and M. Steiner: J. Phys. Soc. Jpn. **63** (1994) 1530.

[41] K. Iio, H. Hotta, M. Sano, H. Masda, H. Tanaka and K. Nagata: J. Phys.Soc. Jpn. **57** (1988) 50.

[42] A. Harrison, M. F. Collins, J. Abu-Dayyeh and C. V. Stager: Phys. Rev. B **43** (1991) 679.

[43] J. Goodyear and D. J. Kennedy: Acta Crystallogr. **28** (1972) 1640.

[44] G. L. McPherson, L. J. Sindel, H. F. Quals, C. B. Frederich and C. J. Doumit: Inorg. Chem. **14** (1975) 1831.

[45] J. P.Sanchez, J. M. Friedt, B. Djeromouni and G. Jehanno: J. Phs. Chem. Solids **40** (1979) 585.

[46] H. Kawamura: J. Phys. Soc. Jpn. **61** (1990) 1299.

[47] H. Kawamura: J. Phys.: Condens. Matter **10** (1998) 4707.

[48] M. F. Collins: *Magnetic Critical Scattering* (New York: Oxford University Press) (1989) p 29.

[49] H. Weber, D. Beckmann, J. Wosnitza, H. von Löhneysen and D. Visser: Int. J. Mod. Phys. B **9** (1995) 1387.

[50] R. Brener, E. Ehrenfreund and H. Shechter: J. Phys. Chem. Solids **38** (1977) 1023.

[51] H. Tanaka, T. Hasegawa and K. Nagata: J. Phys. Soc. Jpn. **62** (1993) 4053.

[52] H. Tanaka, H. Nakano and S. Matsuo: J. Phys. Soc. Jpn. **63** (1994) 3169.

[53] M. E. Fisher: Amer. J. Phys. **32** (1969) 343.

[54] K. Nagata, Y. Tazuke and K. Tsushima: J. Phys. Soc. Jpn. **32** (1972) 1486.

[55] S. Miyashita and H. Kawamura: J. Phys. Soc. Jpn. **53** (1985) 3385.

[56] J. Villain: J. Phys. C: Solid State Phys. **10** (1977) 4793.

[57] T. Bhattacharya, A. Billoire, R. Lacaze and T. Jolicoeur: J. Phys. (Paris) **I4** (1992) 122.

[58] D. Loison and H. T. Diep: Phys. Rev. B **50** (1994) 16453.

[59] A. Mailhot, M. L. Plumer and A. Caillé: Phys. Rev. B **50** (1994) 6854.

[60] G. Zumbach: Phys. Rev. Lett. **71** (1993) 2421.

[61] P. Azaria, B. Delamotte and T. Jolicoeur: Phys. Rev. Lett. **64** (1990) 3175.

[62] M. L Plumer and A. Mailhot: J. Phys.: Condens. Matter **9** (1997) 16113.

[63] M. L. Plumer and A. Mailhot: Phys. Rev. B **50** (1994) 16113.

[64] H. B. Weber,T. Werner, J. Wosnitza, H. von Löhneysen and U. Schotte: Phys. Rev. B **54** (1996) 15924.

[65] A. W. Schlueter, R. A. Jacobson and R. E. Rundle: Inorg. Chem. **5** (1966) 277.

[66] R. Laiho, N. Natarajan and M. Kaira: Phys. Status Solidi (a) **15** (1973) 311.

[67] C. J. Kroese, W. J. A. Maaskant and G. D. Verschoor: Acta Crystallogr. **B30** (1974) 1053.

[68] S. Hirotsu: J. Phys.: Condens. Matter **10** 967.

[69] H. A. Graf, G. Shirane, U. Schotte, H. Dachs, N. Pyka and M. Iizumi: J. Phys.: Condens. Matter **1** (1989) 3743.

[70] U. Schotte, H. A. Graf and H. Dachs: J. Phys.: Condens. Matter **1** (1989) 3765.

[71] K. Adachi, N. Achiwa and M. Mekata: J. Phys. Soc. Jpn. **49** (1980) 545.

[72] Y. Tazuke, H. Tanaaka, K. Iio and K. Nagata: J. Phys. Soc. Jpn. **50** (1981) 3919.

[73] H. Tanaka, U. Schotte and K. D. Schotte: J. Phys. Soc. Jpn. **61** (1992) 1344.

[74] W. Palme, F. Mertens, O. Born, B. Lüthi and U. Schotte: Solid State Comm. **76** (1990)

[75] F. J. Rioux and B. C. Gerstein: J. Chem. Phys **50** (1969) 758.

[76] H. Hyodo, K. Iio and K. Nagata: J. Phys. Soc. Jpn. **50** (1981) 1545.

[77] H. B. Weber, T. Werner, J. Wosnitza, H. v. Löhneysen and U. Schotte: Phys. Rev. **54** (1996) 15924.

[78] H. Nojiri, Y. Tokunaga and M Motokawa: J. Physique Colloque C8 **49** Supplément (1988) 1459.

[79] T. Nikuni and H. Shiba: J. Phys. Soc. Jpn. **62** (1993) 3268.

[80] M. Mino, K. Ubukata, T. Bokui, M. Arai, H. Tanaka and M. Motokawa: Physica B **201** (1994) 213.

[81] U. Schotte, N. Stüßer, K. D. Schotte, H. Weinfurter, H. M. Mayer and M. Winkelmann: J. Phys.: Condens. Matter **6** (1994) 10105.

[82] H. Ohta, S. Imagawa, M. Motokawa and H. Tanaka: J. Phys. Soc. Jpn. **62** (1993) 3011.

[83] M. Chiba, K. Ohara, Y. Ajiro and T. Morimoto: J. Phys. Soc. Jpn. **62** (1993) 4186.

[84] A. E. Jacobs, T. Nikuni and H. Shiba: J. Phys. Soc. Jpn. **62** (1993) 4066.

[85] T. Nikuni and A. E. Jacobs: Phys. Rev. B **57** (1998) 5205.

[86] H. Nojiri, K. Takahashi, T. Fukuda, M, Fujita, M. Arai and M. Motokawa: Physica B **241-243** (1998) 210.

[87] T. Werner, H. B. Weber, J. Wosnitza, A. Kelnberger, M. Meschke, U. Schotte, N. Stüßer, Y. Ding and M. Winkelmann: Solid State Comm. **102** (1997) 609.

[88] A. E. Jacobs and T. Nikuni: J. Phys.: Condens. Matter **10** (1998) 6405.

[89] U. Schotte,A. Kelnberger and N. Stüßer: J. Phys.: Condens. Matter **10** (1998) 6391.

[90] A. V. Chubukov and D. I. Golosov: J. Phys.: Condens. Matter **3** (1991) 69.

[91] M. Mekata: J. Phys. Soc. Jpn. **42** (1977) 76.

[92] M. Mekata and K. Adachi: J. Phys. Soc. Jpn. **44** (1978) 806.

[93] H. Tanaka, K. Iio and K. Nagata: J. Phys. Soc. Jpn. **54** (1985) 4345.

[94] R. E. Watson and A. J. Freeman: Acta Crystallogr. **14** (1961) 27.

[95] J. Hirano, S. Ueda, M. Chiba, T. Ono, H. Tanaka and T. Kubo: Int. Conf. on Low Temperature Physics (Helsinki) (1999).

[96] P. Wong, P. M. Horn, R. J. Birgeneau, C. R. Safinya and G. Shirane: Phys. Rev. Lett. **45** (1980) 1974.

[97] P. Wong, P. M. Horn, R. J. Bergeneau and G. Shirane: Phys. Rev. B **27** (1983) 428.

[98] K. Katsumata, H. Yoshizawa, G. Shirane and R. J. Bergeneau: Phys. Rev. B **31** (1985) 316.

[99] H. Tanaka, T. Hasegawa an K. Nagata: J. Phys. Soc. Jpn. **62** (1993) 4053.

[100] T. Ono, H. Tanaka, T. Kato and K. Iio: J. Phys.: Condens. Matter **10** (1998) 7209.

[101] T. Ono, H. Tanaka, T. Kato, K. Nakajima and K. Kakurai: J. Phys.: Condens. Matter **11** (1999) 4427.

[102] I. Matsubara, K. Iio and K. Nagata: J. Phys. Soc. Jpn. **51** (1982) 3071.

[103] A. C. Phaff, C. H. W. Swüste and W. J. M. de Jonge: Phys. Rev. B **25** (1982) 6570.

[104] D. Mukamel: Phys. Rev. Lett. **46** (1981) 845.

[105] M. Pleimling: Eur. Phys. J. B **10** (1999) 465.

[106] C. Scherer and Y. Barjhoux: Phys. Stat. Sol. (b) **80** (1977) 313.

[107] H. Shiba: Solid State Comm. **41** (1982) 511.

[108] G.R. Davidson, M. Eibshütz, D. E. Cox and V. J. Minkiewicz: AIP Conf. Proc. **5** (1971) 436.

[109] T. Haseda, N. Wada, M Hata and K. Amaya: Physica **108B** (1981) 841.

[110] N. Wada, K Ubukoshi and K. Hirakawa: J. Phys. Soc. Jpn. **51** (1982) 2833.

[111] H. Shiba and N. Suzuki: J. Phys. Soc. Jpn. **51** (1982) 3488.

[112] N. Wada, K. Sumiyoshi, T. Watanabe and K. Amaya: J. Phys. Soc. Jpn. **52** (1983) 1893.

[113] K. Kakurai: unpublished data.

[114] H. Shiba, T. Nikuni and A. E. Jacobs: preprint

[115] T. Kambe, H. Tanaka, S. Kimura, H. Ohta, M. Motokawa and K. Nagata: J. Phys. Soc. Jpn. **65** (1996) 1799.

[116] T. Inami: Ph D thesis, Institute for Solid State Physics, The University of Tokyo (1995).

[117] H. Kadowaki, K. Hirakawa and K. Ubukoshi: J. Phys. Soc. **52** (1983) 1799.

[118] A. Yoshimori: J. Phys. Soc. Jpn. **14** (1959) 807.

[119] K. Yosida and H. Miwa: J. Appl. Phys. **32** (1961) 8S.

List of publications

1. Phase transitions and critical phenomena of triangular antiferromagnetic system: $CsMn(Br_xI_{1-x})_3$
   T. Ono, H. Tanaka, T. Kato, K. Iio, K. Nakajima and K. Kakurai: J. of Magnetism and Magnetic Materials **177-181** (1998) 735.

2. Magnetic phase transitions in the triangular antiferromagnetic system $CsMn(Br_xI_{1-x})_3$
   T. Ono, H Tanaka, T. Kato and K. Iio: J. Phys.: Condens. Matter **10** (1998) 7209.

3. Magnetic structure and behaviour of the Heisenberg limit triangular antiferromagnet $CsMn(Br_{0.19}I_{0.81})_3$
   T. Ono, H. Tanaka, T. Kato, K. Nakajima and K. Kakurai: J. Phys.: Condens. Matter **11** (1999) 4427.

4. Field-induced new ordered phase in triangular antiferromagnet $RbFeCl_3$
   T. Ono and H. Tanaka: J. Phys. Soc. Jpn. **10** (1999) 3174.

5. A new ordered phase in the spin-$\frac{1}{2}$ triangular antiferromagnetic system $CsCu_{1-x}Co_xCl_3$
   T. Ono, H. Horai and H. Tanaka: J. Phys.: Condens. Matter **12** (2000) 975.

6. Oblique triangular antiferromagnetic phase in $CsCu_{1-x}Co_xCl_3$
   T. Ono, H. Tanaka, T. Kato, A. Hoser, N. Stüßer and U. Schotte: preparing.